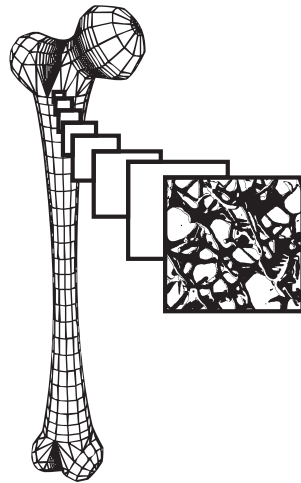


Proceedings
of the 2nd GAMM Seminar on
Continuum Biomechanics

W. Ehlers & N. Karajan (Eds.)



Report No.: II-16

Institute of Applied Mechanics (CE)
Chair II (Continuum Mechanics)
Universität Stuttgart
2007

Report No. II-16
Institut für Mechanik (Bauwesen)
Lehrstuhl II für Kontinuumsmechanik
Universität Stuttgart, Germany, 2007

Editors:

Prof. Dr.-Ing. W. Ehlers
Dipl.-Ing. N. Karajan

© Prof. Dr.-Ing. W. Ehlers
Dipl.-Ing. N. Karajan
Institut für Mechanik (Bauwesen)
Lehrstuhl II für Kontinuumsmechanik
Universität Stuttgart
Pfaffenwaldring 7
70569 Stuttgart, Germany

Druck mit freundlicher Unterstützung der

LB = BW

Stiftungen
Landesbank Baden-Württemberg

All rights reserved. No part of this publication may be reproduced, stored in a retrieval system, or transmitted in any form or by any means, electronic, mechanical, photocopying, microfilming, recording, scanning or otherwise, without written permission from the Editors.

VGE
Verlag GmbH

Produced by VGE Verlag GmbH, Essen, Germany
Printed by DIP – Digital Print, Witten, Germany, 2007

ISBN 978-3-937399-16-X

Preface

The 2nd GAMM Seminar on Continuum Biomechanics took place November 22–24, 2006, in Freudenstadt-Lauterbad, Germany. Like the first one, it was organized by the Biomechanics Activity Group of the “Gesellschaft für Angewandte Mathematik und Mechanik” (GAMM), which promotes scientific development in all areas of applied mathematics and mechanics. The Seminar venue was the Waldhotel Zollernblick in the climatic spa Freudenstadt-Lauterbad located in the Black Forest region, Germany.

The GAMM Biomechanics Activity Group was formed on October 23, 2003, in Stuttgart with the major objective to foster the interest in biomechanical problems in the German-speaking area in order to keep pace with international developments. After the 1st GAMM Seminar on Continuum Biomechanics (November 24–26, 2004), the actual Seminar was the second major initiative of the Activity Group providing a discussion forum on the recent advances in theoretical, numerical, and experimental techniques in the broad field of biomechanical engineering with special focus on soft and hard tissues. The informal nature of the Seminar offered the opportunity to openly exchange scientific ideas, where the welcoming atmosphere of the Waldhotel Zollernblick with an exceptional view on the Swabian Alb furthermore contributed to its overall success. In particular, exposed problems of continuum biomechanics and computational biomechanics have been presented in 20 oral presentations, out of which 11 contributions are published in this Proceedings Volume. Since the organizers are confident that such Seminars help to manifest and to enlarge the biomechanics community in Germany, we still aim at establishing a biennial GAMM Seminar Series on Continuum Biomechanics.

Finally, we would like to express our thanks to the sponsors of the Seminar, namely CADFEM GmbH, DYNAmore GmbH, LBBW-Stiftung, Robert Bosch GmbH, SFB 404, and GAMM. The financial support allowed us to schedule three invited presentations of renown scientists, to publish this volume of Proceedings, and last but not least to keep the fee low, so that, in particular, younger researchers had the possibility to participate. The organization and execution of the Seminar as well as the preparation of the Proceedings Volume was performed by the staff of the Institute of Applied Mechanics (CE) of the University of Stuttgart. Also their extremely valuable help is herewith most gratefully acknowledged.

Stuttgart, December 4, 2007

Wolfgang Ehlers

Nils Karajan

Contents

Micromechanical Modelling of Skeletal Muscles: From the Single Fibre to the Whole Muscle	1
<i>M. Böl & S. Reese</i>	
Parallel 3-d simulations of a biphasic porous media model in spine mechanics	11
<i>W. Ehlers, N. Karajan, C. Wieners</i>	
Experimental-Numerical Studies of Impaction Loading of Osteochondral Grafts	21
<i>U.-J. Görke, A. Bucher, R. Kreißig, H. Günther & M. A. Wimmer</i>	
A Damage-based Model to Describe Aging in Cortical Bone ..	33
<i>I. Ott, R. Kienzler & R. Schröder</i>	
Numerical Investigations on the Biomechanical Compatibility of Hip-Joint Endoprostheses	49
<i>U. Nackenhorst & A. Lutz</i>	
Remodelling and Growth of Living Tissue – A Multiphase Theory	59
<i>T. Ricken & J. Bluhm</i>	
On Multiscale Modelling of Perfused Tissues Using Homogeni- sation of a Strongly Heterogeneous Biot Continuum	77
<i>E. Rohan, R. Cimrman & V. Lukeš</i>	
Calculation of Muscle and Joint Forces in the Masticatory System	87
<i>S. Rues, H. J. Schindler, J. Lenz & K. Schweizerhof</i>	
On Mechanical Modelling of Arterial Walls and Parallel Solution Strategies	97
<i>J. Schröder, A. Klawonn, D. Balzani, O. Rheinbach & D. Brands</i>	
Wave Propagation in Cancellous Bones	109
<i>H. Steeb</i>	
Integrated Motion Measurement in Biomechanics	121
<i>J. F. Wagner</i>	
Author Index	i
List of Participants	iii
Scientific Program	vii

Micromechanical Modelling of Skeletal Muscles: From the Single Fibre to the Whole Muscle

M. Böl & S. Reese

Institute of Solid Mechanics, Braunschweig University of Technology,
Schleinitzstraße 20, 38106 Braunschweig, Germany

Abstract. The structure of a skeletal muscle is dominated by its hierarchical architecture in which thousands of muscle fibres are arranged within a connective tissue network. The single muscle fibres consist of many force-producing cells, known as sarcomeres, which contribute to the contraction of the whole muscle. There are a lot of questions concerning the optimisation of muscle strength and agility. To answer these questions, numerical testing tools can be an adequate alternative to standard experimental investigations. From the mechanical point of view, the material behaviour of muscles is highly non-linear. They undergo large deformations in space thereby changing their shape significantly, so that geometrical nonlinearity has to be considered. Many authors use continuum-based approaches in combination with the finite element method to describe such material behaviour. However, models of this kind require realistic constitutive relations between stress and strain which are difficult to determine in an inhomogeneous material.

The present approach is crucially based on the use of the finite element method. The material behaviour of the muscle is split into a so-called active and a passive part. To describe the passive part special unit cells consisting of one tetrahedral element and six truss elements have been derived. Embedded into these unit cells are further truss elements which represent bundles of muscle fibres. In summary, the present concept has the advantage that a three-dimensional model is developed which allows us to take into account many physiological processes at the micro level.

1 Introduction

Skeletal muscles can be considered to be a complex organisation of thousands of force-producing muscle fibres arranged within a connective tissue. Muscles are responsible for the movement of the human body, they provide strength, serve as shock absorption, and protect the skeleton system against external loads. Skeletal muscles, like most biological tissues, undergo large deformations and exhibit highly non-linear mechanical behaviour. Their passive properties can be described by non-linear hyperelastic constitutive relations, see, e. g., [4]. In contrast to other biological tissues skeletal muscles show the ability of active contraction where only tensile forces are generated.

One of the first mathematical models was developed by Hill [6, 7]. This phenomenological model is derived from force-velocity measurements on an entire muscle. As an early representative of the group of microstructural approaches, the concept of Huxley [8] is crucially based on investigations of

the behaviour of the cross bridges. Both the phenomenological as well as the micromechanically-based models are applied to describe the contraction of the whole muscle. However, the focus of such methods is certainly rather on the simulation of the whole body movement than on the microstructural behaviour of a single muscle. To incorporate further, more complex geometrical aspects of skeletal muscles, planimetric and three-dimensional models were designed, see, e. g., [12, 1]. Most of these continuum-based models use a macroscopic description of the passive muscle behaviour (soft tissue) combined with a one-dimensional, possibly micromechanically-motivated, modelling of the active muscle fibres.

The present contribution differs from earlier approaches insofar as it is formulated at the meso mechanical level, as previously introduced in the framework of rubber-like polymers, cf. [3]. In this way the actual geometry of the muscle, i. e., the directional distribution of the muscle fibres, can be easily taken into account. The mechanical behaviour of muscles is, as earlier mentioned by Van Leeuwen [10], split into a passive and an active part. The here proposed concept is based on the idea of representing the passive part by means of an assembly of non-linear truss elements. In each truss element, the force-stretch behaviour of a certain group of collagen fibres is implemented. The truss elements are arranged in such a way that one of them lies on each edge of one finite tetrahedral element. In this way a so-called tetrahedral unit cell is formed. The tetrahedral element of the unit cell serves to model the (near-)incompressible behaviour of skeletal muscles. By using a random assembling procedure, we are able to model arbitrary geometries. An ensemble of these unit cells lets us simulate the behaviour of the soft tissue alone. To incorporate muscle activation, bundles of muscle fibres in form of non-linear truss elements are embedded in the before mentioned assembly of unit cells. These trusses contain a mathematical description of the activation at the fibre level. In this way, we are able to simulate complex muscle structures by arbitrary muscle fibre distributions.

2 Material Modelling of Skeletal Muscles

According to the aforementioned split of the material behaviour into active and passive parts also the Helmholtz free energy

$$W = W_{\text{active}} + W_{\text{passive}} \quad (1)$$

is additively decomposed into active (W_{active}) and passive (W_{passive}) contributions.

2.1 The Active Material Behaviour

One fundamental property of a skeletal muscle fibre is its ability to contract without any mechanical influence from outside. In the present contribution

this behaviour is implemented into three-dimensional truss elements. The force in one truss element is given by

$$F_{\text{active}} = f_{\text{fibre}} \bar{P}_t f_t(t) f_\lambda(\lambda_{\text{fibre}}) f_v(\dot{\lambda}_{\text{fibre}}), \quad (2)$$

where \bar{P}_t denotes the largest possible applied force inside the fibre. This force is correlated with the activation function $f_t(t)$. Furthermore, $f_\lambda(\lambda_{\text{fibre}})$ is a function of the fibre stretch λ_{fibre} and $f_v(\dot{\lambda}_{\text{fibre}})$ denotes a function depending on the stretch rate $\dot{\lambda}_{\text{fibre}}$ of the muscle fibre. Due to the fact that in this paper only quasi-static contraction mechanisms are studied, we only concentrate on the function of activation as well as the function of stretch. The function depending on the stretch rate is chosen to be equal to one.

A typical skeletal muscle consists of thousands of muscle fibres. Due to this high number of fibres it is impossible to discretise *each* muscle fibre by *one* truss element. To compensate this, in (2), the ratio $f_{\text{fibre}} = N_{\text{fibre}}/N_{\text{trussf}}$ has been introduced, where N_{fibre} represents the number of fibres per reference cross section and N_{trussf} the number of truss elements in this cross section.

The Function of Activation: One way of controlling the force inside the muscle is the variation of the impulse rate. The mechanical response initiated

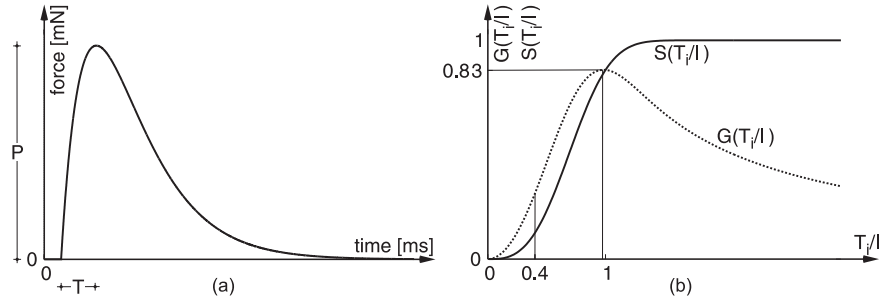


Fig. 1. Isometric single motor unit twitch: (a) Force response of a single impulse and (b) non-linear behaviour between the gain/sigmoid and stimulus rate.

by a motoneuron discharge is a single motor unit twitch as schematically depicted in Figure 1 (a). In the time-dependent function

$$g(t) = \frac{P t}{T} e^{1 - (t/T)}, \quad (3)$$

P and T are the twitch force and the contraction time, respectively. Relation (3) can be expressed for different types of motor units as follows:

$$g_i(t) = \frac{P_i t}{T_i} e^{1 - (t/T_i)} \quad \text{with } i = 1, 2, \dots, n_{\text{MU}}, \quad (4)$$

where n_{MU} depicts the total number of motor unit types. The two twitch parameters P and T are physically-based and can be found in the literature,

see, e.g., [11]. Experimental studies of the frequency response of skeletal muscles show that the relation between the isometric force and the stimulus rate is non-linear, cf., e.g., [9]. This well-known sigmoid relationship $S(T_i/I)$ includes a change in the gain G_i of the nerve-muscle system depending on the stimulus rate T_i/I , see Figure 1 (b).

The before mentioned non-linear behaviour is integrated in the here suggested approach by allowing the gain in the motor unit force to vary as a function of the stimulus rate, normalised with respect to the twitch contraction time T_i . The gain is determined from the sigmoid of the form

$$S(T_i/I) = 1 - e^{-2(T_i/I)^3}. \quad (5)$$

Dividing (5) by the normalised stimulus rate leads to the gain

$$G_i = \frac{S(T_i/I)}{T_i/I} = \frac{1 - e^{-2(T_i/I)^3}}{T_i/I}. \quad (6)$$

In Figure 1 (b) the sigmoid behaviour (continuous shape) as well as the gain (dotted shape) is depicted.

The insertion of the gain function into (4) yields the force response of a motor unit as

$$h_i(t) = G_i \frac{P_i t}{T_i} e^{1 - (t/T_i)} = \underbrace{P_i}_{a_i} \underbrace{\frac{G_i t}{T_i} e^{1 - (t/T_i)}}_{b_i}. \quad (7)$$

The aim of this section is to derive the product $\bar{P}_t f_t(t)$ (see (2)). Therefore, (7) has been multiplicatively split into the two parts a_i and b_i . Following the principle of superposition, it is now possible to sum up the single twitch forces for a certain pool of motor units ($i = 1, 2, \dots, n_{\text{MU}}$) in dependence of a train containing n_{IMP} discharges. This leads to the product of the maximum force \bar{P}_t and the activation function $f_t(t)$, see also (2),

$$\bar{P}_t f_t(t) = \sum_{i=1}^{n_{\text{MU}}} a_i \sum_{i=1}^{n_{\text{MU}}} \sum_{j=1}^{n_{\text{IMP}}} b_i(t - t_{ij}) \quad (8)$$

with $i = 1, 2, 3, \dots, n_{\text{MU}}$ and $j = 1, 2, 3, \dots, n_{\text{IMP}}$ for intervals ($t - t_{ij} \geq 0$).

The Function of Stretch: The dependence of the sarcomere force on the sarcomere length is described by the isometric length-force curve (Figure 2 (a)). From the historical point of view, Blix [2] was the first who constructed a length-force curve from a series of experiments performed at different muscle lengths. He showed that the isometric force of a frog muscle increases with increasing sarcomere length, passes through a maximum at a certain length, addressed as optimum length (see point A in Figure 2 (a)), and decreases again. It is well-known that the muscle contraction is caused by the

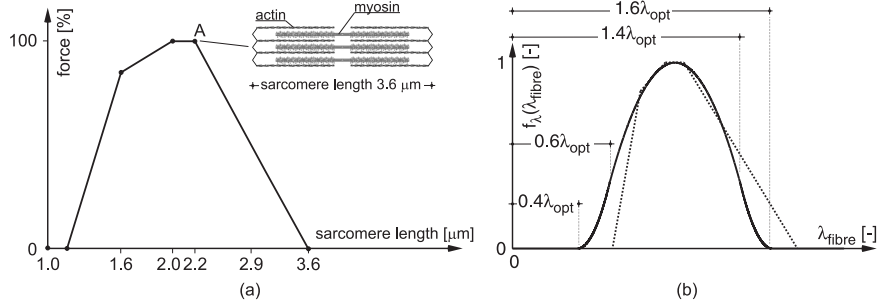


Fig. 2. Relation between contraction force: (a) Length of the sarcomere and overlapping of the actin and myosin filament and (b) comparison between the piecewise linear and the continuous function.

interaction between the actin and myosin filaments sliding past each other. This filament sliding can be seen to be caused by independent force generators, the so-called cross bridges. Experimental evidence was provided by Gordon et al. [5] showing that the isometric length-force relationship of a maximally activated sarcomere is directly related to the overlap between the actin and myosin filaments, cf. Figure 2 (a), the overlap being proportional to the number of available cross bridges and the sarcomere length.

From the mathematical point of view, it is more elaborate to implement the piecewise linear function (Figure 2 (b), dotted curve) into a finite element code. Therefore, we use in this work a continuous curve, see Figure 2 (b) and also [1]. The mathematical representation of this function is given as follows:

$$f_{\lambda}(\lambda_{\text{fibre}}) = \begin{cases} 0 & \text{if } \lambda_{\text{fibre}} < 0.4 \lambda_{\text{opt}} , \\ 9 \left(\frac{\lambda_{\text{fibre}}}{\lambda_{\text{opt}}} - 0.4 \right)^2 & \text{if } 0.6 \lambda_{\text{opt}} > \lambda_{\text{fibre}} \geq 0.4 \lambda_{\text{opt}} , \\ 1 - 4 \left(1 - \frac{\lambda_{\text{fibre}}}{\lambda_{\text{opt}}} \right)^2 & \text{if } 1.4 \lambda_{\text{opt}} > \lambda_{\text{fibre}} \geq 0.6 \lambda_{\text{opt}} , \\ 9 \left(\frac{\lambda_{\text{fibre}}}{\lambda_{\text{opt}}} - 1.6 \right)^2 & \text{if } 1.6 \lambda_{\text{opt}} > \lambda_{\text{fibre}} \geq 1.4 \lambda_{\text{opt}} , \\ 0 & \text{if } \lambda_{\text{fibre}} \geq 1.6 \lambda_{\text{opt}} . \end{cases} \quad (9)$$

Only one dimensionless constant λ_{opt} is used which defines the optimal fibre stretch at which the sarcomere reaches its optimal length, cf. Figure 2 (b).

2.2 The Passive Material Behaviour

The behaviour of passive tissue is characterised by large deformations, a non-linear stress-strain relation and (near-)incompressibility. To model such behaviour, an approach originally developed for rubber-like materials, see [3], is used. A so-called finite element unit cell has been developed that consists of one tetrahedral element and six truss elements lying on each edge of the

tetrahedron. The Helmholtz free energy of one unit cell then includes one contribution coming from the tetrahedral element (W_{tetr}) and another one coming from the truss elements ($W_{\text{truss } j}$, $j = 1, \dots, 6$):

$$W_{\text{passive}} = W_{\text{tetr}} + \sum_{j=1}^6 W_{\text{truss } j}. \quad (10)$$

It is well-known that soft tissue-like material can be seen as a three-dimensional network composed of a huge number of collagen fibres. The micromechanical material behaviour of a bundle of collagen fibres is characterised by the second summand of (10) and can be rewritten as

$$W_{\text{truss } j} = \frac{1}{A_{0j} L_{0j}} f_{\text{coll}} W_{\text{coll } j} \quad (11)$$

with

$$W_{\text{coll } j} = k n_j \Theta \left[\frac{\lambda_{\text{coll } j}}{\sqrt{n_j}} \beta_j + \ln \frac{\beta_j}{\sinh \beta_j} \right]. \quad (12)$$

Herein, A_{0j} and L_{0j} denote the cross section and the length of the undeformed truss element, respectively. As shown in [3] these parameters cancel out of the formulation. Especially important is the fact that the truss length L_{0j} does not correlate with the length of the collagen fibre bundle. The computational efficiency of the present approach could not compete with classical continuum-based finite element computations if the mesh density was linked to the geometry of the microstructure.

$W_{\text{coll } j}$ represents the energy function of one collagen fibre and depends on the Boltzmann's constant k , the number of links per fibre n_j , the absolute temperature Θ , and the inverse Langevin function β_j , cf. [3]. The fibre stretch is computed by means of the relation $\lambda_{\text{coll } j} = r_j/r_{0j} = L_j/L_{0j}$, where r_j describes the end-to-end distance of the fibre in the deformed state and r_{0j} the same distance in the undeformed case. The fact that the ratios r_j/r_{0j} and L_j/L_{0j} are set equal represents the micro-macro transition in the model. Note again that this does not restrict the choice of L_{0j} , i. e., the density of the finite element mesh.

Finally, the parameter $f_{\text{coll}} = N_{\text{coll}}/N_{\text{truss } c}$ defines the ratio between N_{coll} , the number of collagen fibres per reference volume and $N_{\text{truss } c}$, the number of truss elements in the same reference volume. It is obvious that one strives to make f_{coll} as large as possible, because then the minimum number of elements and consequently maximum computational efficiency is obtained.

The first summand of (10) is needed to describe the volumetric behaviour of the unit cell. It is used here to give the structure additional ‘‘volumetric stiffness’’. W_{tetr} reads in detail

$$W_{\text{tetr}} = \frac{K}{4} (J^2 - 1 - 2 \ln J), \quad (13)$$

where $J = \det \mathbf{F}$ denotes the determinant of the macroscopic deformation gradient \mathbf{F} and K is the bulk modulus.

3 Results

The aim of this section is to study how the deformation behaviour of skeletal muscles deviates from the one of the single muscle/collagen fibre. To simplify the discretisation, in a first step, an idealised fusiform muscle geometry is applied, see Figure 3. The pathways of the fibres are computed by means of the vector field

$$\Gamma(z) = \begin{pmatrix} r(z) \cos(\alpha) \\ r(z) \sin(\alpha) \\ z \end{pmatrix}. \quad (14)$$

Herein the radial location of the muscle fibre is identified by α and $r(z)$ is the distance of the fibre from the z -axis, located in the centre of the muscle. One possibility to express $r(z)$ is $r(z) = r_2 \exp(z \ln(r_2/r_1)/h^2)$, where r_2 is the maximum radius of the muscle in the case of $z = 0$. The function $r(z)$ is limited to the interval $z \in [-h, h]$, so that the minimum radius r_1 is located at $z = -h$ and $z = h$, respectively.

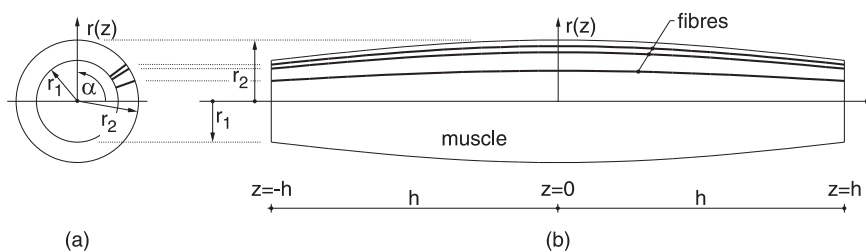


Fig. 3. Two-dimensional view of the used idealised fusiform muscle geometry. (a) Front view and (b) side view of the muscle/fibres.

3.1 Idealised Muscle Geometry

First of all a quasi-static simulation of an idealised muscle geometry as sketched in Figure 4(a) has been performed ($r_1 = 10$ mm, $r_2 = 17$ mm, $h = 50$ mm and $\alpha = 22.5^\circ$, cf. Figure 3). The geometry of the muscle is fixed at one end and free to move at the other end. No external loads are used, the muscle is only loaded by its activation. The finite element simulations have been performed using the parameters listed in Table 1. Three different stimulus rates ($1/I = 5, 40, 160$ imp/s) are used. Figure 4(a) shows the results of the simulations. Here, the displacement-time behaviour is plotted. It can be recognised that for low stimulus rates, such as $1/I = 5$ imp/s, the displacement response is characterised by single twitches. If the activation rate increases, e. g., $1/I = 40$ imp/s, the single twitches superpose each other, this leads to a higher displacement level. Here, the shape of the single twitches can be still seen. If the stimulus rate is high enough ($1/I = 160$ imp/s), the

active muscle behaviour				passive muscle behaviour		
activation function	P	[mN]	70	K	[N/mm ²]	10^5
	T	[s]	0.015	f_{coll}	[-]	$4.106 \cdot 10^{14}$
	$1/I$	[imp/s]	5,40,160	n	[-]	7.8
stretch function	λ_{opt}	[-]	1.4	N_{coll}	[-]	$2.792 \cdot 10^{18}$
	f_{fibre}	[-]	2000	N_{trussc}	[-]	6800
	N_{fibre}	[-]	$3.2 \cdot 10^5$	k	[Nmm/K]	$1.381 \cdot 10^{-20}$
	N_{trussf}	[-]	160	Θ	[K]	273

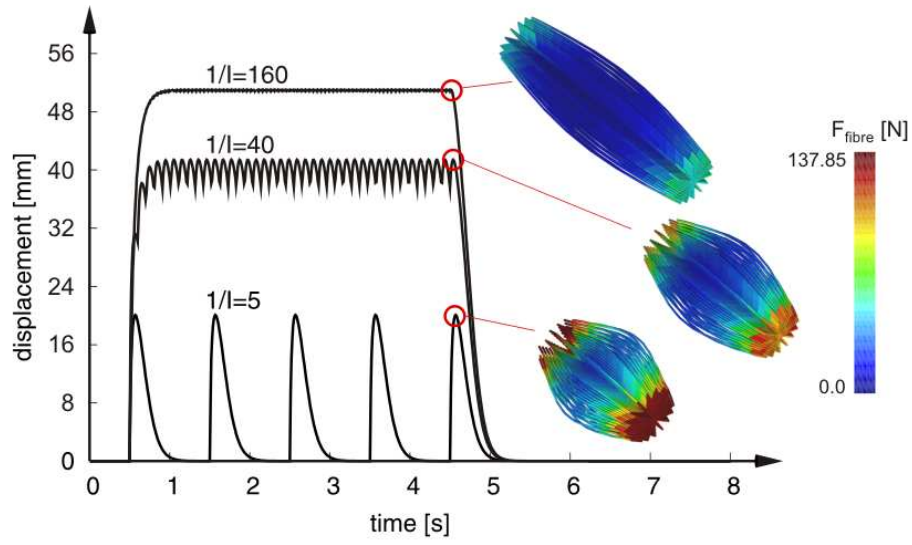
Table 1. Material parameters for the active and passive muscle properties.

displacement response is characterised by a plateau where no single twitch shape can be identified. In this case the response of the activation is called tetanic. In addition to the displacement curves in Figure 4 (a), the distribution of the forces in the truss elements representing the fibre bundles (active material behaviour) is shown. The maximum deformation state for the different stimulus rates is plotted. The largest deformation is reached at $t = 4.5$ s. At this point the muscle has reached its maximum contraction. Here, the forces of the truss elements representing the active material behaviour show the highest values. For $t > 4.5$ s the muscle relaxes.

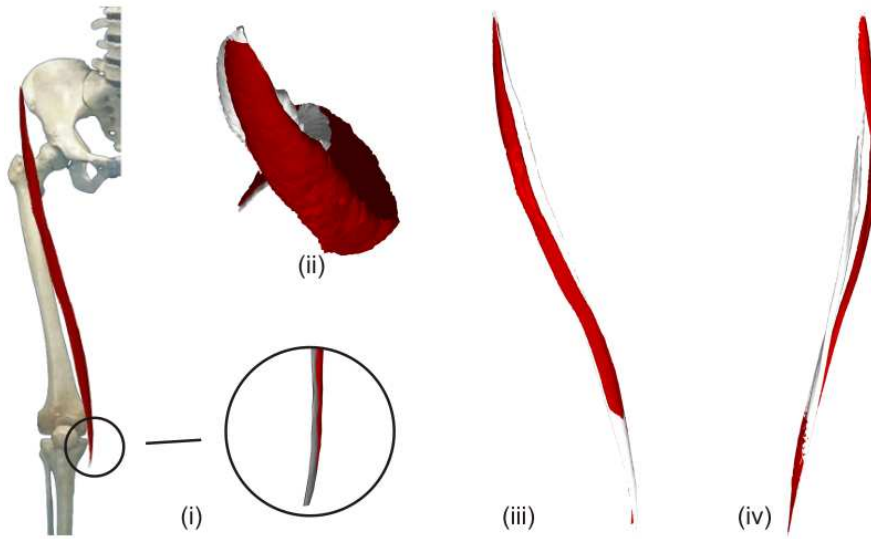
active muscle behaviour				passive muscle behaviour		
activation function	P	[mN]	70	K	[N/mm ²]	10^5
	T	[s]	0.015	f_{coll}	[-]	$3.413 \cdot 10^{14}$
	$1/I$	[imp/s]	200	n	[-]	5.5
stretch function	λ_{opt}	[-]	1.4	N_{coll}	[-]	$1.058 \cdot 10^{18}$
	f_{fibre}	[-]	250	N_{trussc}	[-]	3100
	N_{fibre}	[-]	$4.0 \cdot 10^5$	k	[Nmm/K]	$1.381 \cdot 10^{-20}$
	N_{trussf}	[-]	1600	Θ	[K]	273

Table 2. Material parameters for the active and passive muscle properties.

One aim of this work is to apply the material model to realistic muscle geometries to be responsive to patients-specific questions. Here, the longest muscle of the human body, the sartorius muscle, is studied, see Figure 4 (b). The action of the sartorius muscle is to cross the legs, by flexion of the knee, and flexion and lateral rotation of the hip. Figure 4 (b_i) shows the complete sartorius muscle including the tendon (coloured grey). To study the contraction mechanism of the muscle, isotonic quasi-static simulation is applied. The used parameters are shown in Table 2. The sartorius muscle belongs to the group of fusiform muscles. Due to the spiral geometry of the muscle also the deformation behaviour is characterised by a torsion-like deformation in combination with a contraction, cf. Figure 4 (b_{ii-iv}). This is conform to the physiological “function” of the muscle, because it bends the joints of the hip and the knee in combination with a movement of the thigh to the middle while the lower thigh is rotated to the inner site of the thigh.



(a)



(b)

Fig. 4. (a) Simulation results of an idealised muscle geometry: Displacement-time behaviour for three different activation rates ($1/I = 5, 40, 160$ imp/s) and distribution of the forces in the muscle fibres. (b) Geometry and simulation results (only tetrahedral elements are shown) of the sartorius muscle: (i) Muscle geometry (red = muscle tissue, grey = tendon), (ii) axial, (iii) coronal and (iv) sagittal view (light-grey = undeformed muscle, red = deformed muscle).

4 Conclusions

In the present contribution a new approach for the simulation of skeletal muscles is shown. The basic idea is to split the Helmholtz free energy into two parts. One part represents the passive material behaviour of the muscle, whereas the other part describes the active part. The passive part is modelled by special unit cells which represent the surrounding soft tissue. The active muscle behaviour is embedded in additional finite truss elements. These elements lie inside of the soft tissue.

The development of a realistic muscle modelling based on the finite element method is still at the very beginning. In the present paper, qualitatively reasonable results, based on idealised as well as on realistic muscle geometries, could be obtained. Further work will be directed to validate these results by means of experimental investigations.

References

1. Blemker, S. S.; Pinsky, P. M. & Delp, S. L.: A 3d model of muscle reveals the causes of nonuniform strains in the biceps brachii. *Journal of Biomechanics* **38** (2005), 657–665.
2. Blix, M.: Die Länge und die Spannung des Muskels. *Skandinavisches Archiv für Physiologie* **3** (1894), 295–318.
3. Böl, M. & Reese, S.: Finite element modelling of rubber-like polymers based on chain statistics. *International Journal of Solids and Structures* **43** (2006), 2–26.
4. Fung, Y. C.: *Biomechanics: Mechanical Properties of Living Tissue*, Springer-Verlag, New York, 1993.
5. Gordon, A. M.; Huxley, A. F. & Julian, F. J.: The variation in isometric tension with sarcomere length in vertebrate muscle fibres. *The Journal of Physiology* **184** (1966), 170–192.
6. Hill, A. V.: The maximum work and mechanical efficiency of human muscles, and their most economical speed. *The Journal of Physiology* **56** (1922), 19–41.
7. Hill, A. V.: The heat of shortening and the dynamic constants of muscle. *Proceedings of Royal Society of London B* **126** (1938), 136–195.
8. Huxley, A. F.: Muscle structure and theories of contraction. *Progress in biophysics and biophysical chemistry* **7** (1957), 255–318.
9. Kernell, D.; Eerbeek, O. & Verhey, B. A.: Relation between isometric force and stimulus rate in cat’s hindlimb motor units of different twitch contraction time. *Experimental Brain Research* **50** (1983), 220–227.
10. van Leeuwen, J. L.: Muscle function in locomotion. In Alexander, R. M. (ed.): *Mechanics of Animal Locomotion*, Springer-Verlag, Berlin, 1992, pp. 191–249.
11. Taylor, A. M.; Steege, J. W. & Enoka, R. M.: Motor-unit synchronization alters spike-triggered average force in simulated contractions. *Journal of Neurophysiology* **88** (2002), 265–276.
12. Tsui, C. P.; Tang, C. Y.; Leung, C. P.; Cheng, K. W.; Ng, Y. F.; Chow, D. H. K. & Li, C. K.: Active finite element analysis of skeletal muscle-tendon complex during isometric, shortening and lengthening contraction. *Bio-Medical Materials and Engineering* **14** (2004), 271–279.

Parallel 3-d simulations of a biphasic porous media model in spine mechanics

W. Ehlers¹, N. Karajan¹, and C. Wieners²

¹ Institute of Applied Mechanics (Civil Engineering),
Universität Stuttgart, Pfaffenwaldring 7, 70569 Stuttgart, Germany

² Institute for Applied and Numerical Mathematics,
Universität Karlsruhe, Englerstr. 2, 76 128 Karlsruhe, Germany

Abstract. This contribution presents an extended model based on the Theory of Porous Media (TPM), which is suitable for the simulation of electro-chemically active soft tissues and, in particular, the intervertebral disc (IVD). The respective non-linear constitutive equations include the modelling of the anisotropic material behaviour as well as the osmotic pressure. We introduce a stable finite element discretization, and we propose an iterative parallel solution method with a domain decomposition preconditioner combining an algebraic coarse grid solver on an overlay mesh and approximate ILU solving on the subdomains. Finally, the efficiency of the model is shown by a fully coupled 3-d simulation of a lumbar spine (vertebrae L1 to L5), where one computation shows a healthy spine segment while the other one includes a stiffened L4-L5 motion segment.

1 Introduction

For a better understanding of the complex coupled behaviour of the IVD and its influence on the overall performance of the spine, an appropriate finite element model describing all relevant effects would be of great benefit. In this context, such a model will remarkably aid the design of new implants, if it is possible to reproduce a realistic response due to external loads. However, a realistic numerical simulation of such a complex biological structure requires not only an elaborated material model but also an efficient solution method for the discretized system.

The spine itself consists of several vertebrae and intervertebral discs embedded in between. In our model we neglect the cartilaginous endplates separating the discs and the vertebrae since we expect that their mechanical behaviour is of minor importance. Two main regions can be distinguished in an axial cut through the IVD: a gelatinous core, the nucleus pulposus (NP), enclosed by a fibrous, lamellar structure, the anulus fibrosus (AF). Both regions are composed of a porous multi-component microstructure consisting of a charged, hydrated extracellular matrix as well as an ionized interstitial fluid, yielding a active swelling material. Herein, the solid skeleton consists of proteoglycans (PG's), glycosaminoglycans (GAG's), and collagen fibres of type I and II saturated by a liquid containing dissolved anions and cations

as solutes. The large PG's and GAG's are thereby trapped in the collagen network and carry negative fixed charges, which therefore underlie the same motion as the whole solid matrix. For more details see, e. g., [1, 7, 14, 17] and references therein.

Due to the porous microstructure of both the IVD and the vertebrae, these materials can be adequately modelled in the framework of the TPM. The respective constitutive equations, needed to capture all occurring phenomena, are implemented and can be switched on and off via material parameters. Furthermore, several inhomogeneities occur in the IVD. In particular, this is the inhomogeneous distribution of the orientation and mechanical behaviour of the collagen fibres in the AF as well as the concentration of the fixed negative charges. These inhomogeneities are captured as is described in [7].

The arising coupled set of governing equations can be reformulated in variational form which then allows for a discrete approximation by finite elements. We use Taylor-Hood elements with quadratic approximations of the solid displacement and linear pressure approximation, since they provide stable results also for small time steps and for a wide range of Darcy parameters.

For a full simulation of several spine segments, a sufficiently fine geometry resolution is essential. This leads to very large algebraic systems, so that reliable numerical computations cannot be performed on single processor machines. Thus, a parallel finite element implementation is used, where parallel Krylov methods are used together with a strong preconditioner for the solution of the linearized problems. The efficiency of this solution method is then demonstrated by numerical results showing the mechanical response of vertebrae and intervertebral discs under loading forces. Herein, two computations are performed, one concerning a healthy lumbar spine and another having the lowest motion segment, i. e., the L4-L5 segment, stiffened.

2 An extended binary porous media model

In a standard incompressible biphasic model for quasi-static processes with no mass exchange between the constituents and negligible body forces, the respective volume and momentum balances read

$$\operatorname{div}[(\mathbf{u}_S)'_S + n^F \mathbf{w}_F] = 0 \quad \text{and} \quad \operatorname{div}(\mathbf{T}^S + \mathbf{T}^F) = \mathbf{0}, \quad (1)$$

cf. [4]. In this context, the porosity of the model is denoted by n^F with its counterpart $n^S = 1 - n^F$ representing the solidity. The seepage velocity is denoted by \mathbf{w}_F , whereas $(\mathbf{u}_S)'_S$ is the material time derivative of the solid displacement vector with respect to the deforming solid skeleton. The overall stress of the model $\mathbf{T} = \mathbf{T}^S + \mathbf{T}^F$ is the sum of the partial Cauchy stress tensors of the solid and the fluid constituent, respectively.

Following this, the partial stress tensors are subjected to the principle of effective stresses (cf. [3, 16]) yielding a split into hydrostatic and so-called extra quantities

$$\mathbf{T}^S = -n^S p_{\text{hyd}} \mathbf{I} + \mathbf{T}_E^S \quad \text{and} \quad \mathbf{T}^F = -n^F p_{\text{hyd}} \mathbf{I} + \mathbf{T}_E^F, \quad (2)$$

where \mathbf{I} denotes the second-order identity tensor. As is usual in hydraulics, the fluid extra stress \mathbf{T}_E^F is neglected due to dimensional reasons, cf. [11]. In order to capture the soft tissues swelling capability, osmotic effects have to be incorporated using a further split

$$\mathbf{T}_E^S = -p_{\text{osm}} \mathbf{I} + \mathbf{T}_{E,\text{mech}}^S \quad (3)$$

of the solid extra stress into osmotic and purely mechanical contributions. Thus, the overall pressure is given by $p_{\text{tot}} = p_{\text{hyd}} + p_{\text{osm}}$. In this context, p_{osm} models the colloid osmotic pressure and is understood as the pressure difference between the internal osmotic pressure, which results from the concentrations of the NaCl-solutes and the fixed negative charges, and the external osmotic pressure arising from the NaCl-solutes of the fluid surrounding the tissue. Due to Lanir's assumption [10] stating that the dissolved ions and cations move very rapidly and do not generate concentration gradients in the tissue, van't Hoff's osmotic law

$$p_{\text{osm}} = R\Theta \left[\sqrt{4\bar{c}_m^2 + (c_m^{fc})^2} - 2\bar{c}_m \right] \quad (4)$$

can be applied to the whole domain and is not restricted to the boundary. Herein, R is the universal gas constant, Θ denotes the absolute temperature, \bar{c}_m is the molar concentration of the solutes in the surrounding (external) fluid, and c_m^{fc} is the molar concentration of the fixed negative charges with respect to the fluid volume inside the tissue. Hence, the latter quantity is deformation dependent, as volumetric deformations in the tissue directly influence the volume fraction n^F of the fluid. If a local concentration balance is postulated and integrated from initial quantities $(\cdot)_{0S}$, cf. [6], the relation

$$c_m^{fc} = c_{0S}^{fc} n_{0S}^F (J_S - n_{0S}^S)^{-1}, \quad \text{where} \quad J_S = \det \mathbf{F}_S, \quad (5)$$

can be derived for the change of the concentration of the fixed charges. As a consequence, (5)₁ depends on the solid Jacobian J_S measuring the volumetric deformation of the overall tissue.

Further constitutive assumptions concern the purely mechanical solid extra stress. We proceed from the idealization of an hyperelastic solid skeleton, which must be capable of capturing the isotropic extracellular matrix as well as the anisotropic fibre reinforcements resulting from the collagen fibres of Type I. Following [6], the resulting isotropic and anisotropic Cauchy stresses can be expressed in a decoupled manner as

$$\begin{aligned} \mathbf{T}_{E,\text{mech}}^S &:= \mathbf{T}_{E,\text{iso}}^S + \mathbf{T}_{E,\text{aniso}}^S, \quad \text{where} \\ \mathbf{T}_{E,\text{iso}}^S &= \frac{\mu_0^S}{J_S} (\mathbf{F}_S \mathbf{F}_S^T - \mathbf{I}) + \Lambda_0^S (1 - n_{0S}^S)^2 \left(\frac{1}{1 - n_{0S}^S} - \frac{1}{J_S - n_{0S}^S} \right) \mathbf{I}, \quad (6) \\ \mathbf{T}_{E,\text{aniso}}^S &= \frac{\tilde{\mu}_1^S}{J_S} I_4^{-1} (I_4^{\tilde{\gamma}_1^S/2} - 1) (\mathbf{a} \otimes \mathbf{a}) + \frac{\tilde{\mu}_1^S}{J_S} I_6^{-1} (I_6^{\tilde{\gamma}_1^S/2} - 1) (\mathbf{b} \otimes \mathbf{b}). \end{aligned}$$

Here, μ_0^S is the classical ground-state shear modulus, Λ_0^S is the second Lamé constant, $\tilde{\mu}_1^S$ and $\tilde{\gamma}_1^S$ are parameters concerning the mechanically equivalent behaviour of the collagen fibre families, where $\mathbf{a} = \mathbf{F}_S \mathbf{a}_0$ and $\mathbf{b} = \mathbf{F}_S \mathbf{b}_0$ are the fibre directions in the deformed configuration with given constant unit fibre directions \mathbf{a}_0 and \mathbf{b}_0 in the reference frame. The corresponding mixed invariants $I_4 = \mathbf{a} \cdot \mathbf{a}$ and $I_6 = \mathbf{b} \cdot \mathbf{b}$ describe the squared stretches in the respective fibre direction. Finally, the set of independent unknowns in the process is reduced by Darcy's filter law

$$n^F \mathbf{w}_F = -\frac{K_{0S}^S}{\mu^{FR}} \text{grad} p_{\text{hyd}}, \quad (7)$$

which is inserted into (1)₁. The parameters K_{0S}^S and μ^{FR} of (7) are the intrinsic permeability coefficient and the effective dynamic viscosity of the fluid, respectively, and $\text{grad}(\cdot)$ denotes the gradient with respect to the location vector \mathbf{x} of the deformed configuration.

3 Weak formulation of the binary model

For the computational model, an interval in time $[0, T]$ and a reference domain $\Omega = \Omega_0 \subset \mathbb{R}^3$ is fixed. The primary variables are the solid displacement \mathbf{u}_S and the hydrostatic pressure p_{hyd} . For a given displacement vector \mathbf{u}_S , the deformed configuration is denoted by $\Omega(\mathbf{u}_S)$, and the solid deformation gradient on $\Omega(\mathbf{u}_S)$ is computed via its inverse $\mathbf{F}_S^{-1} = \mathbf{I} - \text{grad} \mathbf{u}_S$.

Data: A specific configuration is determined by the following data: the reference domain Ω_0 , appropriate load functionals defining traction forces $\bar{\mathbf{t}}$ and the fluid efflux \bar{q} , and essential boundary conditions for

$$\begin{aligned} \mathbf{u}_S(t, \mathbf{x}) &= \mathbf{u}_S^D(t, \mathbf{x}), & \mathbf{x} \in \Gamma_S(t) \subset \partial\Omega_t, \\ p_{\text{hyd}}(t, \mathbf{x}) &= p_{\text{hyd}}^D(t, \mathbf{x}), & \mathbf{x} \in \Gamma_F(t) \subset \partial\Omega_t, \end{aligned} \quad (8)$$

on some parts of the boundary (using $\Omega_t = \Omega(\mathbf{u}_S(t))$). Due to the choice of p_{hyd} as primary variable, the model does not a priori exhibit a stress-free reference configuration. This becomes clear when (3) to (6) are combined in order to compute the overall stress of the model, thereby using values of the natural state, i. e., $\mathbf{u}_S = \mathbf{0}$ and $p_{\text{hyd}} = 0$. Due to (4), there is always an initial osmotic pressure

$$p_{\text{osm,OS}} = R\Theta \left[\sqrt{4\bar{c}_m^2 + (c_{0S}^{fc})^2} - 2\bar{c}_m \right]. \quad (9)$$

Hence, the constant part $p_{\text{osm,OS}} \mathbf{I}$ is added onto the mechanical extra stress (6)₁ to enforce a stress free reference configuration in the sense of classical continuum mechanics. Note that without this modification, the model would describe an initial swelling of the tissue until equilibrium between (9) and the

tension in the mechanical extras stress $(6)_1$ is reached. As this contribution is concerned with numerical solution strategies, the described simpler approach by directly starting with the initial osmotic pressure (9) is used here.

Finally, the model also depends on several material parameters. For a full set of suitable parameters please refer to Table 1 in Section 5.

Variational formulation: With these settings, it is now possible to state the full biphasic problem at time $t \in [0, T]$: for a given traction vector $\bar{\mathbf{t}}$ and a given efflux \bar{q} of the interstitial fluid find \mathbf{u}_S and p_{hyd} satisfying the essential boundary conditions and the balance equations in weak form

$$\begin{aligned} \int_{\Omega_t} \mathbf{T}_{E,\text{mech}}^S \cdot \text{grad } \mathbf{v} \, dv - \int_{\Omega_t} p_{\text{tot}} \text{div } \mathbf{v} \, dv &= \int_{\partial\Omega_t} \bar{\mathbf{t}} \cdot \mathbf{v} \, da, \\ \int_{\Omega_t} \text{div} (\mathbf{u}_S)'_S q \, dv + \int_{\Omega_t} \frac{K_{0S}^S}{\mu^{FR}} \text{grad } p_{\text{hyd}} \cdot \text{grad } q \, dv &= \int_{\partial\Omega_t} \bar{q} q \, da \end{aligned} \quad (10)$$

for all test functions \mathbf{v} and q satisfying $\mathbf{v} = \mathbf{0}$ on $\Gamma_S(t)$ and $q = 0$ on $\Gamma_F(t)$. Here, $\mathbf{T}_{E,\text{mech}}^S$ depends (non-linearly) on the deformation gradient, and p_{tot} depends on its determinant.

For simplicity, the abbreviations $\mathbf{u} = \mathbf{u}_S$ and $p = p_{\text{hyd}}$ are used in the following.

Discretization in time: For a given time series $0 = t_0 < t_1 < t_2 < \dots < T$, the backward Euler method reads as follows: for a given \mathbf{u}^{n-1} depending on $\Delta t_n = t_n - t_{n-1}$, $\bar{\mathbf{t}}_n = \bar{\mathbf{t}}(t_n)$ and $\bar{q}_n = \bar{q}(t_n)$, the unknowns \mathbf{u}^n and p^n of the time step n are computed satisfying the essential boundary conditions

$$\begin{aligned} \mathbf{u}^n(\mathbf{x}) &= \mathbf{u}_S^D(t_n, \mathbf{x}), & \mathbf{x} \in \Gamma_S^n &:= \Gamma_S(t_n), \\ p^n(\mathbf{x}) &= p_{\text{hyd}}^D(t_n, \mathbf{x}), & \mathbf{x} \in \Gamma_F^n &:= \Gamma_F(t_n), \end{aligned} \quad (11)$$

and

$$\begin{aligned} R_S^n(\mathbf{u}^n, p^n)[\mathbf{v}] &= 0, & \text{for all } \mathbf{v} \text{ with } \mathbf{v} &= \mathbf{0} \text{ on } \Gamma_S^n, \\ R_F^n(\mathbf{u}^n, p^n)[q] &= 0, & \text{for all } q \text{ with } q &= 0 \text{ on } \Gamma_F^n, \end{aligned} \quad (12)$$

where the residuals are given by

$$\begin{aligned} R_S^n(\mathbf{u}, p)[\mathbf{v}] &= \int_{\Omega(\mathbf{u})} \mathbf{T}_{E,\text{mech}}^S(\text{grad } \mathbf{u}) \cdot \text{grad } \mathbf{v} \, dv \\ &\quad - \int_{\Omega(\mathbf{u})} [p + p_{\text{osm}}(\text{grad } \mathbf{u})] \text{div } \mathbf{v} \, dv - \int_{\partial\Omega(\mathbf{u})} \bar{\mathbf{t}}_n \cdot \mathbf{v} \, da, \\ R_F^n(\mathbf{u}, p)[q] &= - \int_{\Omega(\mathbf{u})} \text{div} (\mathbf{u} - \mathbf{u}^{n-1}) q \, dv \\ &\quad - \Delta t_n \int_{\Omega(\mathbf{u})} \frac{K_{0S}^S}{\mu^{FR}} \text{grad } p \cdot \text{grad } q \, dv + \Delta t_n \int_{\partial\Omega(\mathbf{u})} \bar{q}_n q \, da. \end{aligned} \quad (13)$$

Discretization in space: In the special case of small deformations and $\Delta t_n K_{0S}^S/\mu^{FR} \approx 0$, the incremental problem is close to a saddle point problem: Compute \mathbf{w} and r satisfying

$$\begin{aligned} \int_{\Omega} (\mathbb{C} \operatorname{grad} \mathbf{w}) \cdot \operatorname{grad} \mathbf{v} \, dv - \int_{\Omega} r \operatorname{div} \mathbf{v} \, dv &= -R_S[\mathbf{v}], \\ - \int_{\Omega} \operatorname{div} \mathbf{w} q \, dv &= -R_F[q] \end{aligned} \quad (14)$$

for all \mathbf{v} with $\mathbf{v} = \mathbf{0}$ on Γ_S^n and q with $q = 0$ on Γ_F^n . This system has the same structure as the Stokes system. Thus, in order to avoid oscillations, a stable discretization $\mathbf{u}_h \in \mathbf{V}_h$ and $p_h \in Q_h$ satisfying the inf-sup condition

$$\sup_{\mathbf{v}_h \neq \mathbf{0}} \frac{\int_{\Omega} q_h \operatorname{div} \mathbf{v}_h \, dv}{\left(\int_{\Omega} \mathbb{C} \operatorname{grad} \mathbf{v}_h \cdot \operatorname{grad} \mathbf{v}_h \, dv \right)^{1/2}} \geq \beta \left(\int_{\Omega} q_h^2 \, dv \right)^{1/2} \quad (15)$$

for all $q_h \in Q_h$ with $\int_{\Omega} q_h \, dv = 0$ has to be used, where β is a constant which is independent of the mesh width. In this context, numerically stable Taylor-Hood elements (Q_2/Q_1) are applied with isoparametric 20-node bricks for the displacements \mathbf{u} and trilinear pressure p , see [2].

Consistent Newton iteration: In every time step, choose suitable start iterates $\mathbf{u}^{n,0}$ and $p^{n,0}$ satisfying the essential boundary conditions (11), and for $k = 1, 2, 3, \dots$ compute increments \mathbf{w} and r (with homogeneous boundary conditions on the Dirichlet boundary parts) by solving the linearized variational problem of the form

$$\begin{aligned} a_{SS}^{n,k}(\mathbf{w}, \mathbf{v}) + a_{FS}^{n,k}(r, \mathbf{v}) &= -R_S^n(\mathbf{u}^{n,k-1}, p^{n,k-1})[\mathbf{v}], \\ a_{SF}^{n,k}(\mathbf{w}, q) + a_{FF}^{n,k}(r, q) &= -R_F^n(\mathbf{u}^{n,k-1}, p^{n,k-1})[q], \end{aligned} \quad (16)$$

for all test functions \mathbf{v} and q with homogeneous boundary conditions on the Dirichlet boundary parts. The bilinear forms $a_{SS}^{n,k}(\cdot, \cdot)$ and $a_{FS}^{n,k}(\cdot, \cdot)$ are the derivatives of $R_S^n(\cdot)$ with respect to the solid and the fluid component at $(\mathbf{u}^{n,k}, p^{n,0})$, and $a_{SF}^{n,k}(\cdot, \cdot)$, $a_{FF}^{n,k}(\cdot, \cdot)$ are the derivatives of $R_F^n(\cdot)$.

Then, a suitable damping factor $s^{n,k} \in (0, 1]$ is determined such that for the updated variables

$$\begin{aligned} \mathbf{u}^{n,k} &= \mathbf{u}^{n,k-1} + s^{n,k} \mathbf{w}, \\ p^{n,k} &= p^{n,k-1} + s^{n,k} r \end{aligned} \quad (17)$$

the residual norm is decreasing. If no such damping parameter is found, the time increment Δt_n is reduced. Close to the solution of the incremental problem it is expected that no damping is necessary, i. e., $s^{n,k} = 1$.

4 A parallel linear solver

The porous media model is realized in the FEM research software PANDAS [5, 15], and a parallel front end for assembling and solving the system is provided by M++ (see [18, 19] for details on the parallel programming model and for the definition of general interfaces). The main feature of this software is a geometry-based data structure relying on the concept of distributed objects, where every object is associated to a geometric point. In particular, the unknowns are associated to their nodal points. This allows for a transparent realization of the parallel consistency requirements for the finite element solution along the parallel interface.

Within the non-linear and time-dependent simulation, the most sensible part of the parallelization is the solution of the linear problems within every Newton step. Here, we use a parallel GMRES method, as is described in [19], together with a domain decomposition preconditioner.

From numerical experiments it is well-known that overlapping domain decomposition preconditioners with coarse grid correction applied to the Stokes system with Taylor-Hood elements are very efficient, see [8, 9]. Hence, this type of preconditioning is a good choice for the discussed application to complex bio-mechanical structures, although two major modifications are required due to the following reasons: Only a moderate number of processors is used so that the subdomain problems are too large for exact solving. Moreover, the underlying geometry is too complex to allow for a small coarse mesh. Thus, an inexact sub-domain solver is used (a multilevel ILU with pivoting and dropping strategy by Mayer [12, 13]) and the coarse problem is constructed on an independent overlay mesh.

Altogether, this preconditioner can easily be constructed within the parallel interface, i. e., it requires only algebraic and geometric information and it is, thus, fully decoupled from the modelling and finite element discretization provided by PANDAS.

5 Numerical experiments

For the numerical application to the human lumbar spine we use the material model described in section 2 with three different sets of parameters listed in Table 1. Herein, the vertebrae are considered as a homogeneous uncharged hard tissue, thereby neglecting its original structure consisting of a dense cortical shell and a soft spongiosa inside. Furthermore, the AF and NP of the IVD are modelled with all occurring inhomogeneities as is described in [6]. In this context, the parameters addressing the mechanical behaviour of the collagen fibres are only given at selected points, i. e., at internal and external regions in dorsal and ventro-lateral positions, which are needed for a linear interpolation in the AF.

The presented initial boundary value problems concern a lumbar spine with removed processes, one having healthy IVD's and another having the

lowest motion segment stiffened, i. e., the lowest IVD behaves like a vertebra. Moreover, all free surfaces are drained ($p_{\text{hyd}} = 0$), the lower surface of the L5-vertebra is totally fixed in space ($\mathbf{u}_S = \mathbf{0}$), and the top surface of the L1-vertebra is loaded with the traction vector $\bar{\mathbf{t}}$, which results in a vertical (F_V) and horizontal (F_H) force when integrated over the surface. The traction vector is then linearly increased with time, until the healthy and the stiffened lumbar spine show a tip deflection of 54.3 mm. The corresponding tip-loads are $F_V = 85$ N, $F_H = 21$ N and $F_V = 108$ N, $F_H = 27$ N with loading times $t = 0.201$ s and $t = 0.255$ s for the healthy and the stiffened spine, respectively. Results of the 3-d simulation are depicted in Figure 1 showing the total pressure in the sagittal plane of the spine.

Vertebrae: Treated with no distinction between cortical shell and spongiosa.				
$n_{0S}^S = 0.2$	[-]	$K_{0S}^S = 2.7 \cdot 10^{-5}$	[mm ²]	
$c_{0S}^{fc} = 0.0$	[mol/mm ³]	$\mu^{FR} = 3.8 \cdot 10^{-8}$	[Ns/mm ²]	
$\mu_0^S = 192.0$	[MPa]	$\Lambda_0^S = 225.7$	[MPa]	
Nucleus Pulposus: Treated as isotropic and charged material.				
$n_{0S}^S = 0.3$	[-]	$K_{0S}^S = 3.5 \cdot 10^{-12}$	[mm ²]	
$c_{0S}^{fc} = 0.3 \cdot 10^{-6}$	[mol/mm ³]	$\mu^{FR} = 6.9 \cdot 10^{-10}$	[Ns/mm ²]	
$\mu_0^S = 0.5$	[MPa]	$\Lambda_0^S = 0.75$	[MPa]	
Anulus Fibrosus: Treated as inhomogeneous anisotropic charged material.				
$n_{0S}^S = 0.3$	[-]	$K_{0S}^S = 6.2 \cdot 10^{-12}$	[mm ²]	
$c_{0S}^{fc} = 0.1 \cdot 10^{-6}$	[mol/mm ³]	$\mu^{FR} = 6.9 \cdot 10^{-10}$	[Ns/mm ²]	
$\mu_0^S = 0.95$	[MPa]	$\Lambda_0^S = 2.2$	[MPa]	
		Ventro-Lat. Int.	Ventro-Lat. Ext.	Dorsal Int. Dorsal Ext.
$\bar{\mu}_1^S$ [MPa]	0.0343	0.1463	0.0059	0.0508
$\bar{\gamma}_1^S$ [-]	44.051	97.135	30.464	54.239

Table 1. Material parameters of the biphasic model for the vertebrae, nucleus pulposus and anulus fibrosus, respectively.

The lumbar spine was discretized using 72 320 20-node Taylor-Hood elements yielding a total of 982 044 degrees of freedom. The computations were carried out in parallel on the cluster “Leonardo da Vinci” of the Institute of Applied Mechanics (CE) at the Universität Stuttgart, using 84 CPU’s (2.2 GHz Opteron with 1 GB RAM/CPU). The full simulation time was 5:44 [h:min] and 11:32 [h:min] for the healthy and the stiffened spine, respectively. In both computations a fixed time increment $\Delta t_n = 0.003$ s is used.

As expected, the force which is required to accomplish the same deformation with the stiffened lumbar spine is remarkably higher than the force needed for the healthy lumbar spine. Moreover, the maximum total intradiscal

pressure p_{tot} in the L3-L4 disc is also raised from 0.7 MPa to 1.0 MPa comparing the healthy with the stiffened state. Note that this is even a higher value than the 0.95 MPa of total disc-pressure reached in the healthy L4-L5 disc. Hence, it is obvious that the stiffening of a motion segment causes a surplus load in the adjacent IVD, when deformations are kept constant.

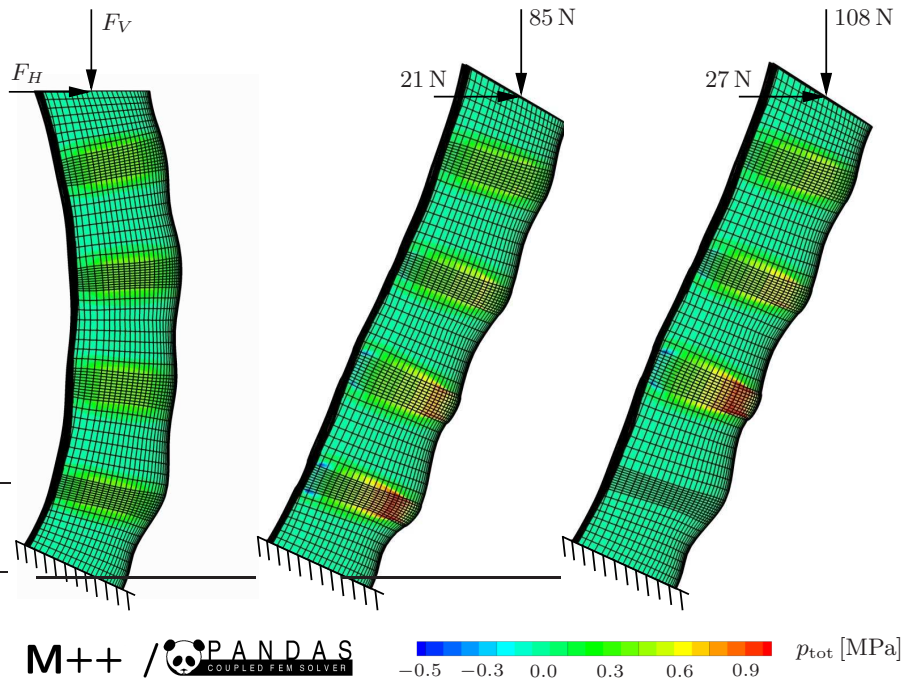


Fig. 1. Sagittal cut illustrating the load-deformation behaviour and the total pressure development inside the IVD's for a healthy lumbar spine (middle) and one having the L4-L5 motion segment stiffened (right). The reference configuration is shown on the left.

References

1. Ayad, S. & Weiss, J. B.: Biochemistry of the intervertebral disc. In Jayson, M. I. V. (ed.): *The Lumbar Spine and Back Pain*, 3rd ed., Churchill Livingstone, New York, 1987, pp. 100–137.
2. Brezzi, F. & Fortin, M.: *Mixed and Hybrid Finite Element Methods*. Springer-Verlag, Berlin, 1991.
3. Ehlers, W.: Constitutive equations for granular materials in geomechanical context. In Hutter, K. (ed.): *Continuum Mechanics in Environmental Sciences and Geophysics*, CISM Courses and Lectures No. 337, Springer-Verlag, Wien, 1993, pp. 313–402.

4. Ehlers, W.: Foundations of multiphasic and porous materials. In Ehlers, W. & Bluhm, J. (eds.): *Porous Media: Theory, Experiments and Numerical Applications*, Springer-Verlag, Berlin, 2002, pp. 3–86.
5. Ehlers, W. & Ellsiepen, P.: PANDAS: Ein FE-System zur Simulation von Sonderproblemen der Bodenmechanik. In Wriggers, P.; Meißner, U.; Stein, E. & Wunderlich, W. (eds.): *Finite Elemente in der Baupraxis: Modellierung, Berechnung und Konstruktion*, Beiträge zur Tagung FEM '98 an der TU Darmstadt am 5. und 6. März 1998, Ernst & Sohn, Berlin, 1998, pp. 391–400.
6. Ehlers, W.; Karajan, N. & Markert, B.: A porous media model describing the inhomogeneous behaviour of the human intervertebral disc. *Materials Science and Engineering Technology* **37** (2006), 546–551.
7. Ehlers, W.; Markert, B. & Karajan, N.: A coupled FE analysis of the intervertebral disc based on a multiphasic TPM formulation. In Holzapfel, G. A. & Ogden, R. W. (eds.): *Mechanics of Biological Tissue*, Springer, Berlin, 2006, pp. 373–386.
8. Klawonn, A. & Pavarino, L. F.: Overlapping Schwarz methods for mixed linear elasticity and Stokes problems. *Computer Methods in Applied Mechanics and Engineering* **165** (1998), 233–245.
9. Klawonn, A. & Pavarino, L. F.: A comparison of overlapping Schwarz methods and block preconditioners for saddle point problems. *Numerical Linear Algebra with Applications* **7** (2000), 1–25.
10. Lanir, Y.: Biorheology and fluid flux in swelling tissues. I. Bicomponent theory for small deformations, including concentration effects. *Biorheology* **24** (1987), 173–187.
11. Markert, B.: *Porous media viscoelasticity with application to polymeric foams*. Dissertation, Bericht Nr. II-11 aus dem Institut für Mechanik (Bauwesen), Universität Stuttgart, 2005.
12. Mayer, J.: A multilevel crout ilu preconditioner with pivoting and row permutation. *Numerical Linear Algebra with Applications*, 2007. To appear.
13. Mayer, J.: Symmetric permutations for I-matrices to delay and avoid small pivots. *SIAM Journal on Scientific Computing*, 2007. To appear.
14. Mow, V. C. & Hayes, W. C.: *Basic orthopaedic biomechanics*. Lippincott-Raven, New York, 1997.
15. PANDAS: Porous media Adaptive Non-linear finite element solver based on Differential Algebraic Systems. <http://www.get-pandas.com>
16. Skempton, A. W.: Significance of Terzaghi's concept of effective stress (Terzaghi's discovery of effective stress). In Bjerrum, L.; Casagrande, A.; Peck, R. B. & Skempton, A. W. (eds.): *From Theory to Practice in Soil Mechanics*, Wiley, New York, 1960, pp. 42–53.
17. Urban, J. P. G. & Roberts, S.: Intervertebral disc. In Comper, W. D. (ed.): *Extracellular Matrix, Volume 1, Tissue Function*, Harwood Academic Publishers GmbH, 1996, pp. 203–233.
18. Wieners, C.; Ammann, M. & Ehlers, W.: Distributed point objects: A new concept for parallel finite elements applied to a geomechanical problem. *Future Generation Computer Systems* **22** (2006), 532–545.
19. Wieners, C.; Ammann, M.; Ehlers, W. & Graf, T.: Parallel Krylov methods and the application to 3-d simulations of a tri-phasic porous media model in soil mechanics. *Computational Mechanics* (2005) **36**, 409–420.

Experimental-Numerical Studies of Impaction Loading of Osteochondral Grafts

U.-J. Görke¹, A. Bucher¹, R. Kreißig¹, H. Günther² & M. A. Wimmer³

¹ Institute of Mechanics, Chemnitz University of Technology,
Straße der Nationen 62, 09111 Chemnitz, Germany

² TBZ-Pariv, Chemnitz and AO Research Institute, Davos,
Liddy-Ebersberger-Straße 41, 09127 Chemnitz, Germany

³ Department of Orthopedics, Rush University Medical Center,
1653 W. Congress Parkway, Chicago, IL 60612, USA

Abstract. Osteochondral grafting is one of the treatment options to repair damaged cartilage. However, the surgical impaction of the osteochondral plug to anchor it into the defect site can be traumatic and subsequently cause cell death and cartilage degeneration. Little is known about the relationship between mechanical loading and biological response.

An experimental-numerical approach of cartilage impaction is presented. Bovine plugs were hit in a controlled laboratory setting using different impaction devices to simulate the surgical procedure. A comparison between field (surgeon) and experimental (lab) data was performed.

Numerical simulations were then conducted to better understand the underlying mechanobiological processes. A commercially available FE-code, improved by utilizing sophisticated material models, has been used. The theoretical background of the material model is presented, based on an overlay concept. The spatial distributions of mechanical field variables are compared to biological endpoints (e. g. live-dead cell assays).

1 Clinical Background

Changes in demographics and recreational habits of modern industrial societies have caused a substantial increase of joint disease and associated health care costs. Articular cartilage lesions can be debilitating and initiate degenerative processes of the joint. In 1998 in Germany alone about 5 millions patients¹ suffered from degenerative osteoarthritis with far-reaching consequences in quality of life.

Articular cartilage is an avascular tissue (i. e. blood vessels are absent) with a limited capacity of self-repair. Consequently, joint injuries do not heal satisfactorily. Several methods to repair cartilage lesions are routinely used or subject of worldwide research activities. Among these, osteochondral grafting involving either autogenic or allogenic tissues is a common clinical procedure

¹ Informationssystem für Gesundheitsberichterstattung des Statistischen Bundesamtes, 1998

for cartilage repair. Osteochondral grafts are bone-cartilage plugs of cylindrical shape which are harvested from undamaged and non-weightbearing joint areas. These plugs are then implanted into the damaged cartilage areas through press-fitting, i. e. so-called recipient holes with slightly negative tolerances are prepared.

Compared with alternative treatment options the osteochondral grafting is of interest because the lesion is replaced with true hyaline cartilage. Though, osteochondral grafting is indicated only for focal cartilage defects (lesions up to 10 cm^2). In order to anchor the plugs in the recipient hole they are press fitted through impaction. Typically, a surgical mallet is used for tapping. Recently, it has been shown that the insertion process of osteochondral grafts causes cell death, particularly in the superficial zone [2]. Primarily, this process is apoptotic which may cause progressive degeneration of the cartilaginous tissue over time.

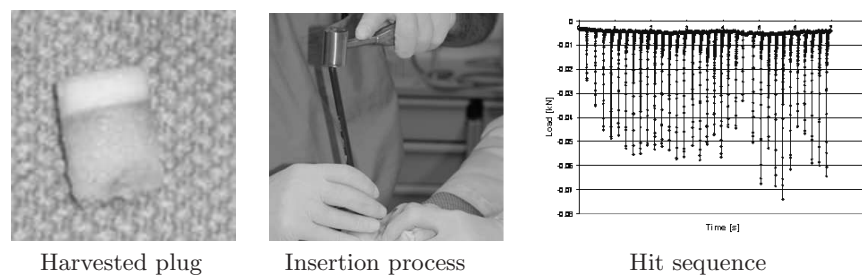


Fig. 1. Harvested osteochondral autograft plug prior to implantation. Implantation of the graft using a plastic tamp device and a surgical mallet (OATS system, Arthrex Inc.). Typical hit sequence showing that the surgeon applies load levels between 50 and 75 N and 33 hits with an overall impulse of 7 Ns [20].

Figure 1 shows the tapping procedure using the OATS (**O**steochondral **A**utograft **T**ransfer **S**ystem) procedure (Arthrex Inc.), and a typical tapping sequence of a graft implantation performed at the Rush University Medical Centre, Chicago (USA).

2 Experimental Studies

Currently, little is known about the mechanobiological processes in articular cartilage which are initiated by impaction loading. At the Rush University Medical Centre, Chicago (USA) several experimental studies have been performed focusing on the viability of chondrocytes in osteochondral grafts that had been impact loaded by the original surgical instruments. Using mechanical testing devices in conjunction with high speed video analysis, the deformation of cartilage during impaction has been studied [14, 15, 20]. Based

on the experimental results, at present numerical studies are performed to analyse correlations between mechanical loading conditions of chondrocytes and their typical response resulting in tissue degeneration due to the transplantation process. The coordinated experimental-numerical approach aimed at numerical (*in silico*) experiments providing data for the improvement of osteochondral grafting procedures.

Two *in vitro* studies with 45 osteochondral plugs in total were performed. 8 mm diameter grafts were harvested from the trochlear region of bovine knee joints using the Arthrex OATS system. Once these plugs were obtained, the bone was trimmed so that the entire length of the plugs was 10 mm. Using the original plastic tamp device (modified with a load cell), and a surgical hammer the donor plugs were placed into recipient holes at the condyles of the knee joint (Figure 1). The plugs from the recipient holes served as unloaded controls. At the end of defined time intervals (0, 4, and 8 days respectively) the re-implanted grafts were removed from the culture, and a 2 mm×2 mm portion of each plug was stained for analysis of cell viability using a confocal laser-scanning microscope. Additionally, these *in vitro* studies served as basis to characterise the impaction profiles in a mechanical sense to calibrate reproducible compression tests. In Figure 1 a typical hit sequence of the clinically observed re-implantation process is shown. Among the various aspects of characterizing the impaction process mechanically the reader’s attention should be focused on the mean overall impulse of 6.98 Ns as a measure of the clinical relevant overall intensity of the impact sequence necessary to anchor the graft in the recipient hole.

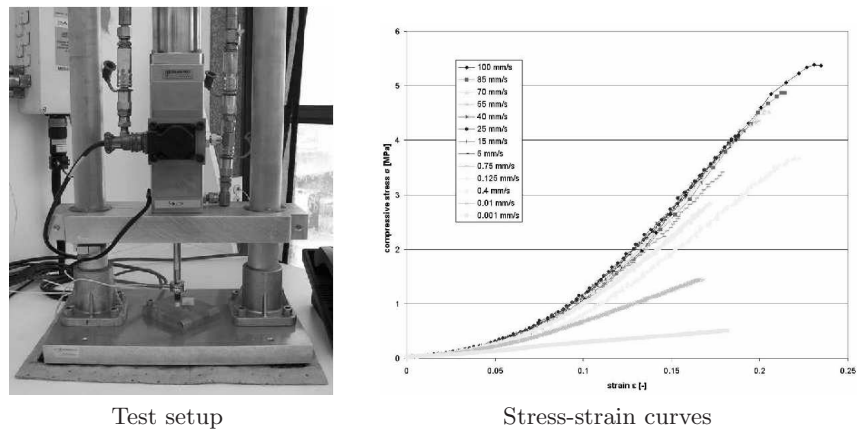


Fig. 2. Quasi-unconfined compression tests of bovine osteochondral grafts on a 5 kN DARTEC servo-hydraulic testing machine (9000-series). Analysis of the rate dependent stress-strain behaviour.

In order to analyse the characteristic material properties relevant for the constitutive modelling in case of impact loading and to produce data for the calibration of the material model, quasi-unconfined compression tests of osteochondral grafts have been performed on a material testing machine using set velocities (see Figure 2). The subchondral bone plug was clamped into a fixation device simulating a compression state as in the clinical situation. Deformation rates were varied in the range of 0.001 mm s^{-1} to 100 mm s^{-1} . The conditions under high impact velocity corresponded to the clinically relevant deformation of approximately 15% of the initial height of the cartilage layer applied in about 3 ms. As can be seen in Figure 2, the rate-dependent nonlinear stress-strain curves show an increase of the global graft stiffness with increasing deformation rate, but with a beginning saturation of this effect at about 1 mm s^{-1} . Obviously, the low permeability of articular cartilage causes a high hydrostatic pressure within the tissue as the interstitial fluid cannot flow out of the graft during the loading time.

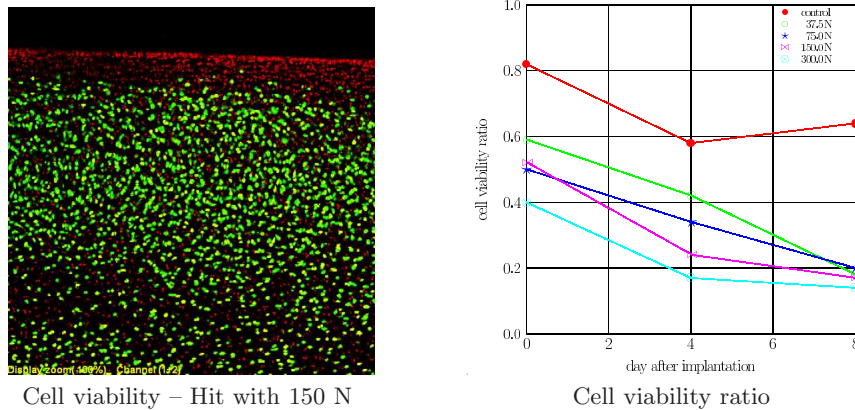


Fig. 3. Cross-section of the graft with superficial zone at the top, green: living cells, red: dead cells. Analysis of the cell viability over time shows time and load dependency.

The deformation process was further studied using grey scale correlation image analysis. In particular, differences between layers were studied. Based on high-speed video images of the compression process, a sequence of pictures documenting the deformation of cartilage was extracted.

To provide systematic and reproducible studies of the cell viability dependent on the overall intensity of impact during osteochondral grafting impact tests with a pneumatic device for controlled impulse application have been performed. The device shows improved reproducible single hit load-time characteristics compared with the material testing machine [10]. Clamped osteochondral grafts were subjected to uniform hit sequences at different load

levels (37.5 N, 75 N, 150 N, and 300 N respectively). The number of hits was defined in accordance to the previously identified overall impulse.

In Figure 3 the changes in cell viability dependent on the load magnitude and the time after implantation of the grafts in comparison to unloaded controls are shown. Analysing these results two effects can be discussed: Initial cell death related to mechanical loading of the chondrocytes is observed. Expectedly, the cell viability ratio decreases with increasing load magnitude. However, an adjustment of the cell viability ratio could be observed over time which appears to be independent of load magnitude and therefore may be impulse driven (which was held constant in this experiment). We speculate that a secondary apoptotic cell response affects cell viability after impaction. At present the exact cell signalling pathway is unknown but mechanical load definitely plays a role.

3 Material Model and Numerical Simulation

3.1 Material Characteristics of Articular Cartilage

According to its function, namely low friction and high wear resistance, articular cartilage presents itself as a complex hydrated composite structure (cf. [12, 13] and others). It consists of a porous, permeable and deformable solid skeleton which is completely filled with a fluid component (interstitial fluid). Cartilage cells (chondrocytes) are embedded in the extracellular matrix (ECM) consisting of a network of collagen fibres, and embedded proteoglycans, glycoproteins and several kinds of lipids. Typically, articular cartilage is subdivided into four zones, which differ in volume ratio and morphology of the constituents.

Early biomechanical approaches based themselves on the description of the mechanical behaviour of organic tissue by means of isotropic linear-elastic models. Recent theoretical and computational capabilities permit improved modelling of biological tissue even considering their discrete structural components. Thus, as a matter of principle, it became possible to utilise more complex material models developed for technical problems also for biomechanical simulations. There are a huge number of publications dealing with the material behaviour of hyaline articular cartilage, and its appropriate modelling (for an overview cf. [9]).

We propose a biphasic phenomenological macrostructural approach describing microstructural effects by means of suitable constitutive equations. The thermodynamically consistent material model is based on a so-called overlay concept illustrating the assumption of the superposition of stress, and assuming an additive decomposition of the stress tensor as well as the free Helmholtz energy density. Within this context, the material to be analysed is assumed to be fictitiously composed of several “layers”. Each layer is characterised by original material properties but the same deformation under mechanical loading. Consequently, in each layer a unique stress response on

external loads can be obtained which usually differs from that one in the other layers (about the basic idea of the overlay concept and its biomechanical application see [16, 17]). Concerning the current state of the art it is generally recognised that articular cartilage is subjected to finite deformations. Due to the varying orientation of the collagen fibres the solid matrix of the cartilage tissue has to be considered as an anisotropic elastic material additionally characterised by tension-compression nonlinearities. Typically, the rate-dependency of a biphasic material behaviour is exclusively attributed to the fluid flow through the solid matrix. However, recent observations demonstrate that viscoelastic properties of the solid phase must not be neglected. Therefore, its intrinsic viscoelasticity is considered by appropriate constitutive relations.

3.2 Viscoelastic Biphasic Constitutive Theory

It is generally accepted in the literature that articular cartilage can be regarded as a saturated porous media. Within the context of material modelling, the theory of porous media is based on the mixture approach of immiscible components (see e. g. Bowen [3], Prevost [18], de Boer [1] and Ehlers [4, 6]). Recently, this theory has been increasingly applied to soft biological tissues.

Like in the continuum mechanics of single-phase materials, the governing equations for multiphase materials (local balance laws) must be completed by constitutive equations. Equation (1) describes the stress decomposition for the mixture

$$\mathbf{T} = \mathbf{T}^S + \mathbf{T}^F = \mathbf{T}_E^S - pJ\mathbf{C}^{-1}. \quad (1)$$

Variables in (1) are defined as follows: second Piola-Kirchhoff stress tensors \mathbf{T} for the mixture, \mathbf{T}^S for the solid phase as well as \mathbf{T}^F for the fluid phase, the deformation gradient \mathbf{F} ($J = \det\mathbf{F}$), the right Cauchy-Green tensor \mathbf{C} , and the effective fluid pressure (pore pressure) p . The presence of the effective fluid pressure term indicates the impact of the fluid flow on the deformable solid skeleton. The development of the effective second Piola-Kirchhoff stress \mathbf{T}_E^S is governed by the solid deformation as well as nonmechanical processes, and needs its own material law. Our custom formulation for the effective solid stress, including anisotropic rate-dependent effects, is presented below.

Combining the first and the second laws of thermodynamics, and considering some well-established constitutive assumptions, the following material description of the dissipation inequality for isothermal processes can be obtained for the mixture

$$-\varrho_0^S \dot{\psi}^S + \frac{1}{2} \mathbf{T}_E^S \cdot \dot{\mathbf{C}} \geq 0. \quad (2)$$

Here ψ^S denotes the free Helmholtz energy density of the solid phase, and ϱ_0^S the partial solid phase density with respect to the reference configuration

of the solid phase. Time derivatives denote the material time derivative with respect to the reference configuration of the solid phase.

As mentioned above, the presented material model is based on the overlay concept. The basic idea of this concept can be impressively explained on the uniaxial simplification of complex material models in case of small deformations. For physical reasons, the formulation of these models can be based on rheological systems consisting of several elements, including springs, dashpots and friction elements (see e. g. [11]). For three-dimensional finite deformations the overlay concept is equivalent to a multiplicative split of the deformation gradient. To model cartilage behaviour, the deformation gradient is assumed to be split into an elastic part \mathbf{F}_e and a viscous part \mathbf{F}_v (see e. g. [5, 11, 19])

$$\mathbf{F} = \mathbf{F}_e \mathbf{F}_v. \quad (3)$$

A (physically incompatible) viscous intermediate configuration is now defined in addition to the reference and current configurations. Consequently, the following additive decomposition of the effective stress is proposed

$$\mathbf{T}_E^S = \mathbf{T}_{\text{eq0}} + \mathbf{T}_{\text{ov}} \quad (4)$$

with \mathbf{T}_{eq0} representing the hyperelastic equilibrium state. The stress tensor \mathbf{T}_{ov} defines the viscous overstress due to the intrinsic viscoelasticity of the solid phase. Without any loss of generality, only one overstress variable will be used to present the definition of the constitutive relations.

According to the additive split of the stress tensor, the following consistent representation of the free Helmholtz energy density ψ^S will be assumed

$$\psi^S = \psi_{\text{eq0}}(\mathbf{C}) + \psi_{\text{ov}}(\widehat{\mathbf{C}}_{\text{ev}}) \quad \text{with} \quad \widehat{\mathbf{C}}_{\text{ev}} = \mathbf{F}_v^{-\text{T}} \mathbf{C} \mathbf{F}_v^{-1}. \quad (5)$$

With (4) and (5) and some algebra, the dissipation relation (2) becomes

$$\begin{aligned} & \left\{ \left[-\varrho_0^S \frac{\partial \psi_{\text{eq0}}}{\partial \mathbf{C}} + \frac{1}{2} \mathbf{T}_{\text{eq0}} \right] + \left[-\varrho_0^S \mathbf{F}_v^{-1} \frac{\partial \psi_{\text{ov}}}{\partial \widehat{\mathbf{C}}_{\text{ev}}} \mathbf{F}_v^{-\text{T}} + \frac{1}{2} \mathbf{T}_{\text{ov}} \right] \right\} \cdot \dot{\mathbf{C}} \\ & + 2 \varrho_0^S \mathbf{F}_v^{-1} \frac{\partial \psi_{\text{ov}}}{\partial \widehat{\mathbf{C}}_{\text{ev}}} \mathbf{F}_v^{-\text{T}} \mathbf{C} \cdot \mathbf{F}_v^{-1} \dot{\mathbf{F}}_v \geq 0. \end{aligned} \quad (6)$$

Using relation (6), stress-strain relations for the hyperelastic equilibrium and the viscous overstress state can be written

$$\mathbf{T}_{\text{eq0}} = 2 \varrho_0^S \frac{\partial \psi_{\text{eq0}}}{\partial \mathbf{C}}, \quad \mathbf{T}_{\text{ov}} = 2 \varrho_0^S \frac{\partial \psi_{\text{ov}}}{\partial \mathbf{C}} \quad (7)$$

with

$$\psi_{\text{eq0}} = \psi_{\text{eq0}}(\mathbf{C}, \mathbf{M}), \quad \psi_{\text{ov}} = \psi_{\text{ov}}(\mathbf{C} \mathbf{C}_v^{-1}, \mathbf{M}_v). \quad (8)$$

Structural tensors $\mathbf{M} = \mathbf{A} \otimes \mathbf{A}$ and $\mathbf{M}_v = \mathbf{F}_v^{-1} (\widehat{\mathbf{A}}_v \otimes \widehat{\mathbf{A}}_v) \mathbf{F}_v^{-\text{T}}$ define the preferred fibre directions. At hyperelastic equilibrium, the directional vectors

\mathbf{A} and \mathbf{A}_v must coincide for the same structural elements. An equation for the viscous part of the deformation gradient can be written

$$\dot{\mathbf{F}}_v = \frac{1}{\eta_v} \mathbf{F}_v \mathbf{T}_{ov} \mathbf{C} \quad \text{with} \quad \eta_v > 0. \quad (9)$$

The elastic and viscous potentials (ψ_{eq0} and ψ_{ov} respectively) are isotropic tensor functions, and are assumed to be decomposed into isotropic and transversely isotropic parts (10) and (11)

$$\psi_{eq0} = \psi_{eq0}^{iso}(I, II, III) + \psi_{eq0}^{aniso}(I_4), \quad (10)$$

$$\psi_{ov} = \psi_{ov}^{iso}(I_{ov}, II_{ov}, III_{ov}) + \psi_{ov}^{aniso}(I_{4ov}). \quad (11)$$

Strain invariants I , II , III and I_4 for the overall strain tensor and the corresponding structural tensor are defined as

$$I = \text{tr} \mathbf{C}, \quad II = \frac{1}{2} \left((\text{tr} \mathbf{C})^2 - \text{tr} \mathbf{C}^2 \right), \quad III = \det \mathbf{C}, \quad (12)$$

$$I_4 = \text{tr}(\mathbf{M}\mathbf{C}). \quad (13)$$

Invariants for the viscous potential, I_{ov} , II_{ov} , III_{ov} and I_{4ov} , are equivalent to (12) and (13). The viscosity function η_v was defined in accordance with Lion [11]

$$\eta_v = \eta_{v0} \exp \left[-\frac{1}{s_o} \frac{\|\widehat{\mathbf{T}}_{ov}\|}{\|\widehat{\mathbf{G}}\|^3} \right] \quad (14)$$

with

$$\|\widehat{\mathbf{T}}_{ov}\| = \sqrt{\text{tr} \left((\mathbf{T}_{ov} \mathbf{C}_v)^2 \right)}, \quad \|\widehat{\mathbf{G}}\| = \sqrt{\text{tr} (\mathbf{C}_v^2)}. \quad (15)$$

For numerical studies, we use the following compressible Fung type approach regarding the isotropic part of the elastic potential ψ_{eq0}^{iso} which becomes a Neo-Hooke material for small deformations

$$\psi_{eq0}^{iso} = \frac{C_1}{\alpha} \left[e^{\alpha(I - \ln III - 3)} - 1 \right] + D_2 (\ln III)^2. \quad (16)$$

To simplify the estimation procedure for the material parameters, a similar Fung type approach is used at this stage for the transversely isotropic part of the elastic potential ψ_{eq0}^{aniso}

$$\psi_{eq0}^{aniso} = \frac{C_2}{\beta} \left[e^{\beta(I_4 - 1)^2} - 1 \right]. \quad (17)$$

The constants C_1 , α , D_2 , C_2 and β are hyperelastic material parameters to be identified from suitable experiments.

It can be easily shown that the special formulations (16) and (17) satisfy the requirement of a stress free undeformed configuration with a zero energy value as well as the requirement of polyconvexity. Furthermore, at zero or infinite values for the right Cauchy-Green strain tensor, the corresponding parts of the Helmholtz free energy density increase to infinite values as expected.

In order to implement the present viscoelastic material model into a commercial finite element (FE) code, we defined the special functions ψ_{ov}^{iso} and ψ_{ov}^{aniso} for the viscous potentials for simplicity

$$\psi_{ov}^{iso} = \frac{C_{1ov}}{\alpha_{ov}} \left[e^{\alpha_{ov} (I_{ov} - \ln III I_{ov} - 3)} - 1 \right] + D_{2ov} (\ln III I_{ov})^2, \quad (18)$$

$$\psi_{ov}^{aniso} = \frac{C_{2ov}}{\beta_{ov}} \left[e^{\beta_{ov} (I_{4ov} - 1)^2} - 1 \right]. \quad (19)$$

The material parameters C_{1ov} , α_{ov} , D_{2ov} , C_{2ov} and β_{ov} , were similar to the isotropic elastic potentials. Further details of the material model are provided in [7, 8].

3.3 Quasi-Unconfined Compression of an Osteochondral Graft

The above presented biphasic material model with intrinsic large strain transversely isotropic viscoelastic solid phase properties has been implemented into the FE code *MSC-Marc* using provided material interfaces within the context of poroelasticity.

Due to the unpredictable and numerically unstable boundary conditions (tangential contact with undefined friction state between the plug and the walls of the recipient hole), the numerical simulation of the real grafting process poses an exceptional challenge. Consequently, the present study focuses on the numerical simulation of the deformation state of osteochondral grafts obtained in the compression tests mentioned above.

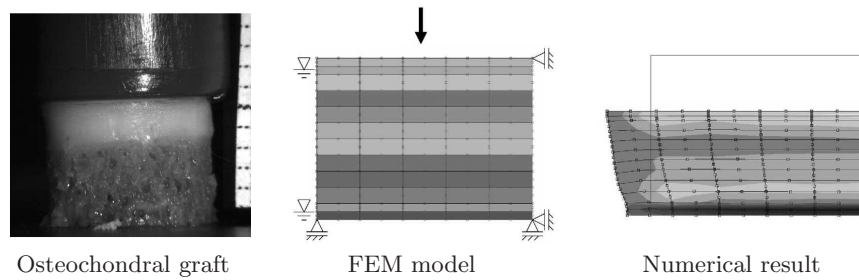


Fig. 4. Numerical simulation of the quasi-unconfined compression of osteochondral grafts using the soil option of the FE-code *MSC-Marc* with a user-defined material model for the effective stress at finite strains.

To numerically simulate the impact loading of clamped osteochondral grafts, we used an idealized model of a cylindrical cartilage plug under unconfined compression between impermeable plates (see Figure 4). The axisymmetric FE model was spatially discretized using 60 eight-noded Herrmann-type elements provided by MSC-Marc for solving mixed formulations. The load controlled impactation process is treated as a frictionless contact problem. Material parameters were estimated from in-house experimental results and data in the literature. In Figure 4 a typical pore pressure distribution is shown obtained during the adaptation phase of the numerical model.

4 Conclusions

Osteochondral grafting is a common method of treating focal degenerative or traumatic joint defects. However, impact loading occurring during re-implantation of the grafts may affect the viability of chondrocytes, and result in subsequent tissue degeneration. Both necrotic and apoptotic effects are reported. Knowledge of the mechanobiological environment during re-implantation of osteochondral grafts may be important to prevent cell death, and to sustain cartilage function.

A combined experimental-numerical approach to analyse the mechanics and the biology of the grafting process has been presented. The FE analysis of compression tests at impact loading is conducted with a complex biphasic material model for large deformations. Currently, systematic numerical simulations of the plug impactation are being performed to correlate the spatial distribution of mechanical variables with cell response (e. g. cell viability ratio). The aim of these studies is to detect the active mechanobiological principles controlling cell metabolism during and after the osteochondral graft insertion process and, consequently, to be able to perform numerical experiments in order to improve the surgical procedure.

5 Acknowledgment

This work was supported by AO Research Grant 02-W66.

References

1. de Boer, R.: *Theory of porous media: Highlights in Historical Development and Current State*. Springer-Verlag, Berlin, 2000.
2. Borazjani, B. H.; Chen, A. C.; Bae, W. C.; Patil, S.; Sah, R. L.; Firestein, G. S. & Bugbee, W. D.: Effect of impact on chondrocyte viability during insertion of human osteochondral grafts. *The Journal of Bone and Joint Surgery (American)* **88** (2006), 1934–1943.
3. Bowen, R. M.: Incompressible porous media models by use of the theory of mixtures. *International Journal of Engineering Science* **18** (1980), 1129–1148.

4. Ehlers, W.: Grundlegende Konzepte in der Theorie Poröser Medien. *Technische Mechanik* **16** (1996), 63–76.
5. Ehlers, W. & Markert, B.: A linear viscoelastic biphasic model for soft tissues based on the theory of porous media. *Journal of Biomechanical Engineering* **123** (2001), 418–424.
6. Ehlers, W.: Foundations of multiphase and porous materials. In: Ehlers, W. & Bluhm, J. (eds.): *Porous Media: Theory, Experiments and Numerical Applications*, Springer-Verlag, Berlin, 2002, pp. 4–86.
7. Görke, U.-J.; Günther, H. & Wimmer, M. A.: Multiscale FE-modeling of native and engineered articular cartilage tissue. In: *Proceedings of the IV European Congress on Computational Methods in Applied Sciences and Engineering. EC-COMAS 2004*, Jyväskylä, 2004, pp. 1–20 (Proceedings on CD).
8. Görke, U.-J.; Günther, H. & Wimmer, M. A.: A poroviscoelastic overlay model for finite element analyses of articular cartilage at large strains. In: Mota Soares, C. A. et al. (eds.): *Solids, Structures and Coupled Problems in Engineering. Proceedings of III European Conference on Computational Mechanics Lissabon*, Springer, Dordrecht, 2006, p. 199 (Book of Abstracts), pp. 1–20 (Proceedings on CD).
9. Huang, C.-Y.; Stankiewicz, A.; Ateshian, G. A. & Mow, V. C.: Anisotropy, inhomogeneity, and tension-compression nonlinearity of human glenohumeral cartilage in finite deformation. *Journal of Biomechanics* **38** (2005), 799–809.
10. Krefner, T.: *Experimentelle Studien zur kontrollierbaren Lastaufbringung an osteochondralen Implantaten als Knorpelersatz*. Report of the Institute of Mechanics and Thermodynamics, Chemnitz University of Technology, 2006.
11. Lion, A.: A physically based method to represent the thermo-mechanical behaviour of elastomers. *Acta Mechanica* **123** (1997), 1–25.
12. Maroudas, A.: Physico-chemical properties of articular cartilage. In: Freeman, M. A. R. (ed.): *Adult Articular Cartilage*, Pitman Medical, 1979, pp. 215–290.
13. Mow, V. C. & Ratcliffe, A.: Structure and function of articular cartilage and meniscus. In: Mow, V. C. & Hayes, W. C. (eds.): *Basic Orthopaedic Biomechanics*, Raven Press, 1997, pp. 113–178.
14. Müller, S.: *Numerische Simulation des Implantationsvorganges von Knorpelgewebe mittels der Methode der Finiten Elemente*. Diploma thesis, Report of the Institute of Mechanics and Thermodynamics, Chemnitz University of Technology, 2005.
15. Müller, S.; Wimmer, M. A.; Görke, U.-J. & Kreißig, R.: Mechanical response of articular cartilage during impaction loading in unconfined compression. In: Huber, G.; Schneider, E. & Morlock, M. (eds.): *Tagungsband zur DGfB-biomechanica V*, Hamburg, 2005, p. 125.
16. Olsen, S. & Oloyede, A.: A finite element analysis methodology for representing the articular cartilage functional structure. *Computer Methods in Biomechanics and Biomedical Engineering* **5**(6) (2002), 377–386.
17. Pande, G. N.; Owen, D. R. J. & Zienkiewicz, O. C.: Overlay models in time-dependent non-linear material analysis. *Computers & Structures* **7** (1977), 435–443.
18. Prevost, P.: Mechanics of continuous porous media. *International Journal of Engineering Science* **18** (1980), 787–800.
19. Reese, S. & Govindjee, S.: A theory of finite viscoelasticity and numerical aspects. *International Journal of Solids and Structures* **35** (1998), 3455–3482.

20. Wimmer, M. A.; Müller, S.; Pylawka, T.; Görke, U.-J.; Cole, B. J. & Williams, J. M.: Mechanical and cellular response of osteochondral tissue during impaction grafting. In: *Proceedings of the ASME 2005 Summer Bioengineering Conference*, Vail, Colorado (USA), 2005, pp. 1-2.

A Damage-based Model to Describe Aging in Cortical Bone

I. Ott, R. Kienzler & R. Schröder

Fachbereich Produktionstechnik 04, Universität Bremen,
Badgasteinerstraße 1, 28359 Bremen, Deutschland

Abstract. Previous studies have shown that the material behaviour of cortical bone changes due to aging from ductile to more brittle, accompanied by loss of fracture energy. Based on published data from one-dimensional mechanical testing for tension [7], first we describe the measured stress-strain curves characterised by their published value for Young's modulus, elastic, plastic and fracture energy, fracture stress and strain, by employing the nonlinear Ramberg-Osgood power law. The experiments have shown a relationship between the mechanical behaviour, age and microstructure, especially the porosity, mineralization and fraction of the secondary osteonal area. By analogy to common procedures in fracture and damage mechanics, we consider these 'individual values' as independent damage parameters. Afterwards we postulate by means of the statistical regression of these independent damage parameters the time dependent material behaviour. From measurable individual parameters only, we are able to predict the stress-strain curves of individuals for arbitrary times.

1 Aging of the Corticalis

The adult human skeleton consists of two kinds of bone tissue:

1. The spongiosa or cancellous bone, which is a spongy-like material with curved plates and rods. It is primarily found in the inner of the vertebrae and in the metaphysis of long bones near to the articulated joints.
2. The corticalis or compacta, which makes up 75% - 80% of the whole skeletal mass. The outer shell of all skeletal bones and the whole middle shaft of the long bones, diaphysis, are composed of corticalis. It is a compact, solid material which consists of lamellar layers. The lamellae themselves have three forms of appearance: the secondary osteons (Figure 1, (2) and (3)), interstitial lamellae (Figure 1, (4)) and the inner and outer circumferential.

The secondary osteons are cylindrical tubes, which are permanently re-built by the remodelling process. The remodelling is regulated by the mineral metabolism and the appearance of microcracks caused by ordinary impact. Osteoblasts cut a tunnel along the longitudinal axis of bone, eating away the damaged tissue. Afterwards, the tunnel is filled up by circular rings of lamellae surrounding the vascular channel (Figure 1, (3)), both of them together forming the so called haversian system or osteon (Figure 1, (2)). The

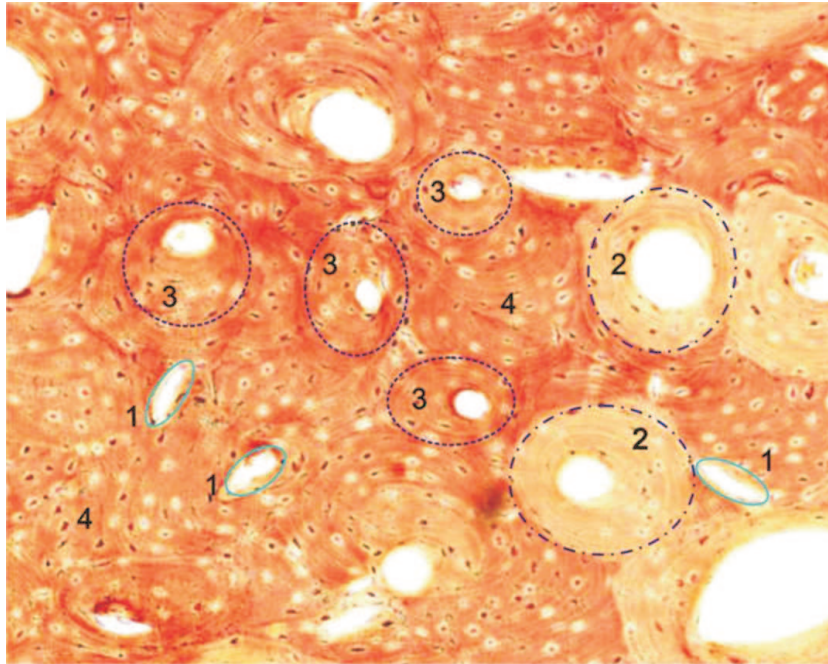


Fig. 1. Corticalis with pores (1), low mineralised (2) and fully mineralised (3) osteons with haversian channels, interstitial lamellae (4).

angular fragments filling the gaps between are known as interstitial lamellae. These fragments have formerly been concentric or circumferential lamellae. If an individual gets older, the corticalis in general becomes more porous (cf. Figure 1, (1)), because erosion cavities arise and the haversian channels grow in diameter. The osteons occurring in old-aged individuals usually have a lower mineral content than in younger ones. The amount of haversian bone increases with age. The geometry of the bone changes as well, e. g., the wall of the diaphysis becomes thinner with age. Not only are the histological and microstructural parameters age-dependent, but the mechanical behaviour as well. The ultimate specific fracture energy decreases with age significantly. So do the strength and the ultimate strain. These developments are well known, first documented by [6], [1], and [4]. Due to the progress in microstructural analyses in bone, two actual studies [9] and [7] publish experimental data, concurrently measuring mechanical and microstructural parameters from individuals of different age. The authors spared no effort to get this data, but there was no obvious correlation between the individual values for age, for the mechanical behaviour, or for the histological and microstructural parameters. So up to now, there is no material law postulated, which connects this statistical trends. We decided to work with the experimental data from McCalden [7] to derive a simple model for the time depend nonlinear behaviour.

2 The Ramberg-Osgood Power Law

At autopsies, McCalden et al. [7] harvested the femora of forty-six individuals, aged 20 to 102 years. They have taken five equal specimens from each individual and tested them in tension (strain controlled) to failure. Afterwards, they determined the porosity of the cross-sectional area and the corrected osteonal area, based on the cross-sectional area corrected by porosity using an image-analysis system. They have used a colorimetric method to determine the milligrams of Ca^{2+} per gram of dry weight of bone. All these values have been published graphically in diagrams versus age. To describe the stress-strain curves, they provide the Young's modulus for the linear part, the ultimate strain and the ultimate stress, and they defined the so-called 'elastic' energy as the triangle area and a 'plastic' energy as the trapezoidal area, shown in Figure 2. The fracture energy is the area underneath the stress-strain curve. Based on this data, we have calculated the dashed line and optimized it to

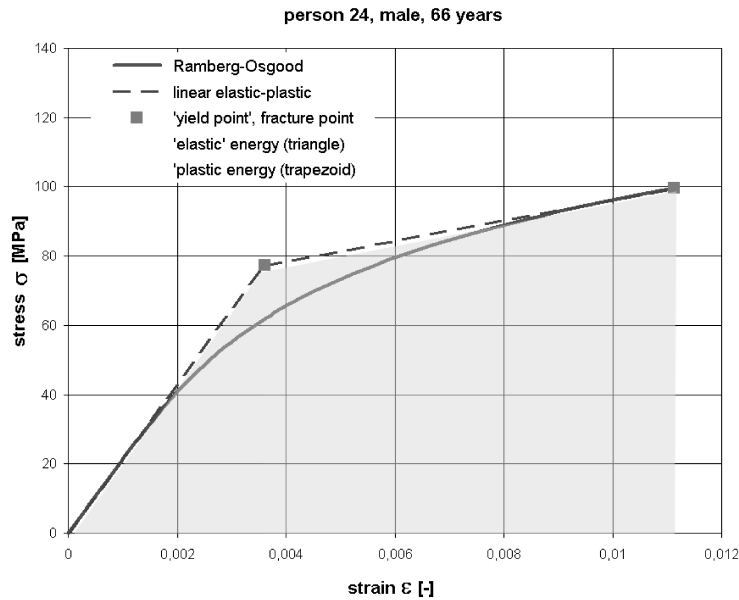


Fig. 2. The published data of person 24, a 66 years old male, and the fitted stress-strain curve as example.

get the two material parameters n and k in the Ramberg-Osgood power law yielding

$$\epsilon = \frac{\sigma}{E} + k \left(\frac{\sigma}{E} \right)^n . \quad (1)$$

The parameters have to fulfil the conditions that the stress-strain curve is tangent to the dash line in the fracture point and the integral satisfies best the measured value of the fracture energy

$$W_u = \int_0^{\varepsilon_u} \sigma d\varepsilon. \quad (2)$$

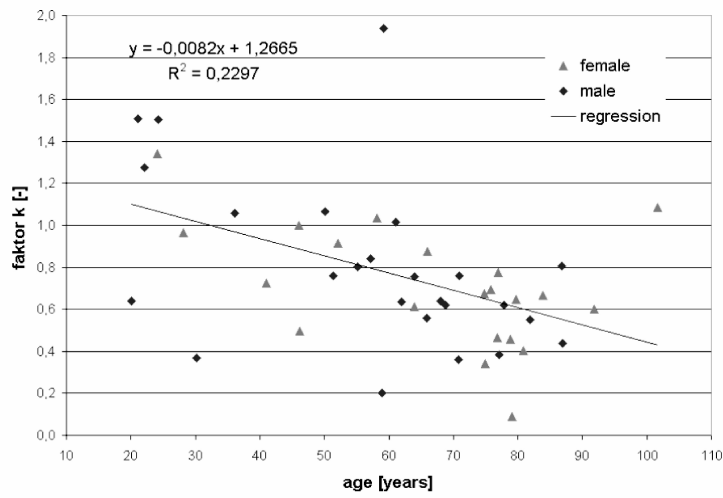


Fig. 3. Individual material parameter factor k .

We restrict the solution for n to 50 and so we get solutions for 45 of the 46 searched curves. Figure 3 and Figure 4 show the individual material parameters n and k of the Ramberg-Osgood power law versus age. Unfortunately, we cannot find any coherence between these material parameters and the histological and microstructural measured values. Neither with multilinear regression nor with covariance analysis, any statistical correlation could be found. The linear regression with age has not proved satisfactory. Nevertheless, the Ramberg-Osgood power law seemed to be successful to describe the mechanical behaviour with only a few parameters. This minimizes the database if mechanical testing has to be documented. Figure 5 shows stress-strain curves each for one decade being constructed by the mean target value of the individuals of each decade.

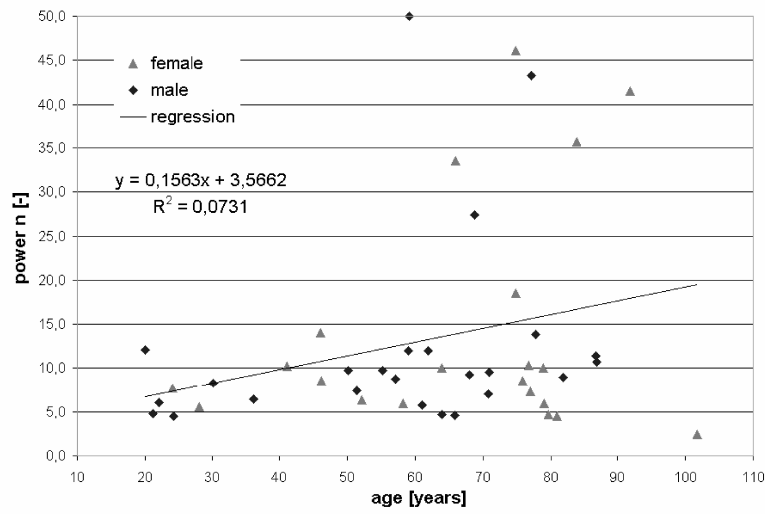


Fig. 4. Individual material parameter exponent n .

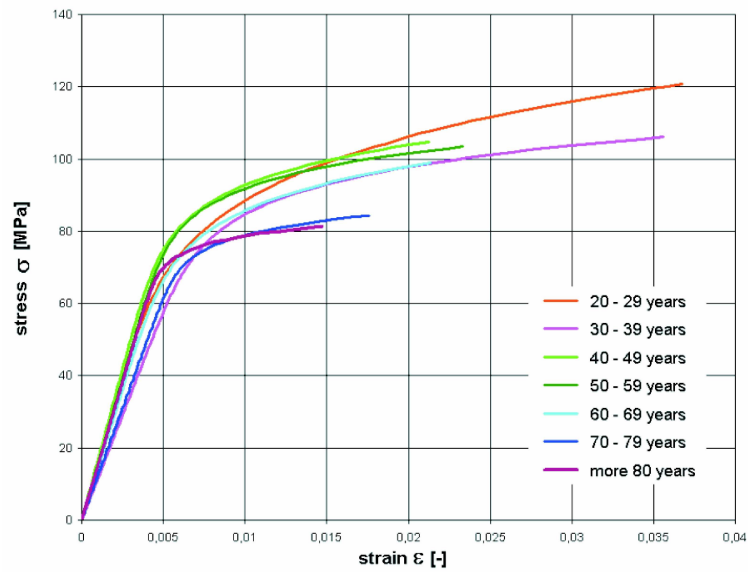


Fig. 5. Stress-strain curves of the average target value for each decade.

3 Hookian and Damaged Spring in Parallel

Let us now divide the corticalis in its two lamellae forms: the osteons (*ost*) and the interstitial lamellae (*ins*). The strain in the corticalis of both constituents

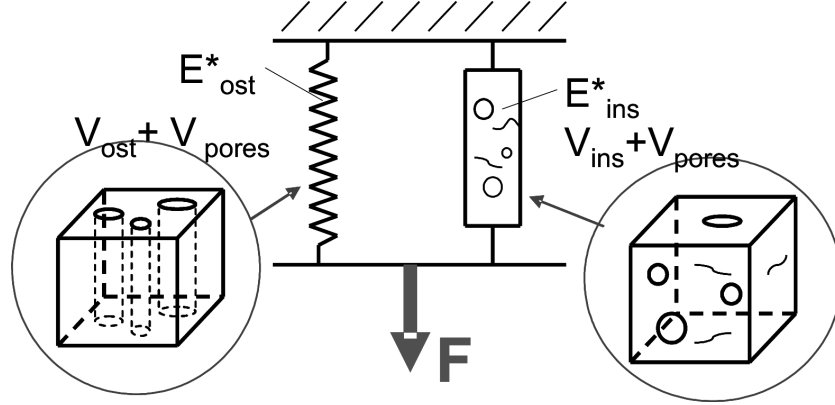


Fig. 6. Hookian and damaged spring in parallel, representing the osteons and the interstitial lamellae.

is the same, but, if we assume different Young's moduli for the two different lamellar forms, the stresses are different. Therefore, the simplest model is that of springs in parallel, see Figure 6. The effective Young's modulus E^* for such a system, taking into account the area fraction osc for the osteons, is

$$E^* = osc E_{ost}^* + (1 - osc) E_{ins}^* \quad (3)$$

with E_{ost}^* : effective Young's modulus for the osteons,
 E_{ins}^* : effective Young's modulus for the interstitial lamellae,

hence the stress-strain curve for the macrostructure of the corticalis is

$$\sigma = osc \sigma_{ost} + (1 - osc) \sigma_{ins} . \quad (4)$$

For the published pore fraction has no subdivision into the haversian channel and the pores in the interstitial lamella we assign the pore fraction equally to both springs. The haversian channels are orientated longitudinally. Thus, the microstructure of the osteon can be modelled as unidirectional hollow cylinders. We consider a representative volume RVE on the microstructure level to describe macroscopic properties of the material in terms of a spatially effective elastic tensor. The prerequisite for this is, that the RVE contains a sufficient number of defects with a statistically homogeneous distribution. If the defects do not interact with each other, homogenization leads to the effective Young's Modulus (plane strain) [5] for the macrostructure

$$E_{ost}^* = \frac{1 - p}{1 + p(2 - 3\nu^2)} E_{ost} \quad (5)$$

with

p : Volume or area fraction of the pores ,

ν : Poisson's ratio $\nu = 0, 4$ and

E_{ost} : Young's modulus for the microstructure (undamaged material) .

The behaviour of the osteons until fracture is linear elastic, because they tend to be less mineralised than the interstitial lamellae, in which they are situated. Because the tensile strength increases with mineralization, we expect crack growth to occur only in the comparatively older interstitial tissue. The less mineralised bone in relatively young haversian systems has a lower Young's modulus than the older surrounding bone [8]. The stress-strain curve for the hookian spring, representing the material behaviour of the osteon, can thus be described as

$$\sigma_{ost} = \varepsilon \frac{1-p}{1+p(2-3\nu^2)} E_{ost} . \quad (6)$$

We model the microstructure and behaviour of the interstitial lamellae up to fracture using the damage model for brittle fracture under uniaxial tension. Up to a well-defined loading level, which may be seen as a kind of usual impact or overall load configuration, there is no crack growth. The bone growth is accustomed to this strain. Microcracking starts, if the bone is strained over the yieldpoint. Acoustic emission [10] shows that in the preyield region the specimens are almost silent, but as the curve bends over, there is a burst of noise, which quiets down somewhat in the postyield region, before appearing again as the final crack destroys the specimen. The well-known model for this behaviour (cf., e. g., [5]), is based on the complementary energy of the undamaged material and energy changes caused by the presence of microcracks, giving rise to the energy release rate G . For a plane region, containing a single mode-I crack with the initial length $2a_0$ and the actual crack length $2a$, the stress-strain curve can be described assuming that beyond a certain loading σ_0 or strain ε_0 , the crack grows according to the fracture criterion G :

$$\varepsilon(\sigma_{ins}, a) = \frac{\sigma_{ins}}{E_{ins}} \left(1 + \frac{2\pi}{\Delta a} a^2 \right) \quad (7)$$

with

$$a = a_0 \quad \text{for} \quad \sigma_{ins,0} \sqrt{\pi a_0} = K_0 ,$$

$$\Delta a > 0 \quad \text{for} \quad \sigma_{ins} \sqrt{\pi (a_0 + \Delta a)} = K_R(\Delta a) ,$$

K_0 initial stress-intensity factor ,
 K_R current stress-intensity factor .

As usual, we represent the crack-resistance curve $K_R(\Delta a)$ by an evolution law with the internal variable η :

$$K_R(\Delta a) = K_\infty \left[1 - \left(1 - \frac{K_0}{K_\infty} \right) e^{-\eta \frac{\Delta a}{a_0}} \right]. \quad (8)$$

Knowing well that the energy release rate for penny-shaped cracks differs slightly from the one for a single mode-I crack, we accept the error for the sake of simplicity of the model. Due to the working hypothesis that the initial crack length is equal to the mean void radius r_0 , it becomes possible to associate the measured microstructural geometry to the variable a_0 in the damage law. Based on [3], the pores are assumed to be spherical voids, and are evenly distributed and homogeneous. The measured area fraction p by a random cut through a cubic cell with one embedded spherical void leads to the expect ratio n by

$$n = \sqrt[3]{\frac{6p}{\pi}} \quad (9)$$

with

$$\begin{aligned} r_0 &= n b && \text{radius of the void,} \\ V_{RVE} &= 8 b^3 && \text{volume of the cubic } RVE. \end{aligned}$$

Using the abbreviation $\gamma = K_\infty K_0$ where K_∞ is the plateau value and

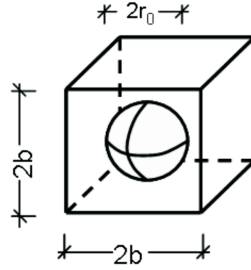


Fig. 7. Geometry of the *RVE* for brittle facture in the interstitial lamellae.

K_0 is the initial value for the crack resistance curve K_R , and including the geometry variables n for the initial crack length and m for the crack growth related to the cubic *RVE* leads to:

$$\frac{\varepsilon}{\varepsilon_0} = \frac{\sigma_{ins}}{\sigma_{ins0}} \frac{1 + \frac{\pi}{2}(n+m)^2}{1 + \frac{\pi}{2}n^2}, \quad (10)$$

$$\frac{\sigma_{ins}}{\sigma_{ins0}} = \frac{\sqrt{n}}{\sqrt{n+m}} \left[\gamma - (\gamma - 1) e^{-\eta \frac{m}{n}} \right]. \quad (11)$$

This is a stress-strain curve for the interstitial-lamellae-nonlinear spring with damage up to brittle failure parameterised by m . Unknown are the yield point with the initial stress σ_0 and the initial strain ε_0 , the ratio γ of the crack resistance, and the evolution parameter η . Hence the stress-strain curve for the damaged corticalis is

$$\sigma = \varepsilon(m) \left[E_{ost} osc \frac{1-p}{1+p(2-3\nu^2)} + E_{ins} \frac{1-osc}{1+\frac{\pi}{2}(n+m)^2} \right], \quad (12)$$

It is linear in the interval $0 < \varepsilon < \varepsilon_0$ for $m = 0$
and nonlinear in the interval $\varepsilon_0 < \varepsilon < \varepsilon_u$ for $0 < m < m_u$.

E_{ins} is the Young's modulus of the undamaged interstitial material. To find the unknowns, the measurement of the mechanical behaviour of the specimens have to keep the following conditions:

- Measured Young's modulus E^* in the linear interval

$$E^* = E_{ost} osc \frac{1-p}{1+p(2-3\nu^2)} + E_{ins} \frac{1-osc}{1+\frac{\pi}{2}n^2}.$$

- Measured fracture point with the values for ultimate stress σ_u and ultimate strain ε_u

$$\sigma_u = \varepsilon_u(m_u) \left[E_{ost} osc \frac{1-p}{1+p(2-3\nu^2)} + E_{ins} \frac{1-osc}{1+\frac{\pi}{2}(n+m_u)^2} \right].$$

- The derivative of σ_{ins} with respect to the ultimate strain ε_u has to be zero, because the cracks become unstable at the fracture point

$$\frac{d\sigma_{ins}}{d\varepsilon_u} = 0 \quad \text{for} \quad m = m_u, \quad \varepsilon(m_u) = \varepsilon_u.$$

- The derivative of σ with respect to the ultimate strain ε_u has to be $osc \cdot E_{ost}^*$

$$\frac{d\sigma}{d\varepsilon} = E_{ost} osc \frac{1-p}{1+p(2-3\nu^2)} \quad \text{for} \quad m = m_u.$$

- The derivative of σ_{ins} with respect to the strain ε has to be positive because the stress has to be monotonically increasing

$$\frac{d\sigma_{ins}}{d\varepsilon} > 0 \quad \text{for} \quad 0 \leq m \leq m_u.$$

- The integration of the stress-strain curve with the integration limits 0 and ε_u has to be equal to the measured fracture energy

$$\begin{aligned}
 W_u &= \int_0^{\varepsilon_u} \sigma \, d\varepsilon = \\
 &= \frac{1}{2} \varepsilon_u^2 E_{ost} osc \frac{1-p}{1+p(2-3\nu^2)} + \frac{1}{2} \varepsilon_0^2 E_{ins} \frac{1-osc}{1+\frac{\pi}{2}n^2} \\
 &\quad + (1-osc) \int_0^{m_u} \sigma_{ins} \frac{d\varepsilon}{dm} \, dm.
 \end{aligned}$$

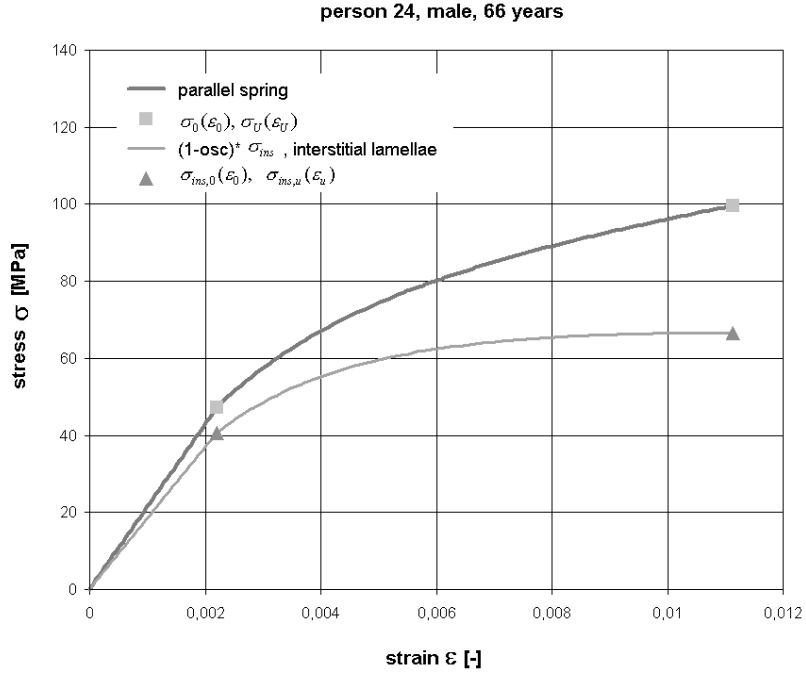


Fig. 8. Nonlinear stress-strain curves of the springs in parallel and the nonlinear spring for the interstitial lamellae, scaled for its area fraction.

This system of equations has an explicit solution. It can be solved numerically by a self-developed software. Figure 8 shows the stress-strain curve for the published data of person 24. Within this model, it is possible to calculate a quasi-bilinear behaviour (person 19) as well as a quasi-brittle behaviour (person 40), cf. Figure 9. This model seems to be successful to describe the

material behaviour of the corticalis in tension. The microstructure of the bone is used to calculate the material behaviour up to fracture.

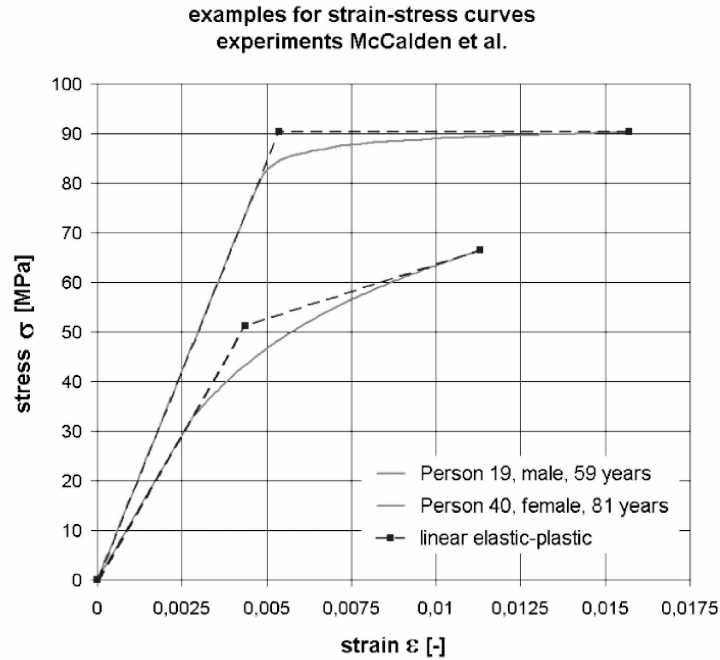


Fig. 9. Examples for quasi-brittle fracture (person 40) and bi-linear behaviour (person 19).

4 Time-Dependence of the Material Parameters of the Spring-in-Parallel Model

The crack resistance ratio γ (Figure 10) and the evolution parameter η (Figure 11) show linear time dependence with a smaller coefficient of determination R^2 than the material parameter of the Ramberg-Osgood power law. Fortunately they are not needed for a prognosis of an individual material behaviour in the future, because they can be generated. We can find a strong time-dependence between the ratio of the internal damage variable vs. age, see Figure 12. The hypothesis, that the energy up to the yield strain ϵ_0 is a kind of usual impact load is confirmed by the time-dependent regression curve of the calculated strain ϵ_0 , see Figure 13. The polynomial has a plateau for the persons between 30 and 70 years. For younger persons, the value is

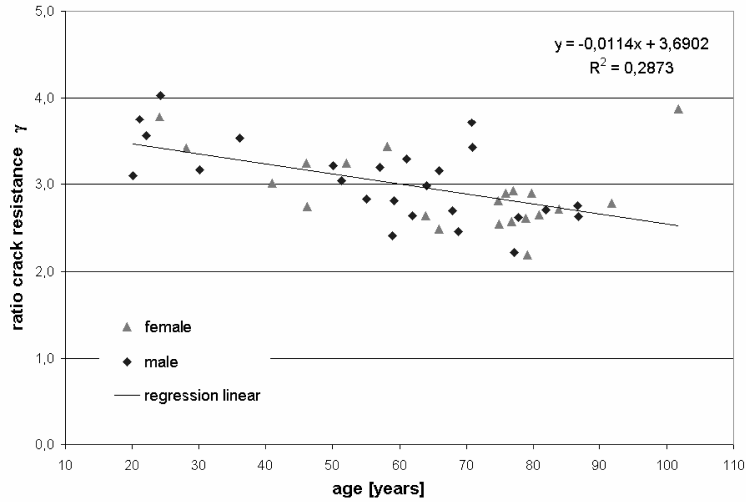


Fig. 10. Ratio crack resistance γ vs. age.

higher, whereas in the last decades, from 70 to 100 years, the value decreases rapidly. This is a load behaviour as expected. In contrast to a lot of studies, which propose a linear correlation or power law regressions, McCalden [7] did not find any correlation between the measured Young's Modulus E^* for the linear interval and the measured mineral content Ca^{2+} . The result is surprising, because it is generally accepted, that the Young's modulus depends on the mineral fraction, cf., e. g., [2]. This might be due to the fact that the microstructure varies tremendously in the specimens. We find a time-depended correlation, which is not so strong but relevant between the sum of the calculated, undamaged Young's moduli per mineral fraction versus age, see Figure 14.

5 Prediction of the Prospective Individual Material Behaviour

With the results of the experiments from McCalden [7] from dead persons and with our damage-based model, we are now able to determinate the actual material behaviour for the first time for living persons without a destructing testing. We calculate the target mechanical values necessary for our calculation program (fracture energy W_u , ultimate strain ε_u , ultimate stress σ_u) by linear regressions of the histological and biological values sex (set 1 for female and 0 for male), age in years, pores area fraction $p[-]$, mineral content of the dry bone $Ca^{2+}[-]$, and the corrected osteon area fraction $osc[-]$, which

can be gained by biopsy.

$$\begin{aligned}
 W_u &= -0,419916 + 0,28993 \text{ sex} - 0,0304638 \text{ age} - 2,219989 p \\
 &\quad + 22,0020239 Ca^{++} - 2,414871 \text{ osc}, \\
 R^2 &= 0,734, \\
 \varepsilon_u &= -0,0358782 + 0,00188142 \text{ sex} - 0,000281694 \text{ age} \\
 &\quad - 0,000891402 p + 0,345772 Ca^{++} - 0,0202157 \text{ osc}, \\
 R^2 &= 0.671, \\
 \sigma_u &= 134,4726 + 4,857621 \text{ sex} - 0,219051 \text{ age} - 170,647433 p \\
 &\quad + 19,889533 Ca^{++} - 23,525239 \text{ osc}, \\
 R^2 &= 0,751.
 \end{aligned}$$

In the reconstruction of the experiments, we have used the measured effec-

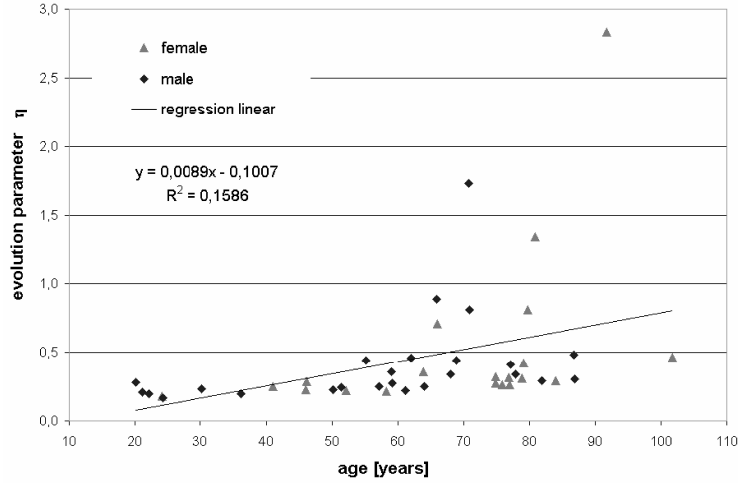


Fig. 11. Evolution parameter η vs. age.

tive Young’s modulus E^* for the parallel spring, calculated from the measured Young’s modulus. Because we did not find any correlation to the histological values, we took instead the regression shown in Figure 14. We calculate the individual loading capacity of a whole bone, using the individual stress-strain curve, and the individual geometry, which is determined through imaging techniques for bone. We also find the usual individual impact for living individuals, determined by the yield strain ε_0 , which was until now impossible to define. Provided that the individual evolution of time-dependent histological parameters is equal to the statistical ones, we can take the derivative of the

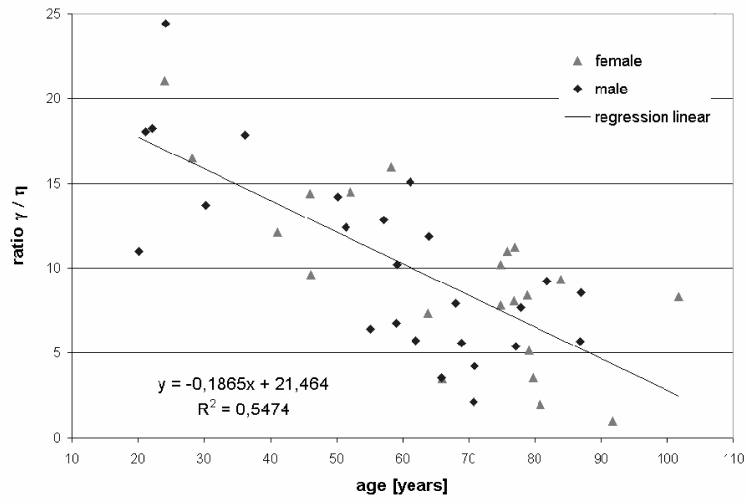


Fig. 12. Ratio γ/η vs. age.

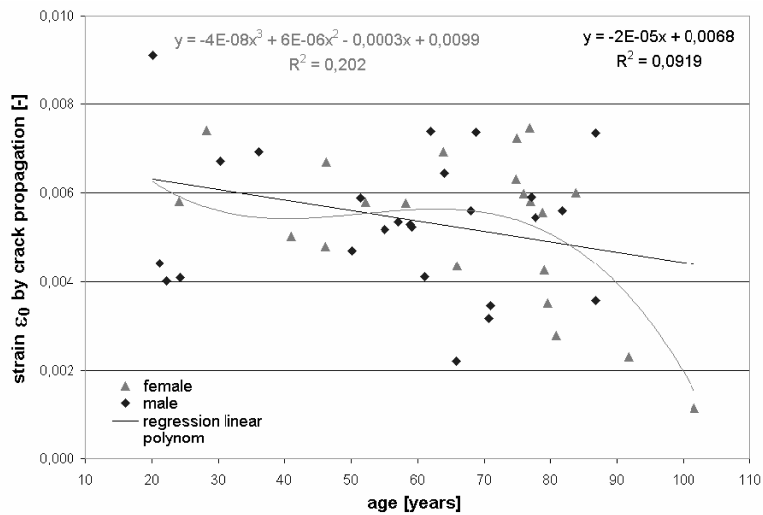


Fig. 13. Yield strain ϵ_0 defined by the beginning of crack propagation vs. age.

regressions to calculate future behaviour. McCalden [7] found

$$\begin{aligned}
 p(t) &= -1,8347 + 22,046 p, & R^2 &= 0,533, \\
 osc(t) &= 34,799 + 19,194 osc, & R^2 &= 0,203.
 \end{aligned}$$

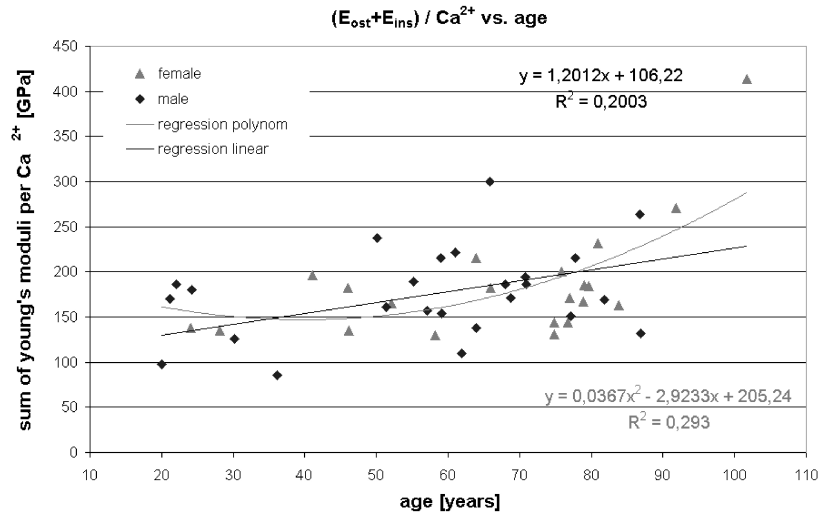


Fig. 14. Ratio of sum of the calculated undamaged Young's moduli per mineral content versus age.

We keep the mineral content constant, because there was no relationship to time. With the time-dependency of the ratio of our internal variables η and γ , we may get an anticipation of the future mechanical behaviour of the corticalis.

Acknowledgement: Figure 1 with friendly permission from Dr. F. Schöni-Affolter, Universität Fribourg / Schweiz, Departement Medizin, Abteilung Histologie. Special thanks to Dr. rer. nat. Olaf Mosbach-Schulz from the Institut für Statistik, Universität Bremen. His profound knowledge was a great help for the statistical interpretation.

References

1. Burstein, A. H.; Reilly, D. T. & Martens, M.: Aging of bone tissue. *Journal Of Bone And Joint Surgery*, **58(1)** (1976), 82-86.
2. Currey, J. D.: *Bones, structure and mechanics*, Princeton University Press, Princeton, 2002.
3. Dong, XN. & Guo XE.: The dependence of transversely isotropic elasticity of human femoral cortical bone on porosity. *Journal of Biomechanics* **37(8)** (2004), 1281-1288.
4. Evans, F. G.: *Mechanical properties of bone*. Thomas, Springfield, III, 1973.
5. Gross, D. & Seelig, T.: *Fracture mechanics, with an introduction to micromechanics*, Springer, Heidelberg, 2006.
6. Lindahl, O. & Lindgren, A. G.: Cortical bone in man. *Acta Orthopaedica Scandinavica* **38(2)** (1967), 141-147.

7. McCalden, R. W.; McGeough, J. A.; Barker, M. B. & Court-Brown, C. M.: Age-related changes in the tensile properties of cortical bone. The relative importance of changes in porosity, mineralization, and microstructure. *Journal Of Bone And Joint Surgery*, **75(8)** (1993), 1193-1205.
8. Rho, Y. J.; Zioupos, P.; Currey J. D. & Pharr, G. M.: Variations in the individual thick lamellar properties within osteons by nanoindentation. *Bone* **25** (1999), 111-119.
9. Zioupos, P. & Currey, J. D.: Changes in the stiffness, strength, and toughness of human cortical bone with age. *Bone*, **22(1)** (1998), 57-66.
10. Zioupos, P. & Currey, J. D.: The extent of microcracking and the morphology of microcracks in damaged bone. *Journal of Materials Science* **29** (1994), 978-976.

Numerical Investigations on the Biomechanical Compatibility of Hip-Joint Endoprostheses

U. Nackenhorst & A. Lutz

Institute of Mechanics and Computational Mechanics, University of Hanover
Appelstraße 9a, 30167 Hannover, Germany

Abstract. A computational approach for studies on the biomechanical compatibility of artificial hip-joint implants based on detailed three-dimensional finite element models is presented. The stress adaptive bone remodelling is described in a thermodynamic consistent constitutive framework. Special attention is laid on the description of the loading conditions due to joint forces and muscle loads. By an inverse simulation technique a statically equivalent load set is computed based on measured bone mass density distributions. Results for two alternative treatments are compared, one with a classical stem-endoprosthesis and one with a minimal invasive resurfacing device. By these results it is demonstrated that computational mechanics can assist in the development of new prosthesis designs regarding their biomechanical compatibility.

1 Introduction

Artificial joint replacement is one standard surgery for joint diseases. With more than 100.000 implantations per year hip-joint endoprosthetics is the most frequent treatment in Germany. A typical complication is aseptic loosening of the implantbone integration with the indication for revision. Stress shielding caused by unphysiological load transfer due to the stiff implant is discussed as one major source for these failure scenario. Besides the requirement on the biocompatibility of the implanted materials, investigations on optimised prosthesis designs with better biomechanical compatibility are performed. Computational mechanics can assist to accelerate these developments.

Since Wolff [1] stated his law of bonetransformation in the late 19th century the relation between bone formation an mechanical demand is well accepted. Pioneering work in this field has also been done by Pauwels [2]. Starting with the late 1980s going along with increased computer performance and related development of computational mechanics first theories on stress adaptive bone remodelling have been developed [3–7], which have been refined for more and more detailed analysis in the following years, e. g., [8–12]. A state of the art modelling approach will be presented in Section 2. Besides the description of the mechanically driven change of bone mass density within a thermodynamical consistent constitutive framework, special emphasis is laid onto the proper formulation of the loading conditions due to joint loads and muscle forces.

At this stage these modelling approaches are far beyond a quantitative prediction of stress driven bone reaction, because the mechanotransduction process, i. e. the mechanical stimulation of bone cells and the signaling mechanism are not well explained till now. However, these models allow a qualitative decision between more or less biomechanical compatible endoprosthesis designs. Those studies will be presented in Section 3, where the computational results obtained for a standard hip-joint prosthesis are compared to those from the analysis of a minimal invasive resurfacing treatment. The reliability of the conclusions will be underlined by clinical studies.

2 Modeling Approach

The finite element method is an established and powerful numerical tool for stress analysis, which enables investigations of the mechanical behaviour for rather complicated 3-dimensional structures. For the simulation of stress adaptive bone remodelling a special constitutive description is needed, which describes the evolution of internal bone structure caused from changed loading conditions. For these macroscopic analysis a continuum approach is assumed, where the local bone structure is described by an averaged bone mass density. A couple of theories have been presented on this target, starting with purely phenomenologically motivated approaches [4–7] over more detailed anisotropic models [9, 10] to formulations which are consistent in a theoretical framework of constitutive modelling [10–12]. However, it seems to be nearly impossible to validate these models because of ethic reasons. The constitutive model used for our investigations is sketched below.

We start with the statement of a free energy function as

$$\Psi = \tilde{\Psi}(\boldsymbol{\varepsilon}, \varrho), \quad (1)$$

which depends on the elastic strain $\boldsymbol{\varepsilon}$ and the bone mass density ϱ , where ϱ is interpreted as internal variable. With these assumption from the entropy balance for an isothermal and quasi-static process the following form of the Clausius Duhem inequation is derived,

$$\left(\boldsymbol{\sigma} - \varrho \frac{\partial \Psi}{\partial \boldsymbol{\varepsilon}} \right) \cdot \dot{\boldsymbol{\varepsilon}} - \left(\varrho \frac{\partial \Psi}{\partial \varrho} + \Psi \right) \dot{\varrho} \geq 0. \quad (2)$$

From classical arguments in thermo continuum mechanics it is concluded that the term in the first bracket describes hyper-elasticity, the stress state can be derived from a free energy potential with respect to conjugate strain measures. The second term describes the biological aspects. The term in the brackets vanishes only, when

- the derivative of the free energy density with respect to the mass density is less than zero
- the free energy density is a linear function in ϱ

The first conclusion describes the process direction in an obvious kind, i. e. if locally bone mass is added the strain energy is reduced and visa verse. The second point gives important hints on the formulation of the constitutive coupling, i. e., the relationship between Young's modulus and bone mass density. Regarding this relation the empirical equation investigated by Carter and Hayes [13]

$$E(\varrho) = 3790 \varrho^3 \quad (3)$$

is cited quite often. Despite some problems in physical consistency of this representation (ϱ is a dimensional property) from the constitutive restrictions derived from the entropy inequality we conclude, that under the assumption of linear elastic mechanical behaviour the exponent has to be two as shown below.

For the first order approach of linear elastic material behaviour the strain energy function can be expressed as

$$\Psi = \frac{1}{2\varrho} \boldsymbol{\varepsilon}^T \frac{E}{E_0} \mathbb{C}_0 \boldsymbol{\varepsilon}, \quad (4)$$

where \mathbb{C}_0 represents the linear elastic constitutive matrix for an arbitrarily chosen reference material, e. g. cortical bone, characterised by E_0 . Now, from the more general representation of (3) of form

$$E = E_0 \left(\frac{\varrho}{\varrho_0} \right)^n, \quad (5)$$

it is concluded from the second fundamental statement that the exponent is $n = 2$. Besides, this conclusion is in agreement with a statistical analysis performed by Rice et al. [14], who derived on a broad data basis of experimental results a clear dominance of the quadratic term. Thus, the free energy density is rewritten as

$$\Psi = \frac{1}{2\varrho_0} \boldsymbol{\varepsilon}^T \frac{\varrho}{\varrho_0} \mathbb{C}_0 \boldsymbol{\varepsilon}, \quad (6)$$

by which the linearity in ϱ is shown.

A second issue is the development of evolution equations for the internal variable, i. e., bone mass density, within an established computable framework of inelasticity, cf. [15]. In analogy to a damage surface a growth function

$$f = \Psi - \Psi_{\text{bio}} = 0 \quad (7)$$

is defined, where Ψ_{bio} represents a biological target value. By this simple formulation it is stated, that the bone tries to find a mass distribution such that at each point the physiological strain energy density is apparent. Now from classical arguments in theory of materials and the assumption that a biological dissipation functional

$$D^{\text{bio}} = \varrho \frac{\partial \Psi}{\partial \varrho} \dot{\varrho} \quad (8)$$

takes extreme values, an evolution rule for the local bone mass density is derived

$$\dot{\rho} = \lambda \frac{\partial f}{\partial \rho}, \quad (9)$$

which is solved implicitly with return mapping like schemes.

A well known numerical instability in this context is checkerboarding using low order spatial finite element representations, see, e. g., [8]. This can be avoided by a smoothing step, where the mechanical stimulus, i. e., strain energy density distribution in this simple approach, is projected onto the nodal points using a superconvergent recovery technique [16].

An additional important issue on the simulation of bone remodelling phenomena is the description of the loading conditions, a topic which has not been discussed intensively in literature so far. A couple of results measured with instrumented hip-joint implants [17] and additionally simulations to compute related muscle forces for well defined motions have been reported, see, e. g., [18]. However, these loading conditions reflect short time reactions, while bone remodelling is a long term process. From computational point of view it is hopeless to simulate bone remodelling on basis of those data. Therefore, the concept of statically equivalent load sets will be suggested. The general idea is to compute a statically equivalent load set based on measured bone mass density distributions by an inverse simulation technique. First attempts on this strategy have been reported in [19], the application on detailed 3-dimensional finite element models of a femoral bone have been outlined in [20].

Results computed by use of a genetic optimisation strategy are depicted in Figure 1, where the resultant statically equivalent joint load and muscle forces are collected. From these studies we concluded, that at least 6 muscle groups have to be taken into account for a reliable simulation of the bone remodelling behaviour due to hip-joint replacement with standard stem-endoprosthesis to be discussed in the next Section.

For the evaluation of local effects the forces computed by this first step have to be distributed for a more physiological representation of the modeling approach. For this purpose locally a minimisation problem

$$\min_{F_i} \left(\sum_{i=1}^{n_{nodes}} |F_i| \mathbf{r}_i - \mathbf{F}_j \right)^2 \quad (10)$$

is solved, where F_i are the equivalent finite element nodal forces, \mathbf{r}_i denote the associated directions and \mathbf{F}_j is the statically equivalent force computed from the prior step. The computed nodal force-distribution is shown in Figure 2. With this load set the mass density distribution shown in Figure 2 has been computed. This result is in good agreement with CT data which underlines the proposed approach.

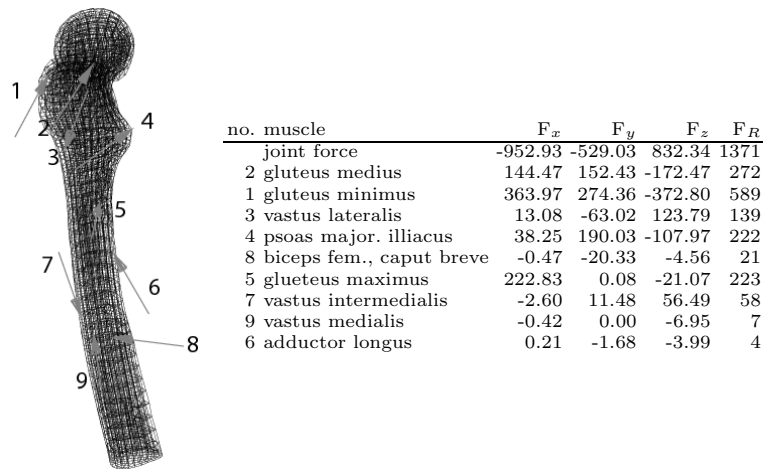


Fig. 1. Primary muscle forces after [20].

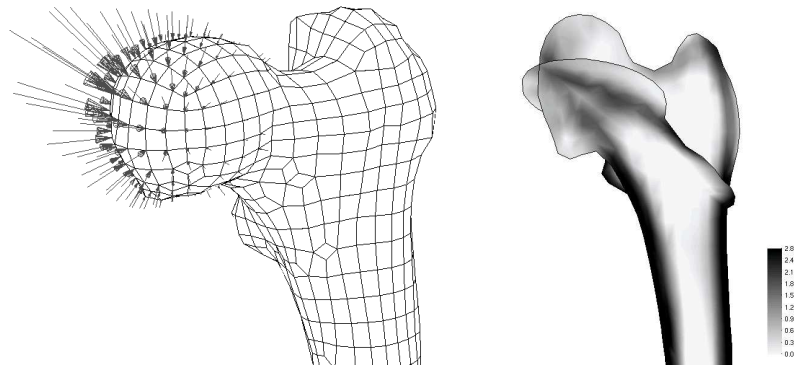


Fig. 2. Distributed joint force and mass density distribution in equilibrium state.

3 A Comparison of Two Hip-Joint Endoprosthesis

The first system analysed is the Zweymüller prosthesis which has been introduced in 1979 and seems to be the most frequently implanted non-cemented stem-prosthesis in Europe. The finite element model used for these investigations is shown in Figure 3. The computed results are depicted in Figure 6, where the change of bone mass density due to the changed mechanical environmental conditions is illustrated for a frontal plane cut. A loss of cortical bone mass density (atrophy) has been computed along the stem, which is in good agreement with clinical observations, see, e. g., [21]. This loss of bone stock might cause problems for revisions and therefore, this implant is rated

as low biomechanical compatible.

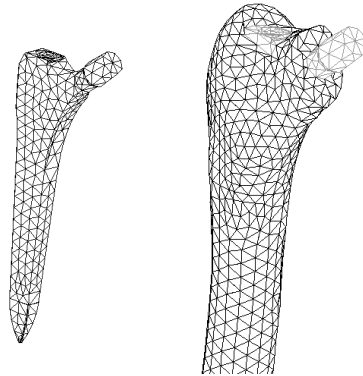


Fig. 3. FE-Model of Zweymüller-prosthesis and femur.

Especially for younger patients attempts on minimal invasive treatment are under investigation to ensure a rather good bone mass stock in the femoral bone for probable revisions. An design for rather low resections is the hip resurfacing technique. In Figure 4 the geometry of such a cap-prosthesis recovered from stereolithography (STL) data, the subsequently constructed CAD model and the generated FE model of the femoral bone with prosthesis are depicted.

The change of bone mass density distribution is illustrated in Figure 5. The pictures indicate stress shielding immediately under the cap while the femoral neck and the distal cortical structures are almost unaffected. Especially, the cortical structure and the spongy topology in the area of the greater trochanter are not influenced by the prosthesis. Therefore, this device provides a good bone stock when retreatment becomes necessary.

4 Conclusions

A modelling approach for numerical studies on boneremodelling caused from artificial hip-joint replacement has been presented in this contribution. The biological reaction of bones due to changes in mechanical demand has been described by a simple phenomenological model within a thermodynamically consistent framework on theory of materials by which a proper computational framework is defined. Special care has been taken on the description of the loading conditions due to joint loads and muscle forces. Statically equivalent loads have been computed by an inverse simulation approach based on measured bone mass density distributions. The joint loads have been distributed carefully to obtain realistic bone structures in a biomechanical equilibrium stage.

The biomechanical compatibility of two different hip-prosthesis has been analysed using detailed three-dimensional finite element models. While traditional

stem-endoprostheses lead to stress shielding and loss of bone mass density in the surrounding bone, the bone stock is kept quite well using hip resurfacing techniques. By these studies it has been demonstrated illustratively that computational mechanics enables comparative studies on the biomechanical compatibility of bone implants.

Future research will concentrate on biologically motivated growth rules based on micromechanical concepts for modelling bone cells in an far realistic environment [22].



Fig. 4. Geometry of the cap-prosthesis, CAD model and generated FE model.

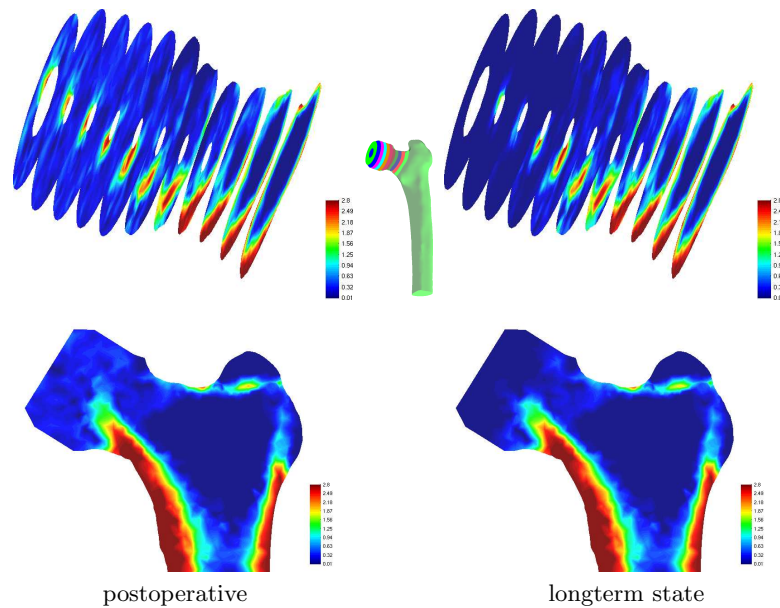


Fig. 5. Bone remodelling caused from hip resurfacing treatment.



Fig. 6. Bone mass distribution computed for a Zweymüller-prosthesis.

References

1. Wolff, J., *Das Gesetz der Transformation der Knochen*. Hirschwald, Berlin, 1892.
2. Pauwels, F.: *Atlas zur Biomechanik der gesunden und kranken Hüfte*, Springer, Berlin, 1973.
3. Carter, D. R.; Orr, T. E. & Fyhrie, D. P.: Relationship between loading history and femoral cancellous bone architecture. *Journal of Biomechanics* **22** (1989), 231–244.
4. Beaupre, G. S.; Orr, T. E. & Carter, D. R.: An Approach for Time-Dependent Bone Modeling and Remodeling — Theoretical Development. *Journal of Orthopaedic Research* **8**, (1990), 651–661.
5. Beaupre, G. S.; Orr, T. E. & Carter, D. R.: An Approach for Time-Dependent Bone Modelling and Remodelling: A Preliminary Remodeling Simulation. *Journal of Orthopaedic Research* **8** (1990), 662–670.
6. Weinans, H.; Huiskes, R. & Grootenboer, H. J.: The Behavior of Adaptive Bone Remodeling Simulation Models. *Journal of Biomechanics* **25** (1992), 1425–1441.
7. Nackenhorst, U.: Numerical simulation of stress stimulated bone remodeling. *Technische Mechanik* **17** (1997), 31–40.
8. Jacobs, C. R.; Levenston, M. E.; Beaupre, G. S.; Simo, J. C. & Carter, D. R.: Numerical instabilities in bone-remodeling simulations: the advantage of a

- node-based finite element approach. *Journal of Biomechanics* **28** (1995), 449–459.
9. Jacobs, C. R.; Simo, J. C.; Beaupre, G. S. & Carter, D. R.: Adaptive Bone Remodeling Incorporating Simultaneous Density and Anisotropy Considerations. *Journal of Biomechanics* **30** (1997), 603–613.
 10. Krstin, N.; Nackenhorst, U. & Lammering, R.: Zur konstitutiven Beschreibung des anisotropen beanspruchungsadaptiven Knochenumbaus. *Technische Mechanik* **20** (2000), 31–40.
 11. Doblare, M. & Garcia, J. M.: Anisotropic bone remodelling model based on a continuum damage–repair theory. *Journal of Biomechanics* **35** (2002), 1–17.
 12. Nackenhorst, U.: Computational Biomechanics of Bones. *Proceedings of Computer Methods in Mechanics, CMM–2005*, (2005).
 13. Carter, D. R. & Hayes, W. C.: The behavior of bone as a two-phase porous structure. *Journal of Bone and Joint Surgery* **59** (1997), 954–962.
 14. Rice, J. C.; Cowin, S. C. & Bowman, J. A.: On the Dependence of Elasticity and Strength of Cancellous Bone on Apparent Density. *Journal of Biomechanics* **21** (1988), 155–168.
 15. Simo, J. C. & Hughes, T. J. R.: *Computational Inelasticity*, Springer, Berlin, 1998.
 16. Zienkiewicz, O. C. & Zhu, J. Z.: The superconvergent patch recovery and a posteriori error estimates. Part 1: The recovery technique. *International Journal for Numerical Methods in Engineering* **33** (1992), 1331–1364.
 17. Bergmann, G.; Deuretzbacher, G.; Heller, M.; Graichen, F.; Rohlmann, A.; Strauss, J. & Duda, G. N.: Hip Contact Forces and Gait Pattern from Routine Activities. *Journal of Biomechanics* **34** (2001), 859–871.
 18. Duda, G.; Heller, M. & Bergmann, G.: Musculoskeletal loading database: loading conditions of the proximal femur. *Theoretical Issues in Ergonomics Science* **6** (2005), 287–292.
 19. Fischer, K. J.; Jacobs, C. R. & Carter, D. R.: Computational Method for Determination of Bone and Joints Loads using Bone Density Distributions. *Journal of Biomechanics* **28** (1995), 1127–1135.
 20. Ebbecke, B.: *Theoretische und algorithmische Konzepte zur Beschreibung des beanspruchungsadaptiven Knochenwachstums*, PhD–Thesis, University of Hanover, 2006.
 21. Hanebeck, J.: *Postoperative Knochendichteänderungen am Femur nach Implantation der zementfreien Zweymüller-Hüftendoprothese unter Berücksichtigung klinischer und röntgenologischer Parameter*, PhD–Thesis, Humboldt Universität Berlin, 2001.
 22. Lenz, C.: *Numerical Micro-Meso Modeling of Mechanosensation driven Osteonal Remodeling in Cortical Bone*, PhD–Thesis, University of Hanover, 2005.

Remodelling and Growth of Living Tissue – A Multiphase Theory

T. Ricken¹ & J. Bluhm²

¹ Computational Mechanics, ² Institute of Mechanics,
University of Duisburg-Essen, Campus Essen,
Universitätsstraße 15, 45117 Essen, Germany

Abstract. A continuum triphase model (i. e., a solid having the interstices filled with water containing nutrients) based on the Theory of Porous Media (TPM) is proposed for the phenomenological description of transversely isotropic biological tissues. However, the description of stress, strain or nutrient driven growth and remodelling phenomena is most notable. Finally, we gain a coupled solution to determine the solid motion, mixture temperature, inner pressure as well as the solid and nutrient volume fractions.

1 Introduction

Biological materials are characterized by their high functionality. Substantial characteristics of biological materials are the ability to grow or degenerate, vary their shape and inner structure to optimize the load transfer. For example, the arteries are composed of spiral fibres (double helix) gathering the tensile and inner pressure load. In an intervertebral disk the compression load is deflected over a fluid, which is stored in a strong impermeable tissue matrix. Plus, the bones might show an optimized internal density with internal structure distribution.

Thereby, growth and remodelling are continuous processes and result of a time depending phase conversion between tissue cells and nutrients, whereby the nutrients themselves can be transported through the tissue. Overall we consider that biological tissues mostly consist of multi-component materials, frequently showing an anisotropic internal structure plus reaction on changing load cases with internal biological and/or chemical activities. In terms of comprehensive overviews on the experimental findings of the growth phenomena, the reader is referred to, e. g., Fung [18, 19] and Taber [30]. An overview of different models for the description of growth phenomena can be found in Ricken et al. [26]. In this investigation, a description based on the Theory of Porous Media will be used, see Biot [4–6], Bowen [11, 12], Ehlers [15, 16], de Boer [10] or Bluhm [7].

The growth processes are driven by mechanical, chemical, genetic, metabolic, and hormonal influences. Due to the lack of detailed knowledge and specific parameters to quantify all these influences, a holistic numerical simulation can not be provided nowadays. However, the capability of tissue to remodel

its structure and density due to a changing stress state has been well known for over a century. Moreover, the precondition for tissue growth is the existence of a growth material like nutrients. Therefore, in this work a calculation concept is presented for the description of stress and nutrient induced growth based on the well established Theory of Porous Media.

2 Basic Model

The examined porous body consists of φ^S (solid) which is saturated by a fluid. The fluid itself is composed of φ^L (liquid) and φ^N (nutrients). The porous body occupies the control space of the porous solid B_S with the boundary ∂B_S and real volumes v^α where the index α denotes $\kappa \in \{S, L, N\}$ individual constituents. The boundary ∂B_S is a material surface for the solid phase and a non-material surface for the liquid and nutrient phases. The volume fractions n^α refer the volume elements dv^α of the individual constituents φ^α to the bulk volume element dv with

$$n^\alpha(\mathbf{x}, t) = \frac{dv^\alpha}{dv}, \quad \sum_{\alpha}^{S,L,N} n^\alpha(\mathbf{x}, t) = \sum_{\alpha}^{S,L,N} \frac{\rho^\alpha}{\rho^{\alpha R}} = 1, \quad (1)$$

where \mathbf{x} is the position vector of the spatial point x in the actual placement and t is the time, see, e. g., de Boer [10]. The volume fractions n^α in (1)₁ meet the volume fraction condition (1)₂ for κ constituents φ^α . Furthermore, the partial density $\rho^\alpha = n^\alpha \rho^{\alpha R}$ of the constituent φ^α is related to the real density of the materials $\rho^{\alpha R}$ involved via the volume fractions n^α , see (1)₂.

The saturated porous solid will be dealt with an immiscible mixture of all constituents φ^α with particles X_α , also with its own independent motion function

$$\mathbf{x} = \chi_\alpha(\mathbf{X}_\alpha, t), \quad \mathbf{X}_\alpha = \chi_\alpha^{-1}(\mathbf{x}, t), \quad (2)$$

where (2)₁ represents the Lagrange description of motion. The function χ_α is postulated to be unique and uniquely invertible at any time t . The existence of a function inverse to (2)₁ leads to the Euler description of motion, see (2)₂. A mathematical condition, which is necessary and sufficient for the existence of equation (2)₂, is given if the Jacobian $J_\alpha = \det \mathbf{F}_\alpha$ differs from zero. Therein, \mathbf{F}_α is the deformation gradient. \mathbf{F}_α and its inverse \mathbf{F}_α^{-1} are defined as $\mathbf{F}_\alpha = (\partial \mathbf{x}) / (\partial \mathbf{X}_\alpha) = \text{Grad}_\alpha \chi_\alpha$ and $\mathbf{F}_\alpha^{-1} = (\partial \mathbf{X}_\alpha) / (\partial \mathbf{x}) = \text{grad } \mathbf{X}_\alpha$. The differential operator “Grad_α” denotes a partial differentiation with respect to the reference position \mathbf{X}_α of the constituent φ^α and the differential operator “grad” referring to the spatial point \mathbf{x} . During the deformation process, \mathbf{F}_α is restricted to $\det \mathbf{F}_\alpha > 0$. The spatial velocity gradient $\mathbf{L}_\alpha = (\text{Grad}_\alpha \mathbf{x}'_\alpha) \mathbf{F}_\alpha^{-1} = \text{grad } \mathbf{x}'_\alpha$, where $(\mathbf{F}_\alpha)'_\alpha = (\partial \mathbf{x}'_\alpha) / (\partial \mathbf{X}_\alpha) = \text{Grad}_\alpha \mathbf{x}'_\alpha$ denotes the material velocity gradient, can be additively decomposed into a symmetric part $\mathbf{D}_\alpha = (\mathbf{L}_\alpha + \mathbf{L}_\alpha^T) / 2$ and a skew-symmetric part $\mathbf{W}_\alpha = (\mathbf{L}_\alpha - \mathbf{L}_\alpha^T) / 2$ with $\mathbf{L}_\alpha = \mathbf{D}_\alpha + \mathbf{W}_\alpha$.

With the Lagrange description of motion $(2)_1$, the velocity and acceleration fields of the constituents φ^α are defined as material time derivatives of the motion function $(2)_1$

$$\mathbf{x}'_\alpha = \frac{\partial \boldsymbol{\chi}_\alpha(\mathbf{X}_\alpha, t)}{\partial t}, \quad \mathbf{x}''_\alpha = \frac{\partial^2 \boldsymbol{\chi}_\alpha(\mathbf{X}_\alpha, t)}{\partial t^2}. \quad (3)$$

For scalar fields depending on \mathbf{x} and t , the material time derivatives are defined as follows

$$(\dots)'_\alpha = \frac{\partial(\dots)}{\partial t} + [\text{grad}(\dots)] \cdot \mathbf{x}'_\alpha, \quad (4)$$

with $\text{grad}(\dots) = \partial(\dots)/\partial \mathbf{x}$, see, e. g., de Boer [10].

The local statements of the balance equations of mass are given for the constituents φ^α by

$$(\rho^\alpha)'_\alpha + \rho^\alpha \text{div } \mathbf{x}'_\alpha = \hat{\rho}^\alpha, \quad (5)$$

and the local statements of the balance equations of momentum read as

$$\text{div } \mathbf{T}^\alpha + \rho^\alpha (\mathbf{b} - \mathbf{x}''_\alpha) + \hat{\mathbf{p}}^\alpha - \hat{\rho}^\alpha \mathbf{x}'_\alpha = \mathbf{0}. \quad (6)$$

In (5) and (6), 'div' denotes the spatial divergence operator, $\hat{\rho}^\alpha$ represents the mass supply between the phases which has to conform to

$$\hat{\rho}^S + \hat{\rho}^L + \hat{\rho}^N = 0, \quad (7)$$

\mathbf{T}^α is the partial Cauchy stress tensor, $\rho^\alpha \mathbf{b}$ specifies the volume force and $\hat{\mathbf{p}}^\alpha$ describes the interaction forces of momentum of the constituents φ^α which are restricted to

$$\hat{\mathbf{p}}^S + \hat{\mathbf{p}}^L + \hat{\mathbf{p}}^N = \mathbf{0}. \quad (8)$$

The last term $\hat{\rho}^\alpha \mathbf{x}'_\alpha$ on the left hand side of (6) describes the part of the momentum resulting from the mass supply. Due to the time scale of growth and remodelling processes in biological systems this part seems to be negligible for most of applications. Nevertheless, we should keep in mind that this growth momentum has to be considered if fast growth and remodelling processes are examined.

The balance of moment of momentum for non-polar materials states that the material time derivative of the moment of momentum is equal to the moments of all external forces. The evaluation of this balance equation yields Cauchy's second equation of motion, namely the symmetry of the stress tensor $\mathbf{T}^\alpha = (\mathbf{T}^\alpha)^T$. At last, in order to close the set of equations, the saturation condition $(1)_2$ must be considered.

In the further description, the system is investigated under the condition of a materially incompressible mixture body:

$$(\rho^{\text{SR}})'_S = 0, \quad (\rho^{\text{LR}})'_L = 0, \quad (\rho^{\text{NR}})'_N = 0, \quad (9)$$

which leads to the conclusion that the volumetric deformations are only a result from the change in the porosity, i.e., from the volume fraction n^S . In this approach, energy transfer will be neglected between all phases and accelerations are excluded ($\mathbf{x}''_\alpha = \mathbf{0}$).

3 Constitutive Modelling

For the treatment of the entropy inequality in analogy to Coleman & Noll [14], we define the set of free but not overall independent process variables

$$\mathcal{P} = \{\mathbf{C}_S, \mathbf{J}_L, \mathbf{J}_N, n^\alpha, \mathbf{w}_{LS}, \mathbf{w}_{NS}, \text{grad } n^L, \text{grad } n^N\}, \quad (10)$$

for fixed values of which the entropy inequality must hold and the free-available variables \mathcal{A} with

$$\mathcal{A} = \{\mathbf{D}_\alpha, (n^\alpha)'_\alpha\}, \quad (11)$$

which contains selective derivatives of the values contained in \mathcal{P} . In (10), besides the volume fractions n^α and the seepage velocities $\mathbf{w}_{LS} = \mathbf{x}'_L - \mathbf{x}'_S$ and $\mathbf{w}_{NS} = \mathbf{x}'_N - \mathbf{x}'_S$, additionally the right Cauchy-Green deformation tensor $\mathbf{C}_S = \mathbf{F}_S^T \mathbf{F}_S$ and the liquid and nutrient Jacobians \mathbf{J}_L and \mathbf{J}_N are considered. This is necessary because of the assumed mass transfers between the phases, which leads to the fact that the volume fractions can not, as usual, be expressed by the well known relation $J_\alpha = \rho_{0\alpha}^\alpha / \rho^\alpha = n_{0\alpha}^\alpha / n^\alpha$ gained from the integration of the local balance equation of mass.

In (10), the quantity n^N is not an independent process variable. Taking into account the saturation condition (1)₂, the volume fraction of the nutrient can be expressed by n^S and n^L . This dependence will be considered thru the evaluation of the entropy inequality. The entropy inequality for the isothermal triphasic mixture body

$$\begin{aligned} & \sum_{\alpha}^{\text{S,L,N}} \left\{ -\rho^\alpha (\psi^\alpha)'_\alpha - \hat{\rho}^\alpha \left(\psi^\alpha - \frac{1}{2} \mathbf{x}'_\alpha \cdot \mathbf{x}'_\alpha \right) + \right. \\ & \left. + \mathbf{T}^\alpha \cdot \mathbf{D}_\alpha + \hat{e}^\alpha - \hat{\mathbf{p}}^\alpha \cdot \mathbf{x}'_\alpha \right\} \geq 0 \end{aligned} \quad (12)$$

will be rearranged in such a way to ensure no neglecting of dependencies which can influence constitutive modelling. In order to keep the complexity of the evaluation in a justifiable scope, the dependency of the Helmholtz free energies ψ^α on the process variables \mathcal{P} will be restricted as follows:

$$\psi^S = \psi^S \{\mathbf{C}_S, n^S\}, \quad \psi^L = \psi^L \{\mathbf{J}_L, n^L\}, \quad \psi^N = \psi^N \{\mathbf{J}_N, n^N\}. \quad (13)$$

For further investigations, the relations $n^\alpha \rho^{\alpha R} (\psi^\alpha)'_\alpha$ will be replaced by¹

$$\begin{aligned}\rho^S (\psi^S)'_S &= 2 n^S \rho^{SR} \mathbf{F}_S \frac{\partial \psi^S}{\partial \mathbf{C}_S} \mathbf{F}_S^T \cdot \mathbf{D}_S + n^S \rho^{SR} \frac{\partial \psi^S}{\partial n^S} (n^S)'_S, \\ \rho^L (\psi^L)'_L &= n^L \rho^{LR} J_L \frac{\partial \psi^L}{\partial J_L} \mathbf{I} \cdot \mathbf{D}_L + n^L \rho^{LR} \frac{\partial \psi^L}{\partial n^L} (n^L)'_L, \\ \rho^N (\psi^N)'_N &= n^N \rho^{NR} J_N \frac{\partial \psi^N}{\partial J_N} \mathbf{I} \cdot \mathbf{D}_N + n^N \rho^{NR} \frac{\partial \psi^N}{\partial n^N} (n^N)'_N.\end{aligned}\quad (14)$$

For saturated porous media the saturation condition (1)₂ is a constraint with respect to the volumetric deformation of the constituents. Therefore, the saturation condition must be considered in view of the evaluation of the entropy inequality. Here, the material time derivative of the saturation condition will be used with

$$-(n^S)'_S - (n^L)'_L - (n^N)'_N + \text{grad } n^L \cdot \mathbf{w}_{LS} + \text{grad } n^N \cdot \mathbf{w}_{NS} = 0. \quad (15)$$

With respect to the evaluation of the the local statement of the entropy inequality (12) equation (15) has to be considered as a constraint, see, e. g., de Boer [9]. Therefore, we use the concept of Lagrange multipliers by adding (15) to the entropy inequality, multiplied by the scalar quantity λ with

$$\lambda \{\text{left hand side of (15)}\} = 0, \quad (16)$$

which does not modify the statement of (12). At last, the interconnection between the spatial velocity deformation gradients \mathbf{D}_α with the volume fractions and their material time derivative n^α and $(n^\alpha)'_\alpha$ as well as the mass supplies $\hat{\rho}^\alpha$ have to be reflected. In the case of no mass exchanges, this can be done by replacing the Jacobian by the volume fractions but in this investigation mass exchanges are considered. Hence, the local statements of the balance equations of mass (5) in the form

$$(n^\alpha)'_\alpha + n^\alpha (\mathbf{D}_\alpha \cdot \mathbf{I}) - \frac{\hat{\rho}^\alpha}{\rho^{\alpha R}} = 0, \quad (17)$$

will be added to the entropy inequality, which yield the interrelations mentioned above. Therefore, we gain to

$$\lambda^\alpha [(n^\alpha)'_\alpha + n^\alpha (\mathbf{D}_\alpha \cdot \mathbf{I}) - \frac{\hat{\rho}^\alpha}{\rho^{\alpha R}}] = 0, \quad (18)$$

which will be added to the entropy inequality. In (18), the Lagrange multipliers λ^α are non-dimensional.

¹ Here, use has been made of

$$\begin{aligned}(J_\alpha)'_\alpha &= \frac{\partial J_\alpha}{\partial \mathbf{F}_\alpha} \cdot (\mathbf{F}_\alpha)'_\alpha = \frac{\partial \det \mathbf{F}_\alpha}{\partial \mathbf{F}_\alpha} \cdot (\mathbf{F}_\alpha)'_\alpha = J_\alpha \mathbf{F}_\alpha^{\text{T}-1} \cdot (\mathbf{F}_\alpha)'_\alpha \mathbf{F}_\alpha^{-1} \mathbf{F}_\alpha = J_\alpha \mathbf{F}_\alpha^{\text{T}-1} \cdot \\ \mathbf{L}_\alpha \mathbf{F}_\alpha &= J_\alpha \mathbf{F}_\alpha \mathbf{F}_\alpha^{-1} \cdot \mathbf{L}_\alpha^{\text{T}} = J_\alpha \mathbf{I} \cdot \mathbf{D}_\alpha.\end{aligned}$$

The entropy inequality (12), enlarged by the material time derivative of saturation condition (16) and the balance equations of mass (18), both multiplied with the corresponding Lagrange multiplier, reads

$$\begin{aligned}
& \mathbf{D}_S \cdot \{ \mathbf{T}^S - 2 n^S \rho^{SR} \mathbf{F}_S \frac{\partial \psi^S}{\partial \mathbf{C}_S} \mathbf{F}_S^T + \lambda^S n^S \mathbf{I} \} + \\
& + \mathbf{D}_L \cdot \{ \mathbf{T}^L - n^L \rho^{LR} J_L \frac{\partial \psi^L}{\partial J_L} \mathbf{I} + \lambda^L n^L \mathbf{I} \} + \\
& + \mathbf{D}_N \cdot \{ \mathbf{T}^N - n^N \rho^{NR} J_N \frac{\partial \psi^N}{\partial J_N} \mathbf{I} + \lambda^N n^N \mathbf{I} \} - \\
& - (n^S)'_S \{ \lambda - \lambda^S + n^S \rho^{SR} \frac{\partial \psi^S}{\partial n^S} \} - \\
& - (n^L)'_L \{ \lambda - \lambda^L + n^L \rho^{LR} \frac{\partial \psi^L}{\partial n^L} \} - \\
& - (n^N)'_N \{ \lambda - \lambda^N + n^N \rho^{NR} \frac{\partial \psi^N}{\partial n^N} \} - \\
& - \hat{\rho}^L \{ (\psi^L - \frac{1}{2} \mathbf{x}'_L \cdot \mathbf{x}'_L + \frac{1}{\rho^{LR}} \lambda^L) - \\
& \quad - (\psi^S - \frac{1}{2} \mathbf{x}'_S \cdot \mathbf{x}'_S + \frac{1}{\rho^{SR}} \lambda^S) \} - \\
& - \hat{\rho}^N \{ (\psi^N - \frac{1}{2} \mathbf{x}'_N \cdot \mathbf{x}'_N + \frac{1}{\rho^{NR}} \lambda^N) - \\
& \quad - (\psi^S - \frac{1}{2} \mathbf{x}'_S \cdot \mathbf{x}'_S + \frac{1}{\rho^{SR}} \lambda^S) \} - \\
& - \mathbf{w}_{LS} \cdot \{ \hat{\mathbf{p}}^L - \lambda \text{grad } n^L \} - \\
& - \mathbf{w}_{NS} \cdot \{ \hat{\mathbf{p}}^N - \lambda \text{grad } n^N \} \geq 0,
\end{aligned} \tag{19}$$

where use has been made of

$$\hat{\rho}^S = -\hat{\rho}^L - \hat{\rho}^N, \quad \hat{\mathbf{p}}^S = -\hat{\mathbf{p}}^L - \hat{\mathbf{p}}^N. \tag{20}$$

With (11) the entropy inequality (19) can be satisfied if the following structure is obtained:

$$\begin{aligned}
& \underbrace{\mathbf{D}_S \cdot \{(\dots)\}}_{=0} + \underbrace{\mathbf{D}_L \cdot \{(\dots)\}}_{=0} + \underbrace{\mathbf{D}_N \cdot \{(\dots)\}}_{=0} - \\
& - \underbrace{(n^S)'_S \{(\dots)\}}_{=0} - \underbrace{(n^L)'_L \{(\dots)\}}_{=0} - \underbrace{(n^N)'_N \{(\dots)\}}_{=0} + \underbrace{Dis}_{\geq 0} \geq 0,
\end{aligned} \tag{21}$$

where

$$\begin{aligned}
Dis = & \\
& -\hat{\rho}^L \left\{ (\psi^L - \frac{1}{2} \mathbf{x}'_L \cdot \mathbf{x}'_L + \frac{1}{\rho^{LR}} \lambda^L) - (\psi^S - \frac{1}{2} \mathbf{x}'_S \cdot \mathbf{x}'_S + \frac{1}{\rho^{SR}} \lambda^S) \right\} - \\
& -\hat{\rho}^N \left\{ (\psi^N - \frac{1}{2} \mathbf{x}'_N \cdot \mathbf{x}'_N + \frac{1}{\rho^{NR}} \lambda^N) - (\psi^S - \frac{1}{2} \mathbf{x}'_S \cdot \mathbf{x}'_S + \frac{1}{\rho^{SR}} \lambda^S) \right\} - \\
& - \mathbf{w}_{LS} \cdot \{ \hat{\mathbf{p}}^L - \lambda \text{grad } \mathbf{n}^L \} - \mathbf{w}_{NS} \cdot \{ \hat{\mathbf{p}}^N - \lambda \text{grad } \mathbf{n}^N \} \geq 0.
\end{aligned} \tag{22}$$

Considering the aforementioned remarks, we obtain necessary and sufficient conditions for the unrestricted validity of the second law of thermodynamics. Firstly, with the relation

$$\lambda^\alpha = \lambda + n^\alpha \rho^{\alpha R} \frac{\partial \psi^\alpha}{\partial n^\alpha}, \tag{23}$$

we obtain for the Cauchy stress tensors

$$\begin{aligned}
\mathbf{T}^S &= 2 n^S \rho^{SR} \mathbf{F}_S \frac{\partial \psi^S}{\partial \mathbf{C}_S} \mathbf{F}_S^T - (n^S)^2 \rho^{SR} \frac{\partial \psi^S}{\partial n^S} \mathbf{I} - n^S \lambda \mathbf{I}, \\
\mathbf{T}^L &= n^L \rho^{LR} J_L \frac{\partial \psi^L}{\partial J_L} \mathbf{I} - (n^L)^2 \rho^{LR} \frac{\partial \psi^L}{\partial n^L} \mathbf{I} - n^L \lambda \mathbf{I}, \\
\mathbf{T}^N &= n^N \rho^{NR} J_N \frac{\partial \psi^N}{\partial J_N} \mathbf{I} - (n^N)^2 \rho^{NR} \frac{\partial \psi^N}{\partial n^N} \mathbf{I} - n^N \lambda \mathbf{I}.
\end{aligned} \tag{24}$$

In view of the dissipative mechanism, the following approaches for the interaction forces $\hat{\mathbf{p}}^L$ and $\hat{\mathbf{p}}^N$ as well as the mass supplies $\hat{\rho}^L$ and $\hat{\rho}^N$ are postulated:

$$\begin{aligned}
\hat{\mathbf{p}}^L &= \lambda \text{grad } \mathbf{n}^L - \mathbf{S}_L \mathbf{w}_{LS} - \beta_{\hat{\mathbf{p}}}^{LN} \mathbf{w}_{NS}, \\
\hat{\mathbf{p}}^N &= \lambda \text{grad } \mathbf{n}^N - \mathbf{S}_N \mathbf{w}_{NS} + \beta_{\hat{\mathbf{p}}}^{LN} \mathbf{w}_{LS}, \\
\hat{\rho}^L &= -\delta_{\hat{\rho}}^L (\Psi^L - \Psi^S) - \delta_{\hat{\rho}}^{SLN} (\Psi^N - \Psi^S) - \delta_{\hat{\rho}}^{LN} (\Psi^L - \Psi^N), \\
\hat{\rho}^N &= -\delta_{\hat{\rho}}^N (\Psi^N - \Psi^S) + \delta_{\hat{\rho}}^{SLN} (\Psi^L - \Psi^S) + \delta_{\hat{\rho}}^{LN} (\Psi^L - \Psi^N),
\end{aligned} \tag{25}$$

with

$$\begin{aligned}
\mathbf{S}_L &= \alpha_{L0} [\alpha_{L1} \mathbf{I} + \alpha_{L2} \bar{\mathbf{M}}]^{-1} + \alpha_{L3} \mathbf{I}, \\
\mathbf{S}_N &= \alpha_{N0} [\alpha_{N1} \mathbf{I} + \alpha_{N2} \bar{\mathbf{M}}]^{-1} + \alpha_{N3} \mathbf{I},
\end{aligned} \tag{26}$$

where $\bar{\mathbf{M}}$ defines an arbitrary positive definite second order tensor. Moreover, in (25) use has been made of the abbreviation for the chemical potential functions

$$\Psi^\alpha = \psi^\alpha - \frac{1}{2} \mathbf{x}'_\alpha \cdot \mathbf{x}'_\alpha + n^\alpha \frac{\partial \psi^\alpha}{\partial n^\alpha} + \frac{1}{\rho^{\alpha R}} \lambda. \tag{27}$$

With these approaches, the dissipation mechanism (22) means

$$\begin{aligned} Dis &= \mathbf{S}_L \mathbf{w}_{LS} \cdot \mathbf{w}_{LS} + \mathbf{S}_N \mathbf{w}_{NS} \cdot \mathbf{w}_{NS} + \\ &+ \delta_{\rho}^L (\Psi^L - \Psi^S)^2 + \delta_{\rho}^N (\Psi^N - \Psi^S)^2 + \delta_{\rho}^{LN} (\Psi^L - \Psi^N)^2 \geq 0, \end{aligned} \quad (28)$$

and is fulfilled if the restrictions

$$\alpha_{\beta\{0,1,2,3\}} \geq 0, \quad \delta_{\rho}^{\beta} \geq 0, \quad \delta_{\rho}^{LN} \geq 0, \quad (29)$$

with $\beta \in \{N, L\}$ and $\mathbf{S}_L, \mathbf{S}_N$ as positive definite second order tensor hold.

In the further investigation we assume that the nutrient phase φ^N is included in the liquid phase φ^L with

$$\varphi^F = \varphi^L + \varphi^N, \quad \mathbf{n}^F = \mathbf{n}^L + \mathbf{n}^N, \quad \rho^{FR} = \frac{\mathbf{n}^L}{\mathbf{n}^F} \rho^{LR} + \frac{\mathbf{n}^N}{\mathbf{n}^F} \rho^{NR}, \quad (30)$$

i. e., both phases are assigned to the same velocity $\mathbf{x}'_F = \mathbf{x}'_L = \mathbf{x}'_N$ and to the same pressure λ .

3.1 Stress

With the assumptions $\partial\psi^F/\partial J_F = 0$ and $\partial\psi^F/\partial \mathbf{n}^F = 0$ where $\varphi^F = \varphi^L + \varphi^N$ and from (24) we gain the following constitutive relations for the partial Cauchy stress tensors

$$\begin{aligned} \mathbf{T}^S &= -\mathbf{n}^S \lambda \mathbf{I} - (\mathbf{n}^S)^2 \rho^{SR} \frac{\partial\psi^S}{\partial \mathbf{n}^S} \mathbf{I} + 2 \rho^S \mathbf{F}_S \frac{\partial\psi^S}{\partial \mathbf{C}_S} \mathbf{F}_S^T \\ &= -\mathbf{n}^S \lambda \mathbf{I} - (\mathbf{n}^S)^2 \rho^{SR} \frac{\partial\psi^S}{\partial \mathbf{n}^S} \mathbf{I} + \mathbf{T}_E^S, \\ \mathbf{T}^F &= -(\mathbf{n}^L + \mathbf{n}^N) \lambda \mathbf{I} = -\mathbf{n}^F \lambda \mathbf{I}, \quad \mathbf{n}^F = \mathbf{n}^L + \mathbf{n}^N, \end{aligned} \quad (31)$$

of the constituents solid and fluid with the realistic fluid pressure λ .

A convenient and common way to formulate anisotropic constitutive relations is the usage of the concept of integrity bases which allows a coordinate-invariant formulation, see, e. g., Spencer [29], Boehler [8], Betten [3] or Zheng & Spencer [31, 32]. In this contribution we will restrict ourselves to a transversely isotropic material response, i. e., only materials with one preferred direction will be considered. Therefore, we introduce the so-called structural tensor $\mathbf{M} = \mathbf{A} \otimes \mathbf{A}$ where \mathbf{A} denotes the preferred \mathbf{A} -axis with $\|\mathbf{A}\| = 1$ with respect to the reference configuration. The stored energy function will be formulated in dependency of the principle invariants $I_{1,2,3}$ of \mathbf{C}_S and the basic invariants $J_{4,5}$ of the argument tensors $(\mathbf{C}_S, \mathbf{M})$ with

$$\begin{aligned} I_1 &:= \text{tr} \mathbf{C}_S, & I_2 &:= \text{tr}[\det[\mathbf{C}_S] \mathbf{C}_S^{-T}] = \text{tr}[\text{Cof} \mathbf{C}_S], \\ I_3 &:= \det \mathbf{C}_S = J_S^2, & J_4 &:= \text{tr}[\mathbf{C}_S \mathbf{M}], & J_5 &:= \text{tr}[\mathbf{C}_S^2 \mathbf{M}], \end{aligned} \quad (32)$$

see, e. g., Reese et al. [22] or Schröder et al. [28]. Now we are able to construct the solid Helmholtz free energy function, which will be decomposed into an isotropic part $\psi_{\text{iso}}^{\text{S}}$ and a transversely isotropic part $\psi_{\text{ti}}^{\text{S}}$, i. e.,

$$\begin{aligned}\psi^{\text{S}} &= \hat{\psi}^{\text{S}}(n^{\text{S}}, I_1, I_2, I_3, J_4, J_5) = \psi_{\text{iso}}^{\text{S}}(n^{\text{S}}, I_1, I_2, I_3) + \psi_{\text{ti}}^{\text{S}}(J_4, J_5) \\ &= \left(\frac{n^{\text{S}}}{n_{0\text{S}}^{\text{S}}}\right)^n \psi_{\text{iso, neo}}^{\text{S}}(I_1, I_2, I_3) + \psi_{\text{ti}}^{\text{S}}(J_4, J_5).\end{aligned}\quad (33)$$

The term in (33) connected with the solid volume fraction n^{S} describes the change of solid rigidity relating to the reference solid volume fraction $n_{0\text{S}}^{\text{S}}$ at $t = t_0$. Carter & Hayes [13] identified the material parameter n in (33) from in situ experiments of human and bovine trabecular bone specimens with and without marrow to a value of $n = 3$, see also Nackenhurst [21]. However, from experimental investigations done by Rice et al. [23] as well as a thermodynamical consistent derivation done by Krstin et al. [20], the density-elasticity relation parameter n is defined with a value of $n = 2$. The isotropic part of the Helmholtz free energy function $\psi_{\text{iso, neo}}^{\text{S}}$ is of Neo-Hookean type, viz:

$$\begin{aligned}\psi_{\text{iso, neo}}^{\text{S}} &= \psi_{\text{iso, neo}}^{\text{S}}(I_1, J_S = \sqrt{I_3}) \\ &= \frac{1}{\rho_{0\text{S}}^{\text{S}}} \left\{ \lambda^{\text{S}} \frac{1}{2} (\ln J_S)^2 - \mu^{\text{S}} \ln J_S + \frac{1}{2} \mu^{\text{S}} (I_1 - 3) \right\},\end{aligned}\quad (34)$$

where μ^{S} and λ^{S} are the macroscopic Lamé constants. For the transversely isotropic part of the Helmholtz free energy function we choose for this first approach a slightly modified function suggested, e. g., in Reese et al. [22] with

$$\psi_{\text{ti}}^{\text{S}} = \psi_{\text{ti}}^{\text{S}}(J_4) = \begin{cases} \frac{1}{2\rho_{0\text{S}}^{\text{S}}} \alpha_1 (J_4 - 1)^{\alpha_2} & \text{for } J_4 \geq 1, \\ 0 & \text{for } J_4 < 1, \end{cases}\quad (35)$$

where $\alpha_1 \geq 1$ and $\alpha_2 > 1$ are parameters due to the stiffness of the preferred direction \mathbf{A} . Due to the structure of ψ^{S} both the invariance condition and the polyconvexity condition are satisfied. The latter implies quasiconvexity which ensures, under some further technical assumptions, the existence of minimizers of related variational principles in finite elasticity, see, e. g., Ball [1], Schröder & Neff [27] or Balzani et al. [2] and references therein. In (35), the distinction of case represents the reasonable assumption that in living soft tissues the preferred direction results from fibres, which cause no stress in the case of shortening. Due to the fact that J_4 represents the squared stretch in the fibre direction \mathbf{A} , the suggested decomposition in (35) appears suitable. In the case of hard tissues, the distinction of case in (35) can be neglected for $J_4 < 1$.

With (31)₁ and (33)-(35), the solid effective Cauchy stress tensor reads

$$\mathbf{T}_{\text{E}}^{\text{S}} = 2\rho^{\text{S}} \mathbf{F}_{\text{S}} \frac{\partial \psi^{\text{S}}}{\partial \mathbf{C}_{\text{S}}} \mathbf{F}_{\text{S}}^{\text{T}} = \left(\frac{n^{\text{S}}}{n_{0\text{S}}^{\text{S}}}\right)^n J_{\text{S}} \frac{\rho^{\text{S}}}{\rho_{0\text{S}}^{\text{S}}} \mathbf{T}_{\text{E, iso, neo}}^{\text{S}} + J_{\text{S}} \frac{\rho^{\text{S}}}{\rho_{0\text{S}}^{\text{S}}} \mathbf{T}_{\text{E, ti}}^{\text{S}}, \quad (36)$$

where

$$\begin{aligned}\mathbf{T}_{E, \text{iso, neo}}^S &= \frac{1}{J_S} [2 \mu^S \mathbf{K}_S + \lambda^S (\ln J_S) \mathbf{I}], \\ \mathbf{T}_{E, \text{ti}}^S &= \frac{1}{J_S} \alpha_1 \alpha_2 [\text{tr}(\mathbf{C}_S \mathbf{M}) - 1]^{\alpha_2 - 1} \mathbf{F}_S \mathbf{M} \mathbf{F}_S^T \\ &= \frac{1}{J_S} \alpha_1 \alpha_2 [\text{tr}(\mathbf{m}) - 1]^{\alpha_2 - 1} \mathbf{m}.\end{aligned}\quad (37)$$

Herein, the Karni-Reiner strain $\mathbf{K}_S = 1/2 (\mathbf{B}_S - \mathbf{I})$ with the left Cauchy-Green tensor $\mathbf{B}_S = \mathbf{F}_S \mathbf{F}_S^T$ and $\mathbf{m} = \mathbf{F}_S \mathbf{A} \otimes \mathbf{F}_S \mathbf{A} = \mathbf{a} \otimes \mathbf{a}$ as the structural tensor has been used, both related to the actual placement.

3.2 Filter Velocity and Transversely Isotropic Permeability

The solid body is saturated by the fluid phase. The motions of both solid and fluid are connected by the interaction forces $\hat{\mathbf{p}}^F = \hat{\mathbf{p}}^L + \hat{\mathbf{p}}^N = -\hat{\mathbf{p}}^S$. From (25)_{1,2} with $\beta_{\mathbf{p}}^{\text{LN}} = 0$ for the constitutive modelling of $\hat{\mathbf{p}}^F$ we gain the restriction

$$\hat{\mathbf{p}}^F = \lambda \text{grad } n^F - \mathbf{S}_F \mathbf{w}_{FS}, \quad (38)$$

where $\mathbf{S}_F = \mathbf{S}_L + \mathbf{S}_N$ with (26) is obtained with

$$\mathbf{S}_F = \alpha_{F0} [\alpha_{F1} \mathbf{I} + (1 - \alpha_{F1}) \mathbf{M}]^{-1} + \alpha_{F3} \mathbf{I}. \quad (39)$$

In (39), the parameter α_{F2} was replaced by the relation $\alpha_{F2} = 1 - \alpha_{F1}$ which allows a weighting between the fully isotropic state ($\alpha_{F1}=1$) and the complete transverse isotropic state ($\alpha_{F1}=0$). From (6) with (31)₂, (38), and (39) with $\alpha_{F3} = \hat{\rho}^F$, where with respect to (29)₁ $\alpha_{F0} \alpha_{F1} + \alpha_{F3} \geq 0$ has to be ensured, as well as the assumption $\mathbf{x}_F'' = \mathbf{o}$, we derive the balance equation of momentum for the fluid phase in the form

$$\begin{aligned}\text{div} (-n^F \lambda \mathbf{I}) + \rho^F \mathbf{b} + \lambda \text{grad } n^F - \\ - (\alpha_{F0} [\alpha_{F1} \mathbf{I} + (1 - \alpha_{F1}) \mathbf{M}]^{-1}) \mathbf{w}_{FS} - \hat{\rho}^F \mathbf{x}'_S = \mathbf{o}.\end{aligned}\quad (40)$$

The last term $\hat{\rho}^F \mathbf{x}'_S$ on the left hand side of (40) describes the influence of the mass supply due to the momentum of the body. In order to obtain a determination for the filter velocity $n^F \mathbf{w}_{FS}$, we rearrange (40) to

$$n^F \mathbf{w}_{FS} = \frac{(n^F)^2}{\alpha_{F0}} [\alpha_{F1} \mathbf{I} + (1 - \alpha_{F1}) \mathbf{M}] (-\text{grad } \lambda + \rho^{\text{FR}} \mathbf{b} - \frac{\hat{\rho}^F}{n^F} \mathbf{x}'_S). \quad (41)$$

The base permeability can either be described by use of the initial Darcy permeability k_{0S}^F [m/s] and the specific weight γ^{FR} [N/m³] or of the intrinsic solid permeability k_{0S}^S [m²] and the effective shear viscosity μ^{FR} [Ns/m²], where

$$\frac{(n^F)^2}{\alpha_{F0}} = \left(\frac{n^F}{1 - n_{0S}^S} \right)^m \frac{k_{0S}^F}{\gamma^{\text{FR}}} = \left(\frac{n^F}{1 - n_{0S}^S} \right)^m \frac{k_{0S}^S}{\mu^{\text{FR}}} \quad (42)$$

and m denotes a dimensionless material parameter, see also Eipper [17], Ehlers [16], Ricken [24] or Ricken & de Boer [25].

3.3 Mass Supply

As mentioned before, we assume a mass exchange which acts only between the solid and nutrient phase ($\hat{\rho}^N = -\hat{\rho}^S$, $\hat{\rho}^L = 0$). Additionally, the assumptions $\Psi^L - \Psi^S = 0$, and $\Psi^L - \Psi^N = 0$ are made. This simplification is explained by the fact that no expert knowledge is available in view of the formulation of the aforementioned functions. Thus, with respect to the description of remodelling processes, the mass supply term of the solid phase will be formulated directly. With (25)₄, the solid mass supply is defined by

$$\hat{\rho}^S = \delta_{\hat{\rho}}^N (\Psi^N - \Psi^S), \quad (43)$$

where $\delta_{\hat{\rho}}^N \geq 0$, see (29)₂. In view of a growth and degeneration description in biological tissues it is necessary to allow a change in sign for $\hat{\rho}^S$, depending on the direction of the process. Accordingly, the chemical potential functions are interconnected as follows:

$$\hat{\rho}^S \geq 0 \quad \rightarrow \quad \Psi^N \geq \Psi^S, \quad \hat{\rho}^S \leq 0 \quad \rightarrow \quad \Psi^N \leq \Psi^S. \quad (44)$$

As a first approach, we postulate $\hat{\rho}^S$ as a function of the total Kirchhoff solid stresses, the solid Jacobian and the nutrient content, i. e.,

$$\hat{\rho}^S = \hat{\rho}^S(\mathbf{n}^N, \boldsymbol{\tau}^S, J_S) = \hat{\rho}^S(\mathbf{n}^N, \mathbf{n}^S, \lambda, \mathbf{C}_S, J_S). \quad (45)$$

In order to define the stress dependency of the mass exchange, we introduce the effective stress τ_{vMi} related to the distortion strain energy of von Mises. The mass exchange rate between the solid and nutrient phase in (45) is postulated in dependence on the nutrient content \mathbf{n}^N , the solid Jacobian J_S and the effective solid stresses τ_{vMi} with

$$\begin{aligned} \hat{\rho}^S &= \hat{\rho}_{\text{max}}^S \hat{\rho}_{\mathbf{n}^N}^S \hat{\rho}_{J_S}^S \hat{\rho}_{\tau_{\text{vMi}}}^S, \\ \hat{\rho}_{\mathbf{n}^N}^S &= -\exp[-\kappa_{\mathbf{n}^N} (\mathbf{n}^N)^2] + 1, \\ \hat{\rho}_{J_S}^S &= -\exp[-\kappa_{J_S} (J_S - 1)^2] + 1, \\ \hat{\rho}_{\tau_{\text{vMi}}}^S &= -2 \exp[-\log(2) \tau_{\text{vMi}}/\tau_{\text{vMi}0}] + 1, \end{aligned} \quad (46)$$

where $\hat{\rho}_{\text{max}}^S$ [kg/(s m³)] denotes the maximum mass exchange rate, $\kappa_{\mathbf{n}^N}$ and κ_{J_S} are parameters due to the nutrient and strain dependency respectively and $\tau_{\text{vMi}0}$ defines the optimal effective stress state where no mass exchange is expected. Although, the knowledge about the capability of biological tissues to grow and remodel is rather old, data for the parameters are difficult to obtain. Therefore, in the numerical examples we choose parameters which are reasonable with respect to the solutions. At present, a parameter study is treated by the authors. In Figure 1, the characteristics of $\hat{\rho}_{\mathbf{n}^N}^S$, $\hat{\rho}_{J_S}^S$, and $\hat{\rho}_{\tau_{\text{vMi}}}^S$ are given.

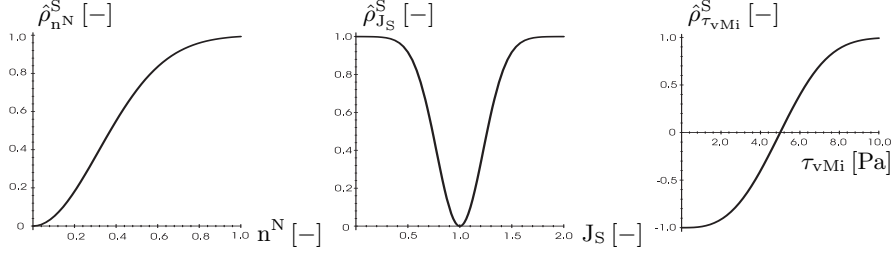


Fig. 1. Constituent parts of the mass transfer rate $\hat{\rho}^S$ with $\kappa_{n^N} = 5$, $\kappa_{J_S} = 10$, and $\tau_{vMi0} = 5$.

4 Numerical Treatment

Weak formulations are formed within the framework of a standard Galerkin procedure. Under consideration of all assumptions made plus the constrain conditions and the constitutive equations, we obtain the set \mathfrak{R} of unknown quantities with five independent fields $\mathfrak{R} = \mathfrak{R}(\mathbf{x}, t) = \{\mathbf{u}_S, \mathbf{w}_{FS}, n^S, n^N, \lambda\}$ wherein \mathbf{u}_S denotes the displacement of the solid phase. The filter velocity $n^F \mathbf{w}_{FS}$ will be calculated using the balance of momentum from (41). Finally, the set of unknown quantities \mathfrak{R} can be reduced to four quantities with

$$\mathfrak{R} = \mathfrak{R}(\mathbf{x}, t) = \{\mathbf{u}_S, n^S, n^N, \lambda\}. \quad (47)$$

In order to determine the independent fields given in (47), weak forms have to be formed. Therefore, we use for the mixture the sum of the balance equations of momentum (6) multiplied with the weight function $\delta \mathbf{u}_S$ as well as the balance equations of mass (5) of the overall mixture, solid, and nutrient phase multiplied with the weight functions $\delta \lambda$, δn^S , and δn^N , respectively. As a result, the used set of equations according to the actual placement can be evaluated to weak forms which are given in Ricken et al [26].

The weak forms of the balance equations are implemented in the well known finite element program FEAP developed by Taylor. The finite element discretization was realized with the Galerkin method. In order to ensure stable numerical results, so called Taylor-Hood elements are used with quadratic ansatz functions for \mathbf{u}_S and linear ansatz functions for λ , n^S , and n^N .

5 Numerical Example

Notably, the following examples are more or less of academic character. This is caused by the fact that for some parameters no realistic quantities are known at the current state. Due to the manifold number of load cases and material properties of living biological tissues the description necessitated much simplification before a solution could be attempted. Basically, in the

numerical example presented, the performance of our calculation concept can be obtained. In view of further investigations and biological knowledge, this model is able to describe the basic behaviour of biological tissues and can be expanded to further findings.

5.1 Transverse Isotropic Material Behaviour

Within many biological materials, an anisotropic material behaviour, which is caused by the internal structure of the material, can be observed. For example the transverse isotropic behaviour of a muscle results from the muscle fibres which are arranged in bundles. Thereby, the muscle behaves more rigid in the direction of the fibres than perpendicular to it, see Figure 2. The material parameters are given in Table 1.

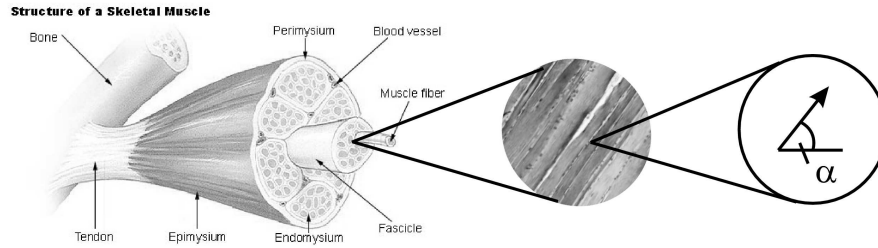


Fig. 2. Transverse Isotropic structure of a muscle.

Parameter	Value	Unit	Parameter	Value	Unit
μ^S	$1 \cdot 10^3$	Pa	$\hat{\rho}_{\max}^S$	0	kg/d m ³
λ^S	0	Pa	k_{0S}^F	$8.3 \cdot 10^2$	m/d
ρ_{0S}^{SR}	$2 \cdot 10^2$	kg/m ³	γ^{FR}	$1.0 \cdot 10^4$	N/m ³
ρ_{0S}^{LR}	$1 \cdot 10^3$	kg/m ³	α_{F1}	1.0	—
ρ_{0S}^{NR}	$1 \cdot 10^3$	kg/m ³	α_{F3}	0.0	—
n_{0S}^S	0.5	—	α_1	$1.0 \cdot 10^3$	—
n_{0S}^L	0.45	—	α_2	3.0	—
n_{0S}^N	0.05	—	m	0	—

Table 1. Parameters for tension test.

In order to clarify the anisotropic material behaviour, a calculation of a disk including a cavity has been carried out. Thus, a tension test with a sample specimen is simulated which possesses a circular defect in the centre. The specimen is fastened at the left side and pulled on the right side; the upper and lower surface are free, see Figure 3 (a).

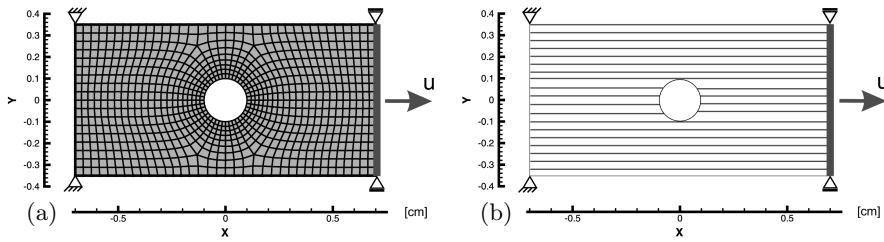


Fig. 3. Boundary conditions and discretization (a) and transverse isotropic material structure (b) for tension test.

The specimen consists of solid matrix that is filled with fluid. The fluid can not leave the sample test specimen at the edges. However, in this example, no mass exchanges are considered. In the first case the solid matrix consists of an isotropic material, whereas in the second case it behaves transverse isotropic, i. e., the fibres in horizontal direction are strengthened, see Figure 3 (b).

As shown in in Figure 4, the deformation behaviour of the two materials differs during the same load. At the edges of the defect the isotropic material is affected by large volume stains (red and blue range), whereas the volume strains in the case of the transverse-isotropic material have a low distribution around the defect. From this we can consider that a biological material, which is reinforced by fibres, will protect injuries against large load peaks.

5.2 Optimized Organic Structures

Apart from the growth process, biological materials are able to adapt their internal structure for a given load case. A substantial characteristic is the optimization of weight reduction, where structures are only formed where it is necessary for stability. An example is the structure of our skeleton which was developed by evolution to a system optimal for our purposes. This evolutionary process is subjected to the following simulation. In order to come closer to this phenomenon, a simple study of a cantilever with a given load is regarded, see Figure 5. In the example, the material distribution evaluates to the state of optimal stress and low strain state. The material parameters are given in Table 2. In Figure 5 (a) the red areas mark the places with a high mass content, while the blue ranges refer to a low material one. In Figure 5 (b) the pertinent change of the effective stress is represented. It can be recognized that the inner structure of the cantilever adjusts itself to the given load so that an optimal structure is finally formed. In the case of any changes in the load case, the formed structure would change again. With this simulation it is possible to optimize technical products as well as, e. g., the basic structure of an automobile.

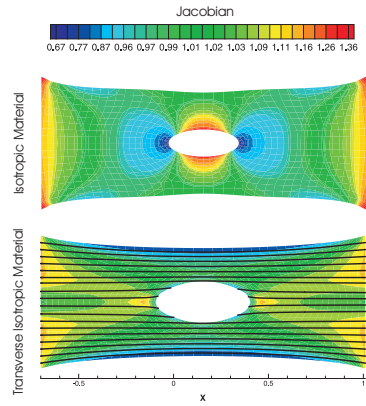


Fig. 4. Volumetric strain distribution for isotropic and transverse isotropic biological material.

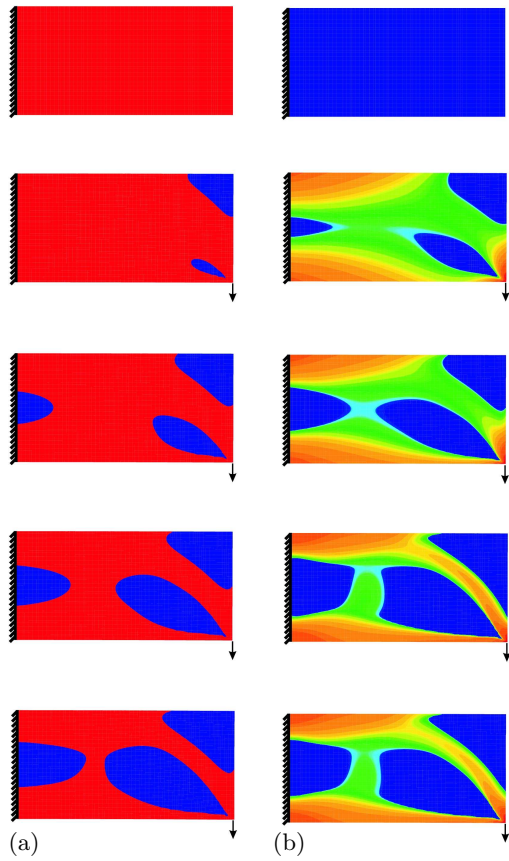


Fig. 5. Structure optimization of organic material: material (a) and effective stress (b). Load = 2 kN.

Parameter	Value	Unit	Parameter	Value	Unit
μ^S	$1 \cdot 10^4$	Pa	$\hat{\rho}_{\max}^S$	1	kg/d m ³
λ^S	0	Pa	k_{0S}^F	$8.3 \cdot 10^2$	m/d
ρ_{0S}^{SR}	$0.2 \cdot 10^{-3}$	g/mm ³	γ^{FR}	$1.0 \cdot 10^4$	N/m ³
ρ_{0S}^{LR}	$1.0 \cdot 10^{-3}$	g/mm ³	α_{F1}	1.0	–
ρ_{0S}^{NR}	$0.2 \cdot 10^{-3}$	g/mm ³	α_{F3}	0.0	–
n_{0S}^S	0.5	–	α_1	$1.0 \cdot 10^3$	–
n_{0S}^L	0.05	–	α_2	3.0	–
n_{0S}^N	0.45	–	m	0	–
κ_{nN}	5.0	–	κ_{JS}	$2.0 \cdot 10^6$	–
τ_{vM10}	10.0	N/mm ²			

Table 2. Parameters for Structure optimization test.

References

1. Ball, J. M.: Convexity conditions and existence theorems in non-linear elasticity. *Archive of Rational Mechanics and Analysis* **63** (1977), 337–403.
2. Balzani, D.; Neff, P.; Schröder, J. & Holzapfel, G. A.: A polyconvex framework for soft biological tissues. Adjustment to experimental data. *International Journal of Solids and Structures*, **43** (2006), 6052–6070.
3. Betten, J.: Formulation of anisotropic constitutive equations. In Boehler, J. P. (ed.): *Applications of Tensor Functions in Solid Mechanics*, CISM Course No. 292, Springer-Verlag, Berlin, 1987.
4. Biot, M. A.: Le problème de la consolidation des matières argileuses sous une charge. *Annales de la Societ scientifique de Bruxelles B* **55** (1935), 110–113.
5. Biot, M. A.: General theory of three-dimensional consolidation. *Journal of Applied Physics* **12** (1941), 155–164.
6. Biot, M. A.: Theory of propagation of elastic waves in a fluid-saturated porous solid. I. Low-frequency range. *Journal of Acoustical Society of America* **28** (1956), 168–178.
7. Bluhm, J.: Modelling of saturated thermo-elastic porous solids with different phase temperatures. In Ehlers, W. & Bluhm, J. (eds.): *Porous Media: Theory, Experiments and Numerical Applications*, Springer-Verlag, Berlin, 2002.
8. Boehler, J. P.: Introduction to the invariant formulation of anisotropic constitutive equations. In Boehler, J. P. (ed.): *Applications of Tensor Functions in Solid Mechanics*, CISM Course No. 292, Springer-Verlag, Berlin, 1987.
9. de Boer, R.: Highlights in the historical development of the porous media theory – toward a consistent macroscopic theory. *Applied Mechanics Review* **49** (1996), 201–262.
10. de Boer, R.: *Theory of Porous Media: highlights in the historical development and current state*. Springer-Verlag, Berlin, 2000.

11. Bowen, R. M.: Incompressible Porous Media models by use of the theory of mixtures. *International Journal of Engineering Science* **18** (1980), 1129–1148.
12. Bowen, R. M.: Compressible Porous Media models by use of the theory of mixtures. *International Journal of Engineering Science* **20** (1982), 697–735.
13. Carter, D. R. & Hayes, W. C.: The compressive behavior of bone as a two-phase porous structure. *The Journal of Bone and Joint Surgery* **59** (1977), 954–962.
14. Coleman, B. D. & Noll, W.: The thermodynamics of elastic materials with heat conduction and viscosity. *Archives for Rational Mechanics and Analysis* **13** (1963), 167–178.
15. Ehlers, W.: *Poröse Medien – ein kontinuumsmechanisches Modell auf der Basis der Mischungstheorie*. Forschungsbericht aus dem Fachbereich Bauwesen **47**, Universität-GH Essen 1989.
16. Ehlers, W.: Foundations of multiphasic and porous materials. In Ehlers, W. & Bluhm, J. (eds.): *Porous Media: Theory, Experiments and Numerical Applications*, Springer-Verlag, Berlin, 2002, pp. 3–86.
17. Eipper, G.: *Theorie und Numerik finiter elastischer Deformationen in fluidgesättigten porösen Medien*. Dissertation, Bericht Nr. II-1 aus dem Institut für Mechanik (Bauwesen), Universität Stuttgart, 1998.
18. Fung, Y. C.: *Biomechanics - Motion, flow, stress, and growth*. Springer-Verlag, Berlin, 1990.
19. Fung, Y. C.: *Biomechanics - Mechanical properties of living tissues*. Springer-Verlag, Berlin, 1993.
20. Krstin, N.; Nackenhorst, U. & Lammering, R.: Zur konstitutiven Beschreibung des anisotropen beanspruchungs-adaptiven Knochenumbaus. *Technische Mechanik* **20** (2000), 31–40.
21. Nackenhorst, U.: Numerical simulations of stress stimulated bone remodeling. *Technische Mechanik* **17** (1997), 31–40.
22. Reese, S.; Raible, T. & Wriggers, P.: Finite element modelling of orthotropic material behaviour in pneumatic membranes. *International Journal of Solids and Structures* **38** (2001), 9525–9544.
23. Rice, J. C.; Cowin, S. C. & Bowman, J. A.: On the dependence of elasticity and strength of cancellous bone. *Journal of Biomechanical Engineering* **21** (1988), 155–168.
24. Ricken, T.: *Kapillarität in porösen Medien - theoretische Untersuchung und numerische Simulation*. Dissertation, Shaker-Verlag, Aachen, 2002.
25. Ricken, T. & de Boer, R.: Multiphase flow in a capillary porous medium. *Computational Materials Science* **28**, (2003), 704–713.
26. Ricken, T.; Schwarz, A. & Bluhm, J.: A Triphasic model of transversely isotropic biological tissue with application to stress and biological induced growth. *Computational Materials Science* **39** (2007), 124–136.
27. Schröder, J. & Neff, P.: Invariant formulation of hyperelastic transverse isotropy based on polyconvex free energy functions. *International Journal of Solids and Structures*, **40** (2003), 401–445.
28. Schröder, J.; Neff, P. & Balzani, D.: A variational approach for materially stable anisotropic hyperelasticity., *International Journal of Solids and Structures* **42** (2005), 4352–4371.
29. Spencer, A. J. M.: Theory of invariants. In Eringen, A. C. (ed.): *Continuum Physics Vol. 1*, Academic Press, New York, 1971, pp. 239–353.

30. Taber, L. A.: Biomechanics of growth, remodeling, and morphogenesis. *Applied Mechanics Review* **48** (1995), 487–545.
31. Zheng, Q. S. & Spencer, A. J. M.: On the canonical representations for Kronecker powers of orthogonal tensors with application to material symmetry problems. *International Journal of Engineering Science* **31** (1993), 617–635.
32. Zheng, Q. S. & Spencer, A. J. M.: Tensors which characterize anisotropies., *International Journal of Engineering Science* **31** (1993), 679–693.

On Multiscale Modelling of Perfused Tissues Using Homogenisation of a Strongly Heterogeneous Biot Continuum

E. Rohan, R. Cimrman & V. Lukeš

Department of Mechanics, Faculty of Applied Sciences, University of West Bohemia, Univerzitní 22, 30614 Plzeň, Czech Republic

Abstract. The homogenisation approach is combined with the technique of the dual porosity (the strong heterogeneity in permeability). The resulting limit model of perfusion in deforming tissue involves new constitutive laws whose coefficients can be computed for specific microstructures using local problems and few parameters related to the microstructure. In the paper, we report the essential features of the two-scale modelling and illustrate its performance on a 2D example.

1 Introduction

It is generally accepted that biological tissues can well be approximated using models of porous media saturated with fluids. Many existing models are introduced purely on the phenomenological basis of the theory of porous media or using the theory of mixtures. In these cases, there are many model parameters to be identified from experiments which, however, pertain somewhat cumbersome. Especially in the large deformation problems, when the coefficients depend on the deformation, the “curve fitting” strategy may become ambiguous serving unreliable results in the prospect of the model applicability for predictions.

We claim that many important constraints and relationships between material parameters can hardly be introduced without a more refined description of the microstructure based on its geometrical arrangement. When such option is available, various averaging techniques can be employed to compute the effective structural parameters. Here, we report on the two-scale modelling which, as a prerequisite, requires a well defined (whatever simplified) microstructural geometry and a micromodel describing the medium behaviour for finite scale heterogeneities distributed in the microstructure. The main features of the present modelling approach can be outlined as follows:

- locally periodic microstructure is defined as a lattice represented (locally) by the reference periodic cell (RPC);
- micromodel is based on the Biot continuum describing mixture of incompressible fluid diffusing in the incompressible solid skeleton;

- constitutive parameters comprise stiffness and hydraulic permeability tensors; they vary with the position in the RPC;
- the permeability coefficients are assumed to be strongly heterogeneous: in a subdomain of the RPC, they depend on the scale parameter ε ; this indicates that there is an underlying sub-microstructure;
- two-scale method of homogenisation is applied to upscale the micromodel;
- limit structure of the model involves global (macroscopic) equations and local sub-problems for corrector functions which constitute the homogenised (effective) parameters;
- in nonlinear situations (large deformation), the reference microscopic configuration (geometry and internal parameters) must be updated locally using the macroscopic fields; the parallel strategy was proposed in [8] and further elaborated and discussed in detail in [5].

The aim of the present paper is to demonstrate the multi-scale computing approach applied to blood perfusion in deforming tissue. Our model captures parallel flow in two conducting sectors separated by an interface representing the lowest hierarchy of the vasculature (capillaries). Another application based on the same machinery was developed to mimic large deformation of smooth muscle tissues with microflow of interstitial fluids around the smooth muscle cells; comprehensive studies can be found in recent references [5, 6].

Detailed description of the upscaled model of blood perfusion is beyond the scope of the paper, it will be developed in the forthcoming paper [7]. We shall outline the model equations of the perfusion problem. In particular, we introduce the micromodel, discuss the strong heterogeneity, the resulting local and global equations and explain the meaning of the homogenised coefficients. Then, we illustrate the multi-scale computing tools: for pre-calculated homogenised coefficients, we solve the global problem for the macroscopic displacement and two pressure fields, consequently, at selected points, we can compute the local (microscopic) stresses and strains.

2 Microstructure and Local Characteristic Responses

The heterogeneous medium is generated as the periodic lattice by the reference periodic cell (RPC) Y split into three non-overlapping sectors Y_k , $k = 1, 2, 3$, so that $\bar{Y} = \bar{Y}_1 \cup \bar{Y}_2 \cup \bar{Y}_3$ with interfaces $\Gamma_k = \bar{Y}_k \cap \bar{Y}_3$ for $k = 1, 2$, see Figure 1. The homogenisation procedure is applied to the quasi-static Biot model for incompressible materials (σ_{ij} is the Cauchy stress, $e_{ij}(u)$ is the small strain of displacement field u , p is the bulk pressure, and w is the perfusion/seepage velocity)

$$\begin{aligned} -\operatorname{div} \sigma^\varepsilon &= f, & \sigma_{ij}^\varepsilon &= -p^\varepsilon \delta_{ij} + D_{ijkl}^\varepsilon e_{kl}(u^\varepsilon), \\ \operatorname{div} \frac{d}{dt} u^\varepsilon + \operatorname{div} w^\varepsilon &= 0, & w_i^\varepsilon &= -K_{ij}^\varepsilon \partial_j p^\varepsilon. \end{aligned} \quad (1)$$

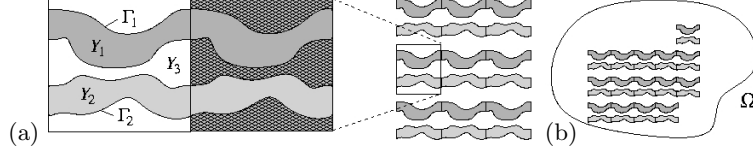


Fig. 1. (a) The reference microstructural cell split into 2 high conductive sectors Y_1 and Y_2 separated by an interface (matrix) sector Y_3 ; $\Gamma_k = \overline{Y_k} \cap \overline{Y_3}$, $k = 1, 2$. (b) The periodic lattice structure of domain Ω .

Above the dependence on the scale of the heterogeneities is indicated by ε . The relationship between the macro- and micro-scale described by coordinates x and y , respectively, is established through $x = \varepsilon y$, see, e. g., [4]. The constitutive parameters varying with position in the microstructure are Y -periodic, cf. [2, 4] (note that $D(y) = D^\varepsilon(x) = D(x/\varepsilon)$ and the same holds for $K(y)$)

$$\begin{aligned} \text{Elasticity: } D_{ijkl}(y) &= \sum_{\alpha=1}^3 \chi_\alpha(y) D_{ijkl}^\alpha, \\ \text{Permeability: } K_{ij}(y) &= \sum_{\alpha=1}^2 \chi_\alpha(y) K_{ij}^\alpha + \varepsilon^2 \chi_3(y) K_{ij}^3, \end{aligned} \quad (2)$$

where $\chi_\alpha(y)$ are the characteristic functions of the subdomains Y_α extended by Y -periodicity to whole \mathbb{R}^3 . Here, the main concern of the homogenisation-based modelling is related to the strong heterogeneity in the permeability coefficients, introduced by virtue of the ε^2 -dependence in $(2)_2$. This scaling is natural, corresponding to lower order scales at which the permeability is obtained by homogenisation of the Stokes flow. The homogenisation procedure is described in detail for a similar model with a simpler type of microstructures in [3].

The effective material tensors involved in the homogenised model depend on the corrector basis functions computed for a given RPC. We employ the bilinear forms (where $f_Z = |Y|^{-1} \int_Z$ for $Z \subset Y$)

$$\begin{aligned} a_Y(\mathbf{u}, \mathbf{v}) &= \int_Y D_{ijkl} e_{kl}^y(\mathbf{u}) e_{ij}^y(\mathbf{v}), \quad c_{Y_3}(\phi, \psi) = \int_{Y_3} K_{ij}^3 \partial_j^y \phi \partial_i^y \psi, \\ (\phi, \psi)_{Y_3} &= \int_{Y_3} \phi \psi, \end{aligned} \quad (3)$$

and use the following spaces: by $\mathbf{H}_{\#}^1(Y)$, we denote the restriction of the Sobolev space $\mathbf{H}^1(Y)$ to the Y -periodic vectorial functions, whereby the analogous notation $H_{\#}^1(Y)$ is used for scalar functions; $H_{\#0}^1(Y_3)$ is the restriction of $H_{\#}^1(Y_3)$ to functions which are zero on interfaces $\Gamma_k = \Gamma_{k,3}$, $k = 1, 2$.

There are the steady and time-dependent correctors:

The steady state correctors $(\bar{\omega}^{rs}, \bar{\pi}^{rs})$ and $(\omega^{*,\alpha}, \tilde{\pi}^\alpha(0))$ are solutions to the following problems:

- Find $\bar{\omega}^{rs} \in \mathbf{H}_{\#}^1(Y)$ and $\bar{\pi}^{rs} \in H_{\#0}^1(Y_3)$, so that

$$\begin{aligned} a_Y(\bar{\omega}^{rs}, \mathbf{v}) &= -a_Y(\mathbf{II}^{rs}, \mathbf{v}) \quad \forall \mathbf{v} \in \mathbf{H}_{\#}^1(Y), \\ c_{Y_3}(\bar{\pi}^{rs}, \psi) &= -(\psi, \operatorname{div}_y \bar{\omega}^{rs} + \operatorname{div}_y \mathbf{II}^{rs})_{Y_3} \quad \forall \psi \in H_{\#0}^1(Y_3), \end{aligned} \quad (4)$$

where $\mathbf{II}_i^{rs} = \delta_{ri} y_s$, so that $\mathbf{II}_i^{rs} e_{rs}^x$ is the displacement induced in Y by locally uniform (macroscopic) strain e_{rs}^x .

- Find $\omega^{*,\alpha} \in \mathbf{H}_{\#}^1(Y)$ and $\tilde{\pi}^\alpha(0) \in H_{\#}^1(Y_3)$, such that

$$\begin{aligned} a_Y(\omega^{*,\alpha}, \mathbf{v}) - (\tilde{\pi}^\alpha(0), \operatorname{div}_y \mathbf{v})_{Y_3} &= \int_{\Gamma_\alpha} \mathbf{v} \cdot \mathbf{n}^{[\alpha]} dS \quad \forall \mathbf{v} \in \mathbf{H}_{\#}^1(Y), \\ (\psi, \operatorname{div}_y \omega^{*,\alpha})_{Y_3} &= 0 \quad \forall \psi \in H_{\#0}^1(Y_3), \end{aligned} \quad (5)$$

where $\tilde{\pi}^\alpha(0) = \delta_{\alpha\beta}$ on Γ_β , $\beta = 1, 2$, and $\mathbf{n}^{[\alpha]}$ is the unit normal outward to Y_α . It holds that $\omega^{*,1} = -\omega^{*,2}$ and $\tilde{\pi}^1(0) = 1 - \tilde{\pi}^2(0)$. Note that $\tilde{\pi}^\alpha(0)$ serves as the Lagrange multiplier of the incompressibility of $\omega^{*,\alpha}$ in Y_3 .

The time-variant correctors satisfy the following subproblems:

- Find $(\tilde{\omega}^{rs}, \tilde{\pi}^{rs}) \in \mathbf{H}_{\#}^1(Y) \times H_{\#0}^1(Y_3)$, such that for $t > 0$

$$\begin{aligned} a_Y(\tilde{\omega}^{rs}(t), \mathbf{v}) - \left(\frac{d}{dt} \tilde{\pi}^{rs}(t), \operatorname{div}_y \mathbf{v} \right)_{Y_3} &= 0 \quad \forall \mathbf{v} \in \mathbf{H}_{\#}^1(Y), \\ (\psi, \operatorname{div}_y \tilde{\omega}^{rs}(t))_{Y_3} + c_{Y_3}(\tilde{\pi}^{rs}(t), \psi) &= 0 \quad \forall \psi \in H_{\#0}^1(Y_3), \end{aligned} \quad (6)$$

with the initial condition $\tilde{\pi}^{rs}(0) = -\bar{\pi}^{rs}$.

- Find $(\tilde{\omega}^\alpha, \tilde{\pi}^\alpha) \in \mathbf{H}_{\#}^1(Y) \times H_{\#}^1(Y_3)$, such that for $t > 0$

$$\begin{aligned} a_Y(\tilde{\omega}^\alpha(t), \mathbf{v}) - \left(\frac{d}{dt} \tilde{\pi}^\alpha(t), \operatorname{div}_y \mathbf{v} \right)_{Y_3} &= 0 \quad \forall \mathbf{v} \in \mathbf{H}_{\#}^1(Y), \\ (\psi, \operatorname{div}_y \tilde{\omega}^\alpha(t))_{Y_3} + c_{Y_3}(\tilde{\pi}^\alpha(t), \psi) &= 0 \quad \forall \psi \in H_{\#0}^1(Y_3), \\ \text{where } \tilde{\pi}^\alpha &= \delta_{\alpha\beta} \text{ on } \Gamma_\beta, \beta = 1, 2, \end{aligned} \quad (7)$$

with the initial condition $\tilde{\pi}^\alpha(0) \neq 0$ already computed in (5).

3 Homogenised Parallel Diffusion in a Deforming Medium

The macromodel involves the homogenised coefficients (presented in Section 3.1) and is defined in terms of the macroscopic displacements, $\mathbf{u}(t) \in \mathbf{V} \subset \mathbf{H}^1(\Omega)$, and the two macroscopic pressures, $p_1(t), p_2(t) \in H_0^1(\Omega)$; these satisfy the equilibrium equation

$$\begin{aligned} & \int_{\Omega} \left[\mathcal{E}_{ijkl} e_{kl}^x(\mathbf{u}(t)) + \bar{\mathcal{B}}_{ijkl} \frac{d}{dt} e_{kl}^x(\mathbf{u}(t)) \right. \\ & \quad \left. + \int_0^t \mathcal{H}_{ijkl}(t-\tau) \frac{d}{d\tau} e_{kl}^x(\mathbf{u}(\tau)) d\tau \right] e_{ij}^x(\mathbf{v}) \\ & - \int_{\Omega} e_{ij}^x(\mathbf{v}) \int_0^t \tilde{\mathcal{R}}_{ij}^1(t-\tau) [p_1(\tau) - p_2(\tau)] d\tau \\ & - \sum_{\alpha=1,2} \int_{\Omega} \left[\frac{|Y_{\alpha}|}{|Y|} \delta_{ij} + \bar{\mathcal{P}}_{ij}^{\alpha} \right] p_{\alpha}(t) e_{ij}^x(\mathbf{v}) = L(\mathbf{v}) \quad \forall \mathbf{v} \in \mathbf{V}_0, \end{aligned} \quad (8)$$

(where \mathbf{V}_0 is the space of the test displacements and $L(\cdot)$ is the load functional) and the two balance-of-mass equations for $\alpha, \beta = 1, 2, \beta \neq \alpha$

$$\begin{aligned} & \int_{\Omega} \mathcal{C}_{ij}^{\alpha} \partial_j^x p_{\alpha}(t) \partial_i^x q + \int_{\Omega} q \mathcal{G}^* \frac{d}{dt} (p_{\alpha}(t) - p_{\beta}(t)) \\ & + \int_{\Omega} q \int_0^t \tilde{\mathcal{G}}_+(t-\tau) \frac{d}{d\tau} (p_{\alpha}(\tau) - p_{\beta}(\tau)) d\tau \\ & + \int_{\Omega} q \int_0^t \frac{d}{dt} \tilde{\mathcal{Q}}_{ij}^{\alpha}(t-\tau) \frac{d}{d\tau} e_{ij}^x(\mathbf{u}(\tau)) d\tau \\ & + \int_{\Omega} q \left[\frac{|Y_{\alpha}|}{|Y|} \delta_{ij} + \hat{\mathcal{Q}}_{ij}^{\alpha}(0_+) \right] \frac{d}{dt} e_{ij}^x(\mathbf{u}(t)) = 0, \quad \forall q \in H_0^1(\Omega), \end{aligned} \quad (9)$$

which govern the fluid flow in the two channels and its redistribution between them.

Due to the relationship between homogenised coefficients (HCs) and the structures of the corrector problems, we may better understand the mechanical interpretation of the HCs – they represent integral figures of the microscopic responses for special load regimes.

3.1 Homogenised Coefficients

We list the expressions for computing the HCs using the corrector solutions defined in (4)–(7). The homogenised permeabilities $\mathcal{C}_{ij}^{\alpha}$ are computed for each compartment Y_{α} independently using the standard homogenisation result, cf. [3] or the general references [2, 4].

Homogenised elasticity and viscoelasticity coefficients:

- Elasticity $\mathcal{E}_{ijkl} = a_Y (\mathbf{\Pi}^{kl} + \bar{\omega}^{kl}, \mathbf{\Pi}^{ij} + \bar{\omega}^{ij})$,
- Viscosity, instantaneous effects $\bar{\mathcal{B}}_{ijkl} = \frac{1}{2} c_{Y_3} (\bar{\pi}^{kl}, \bar{\pi}^{ij})$,
- Viscosity, fading memory effects $\mathcal{H}_{ijkl}(t) = c_{Y_3} \left(\frac{d}{dt} \tilde{\pi}^{kl}(t), \bar{\pi}^{ij} \right)$.

Biot-type coefficients: stress induced by non-equilibrated pressure $p_1 - p_2$, see (11),

$$\text{instantaneous: } \bar{\mathcal{P}}_{ij}^\alpha = \left[(\bar{\pi}^\alpha(0), \delta_{ij})_{Y_3} - a_Y (\boldsymbol{\omega}^{*,\alpha}, \mathbf{II}^{ij}) \right],$$

$$\text{fading memory: } \tilde{\mathcal{R}}_{ij}^\alpha(t) = \left[\left(\frac{d}{dt} \tilde{\pi}^\alpha(t), \delta_{ij} \right)_{Y_3} - a_Y (\tilde{\omega}^\alpha(t), \mathbf{II}^{ij}) \right], \quad \alpha = 1, 2.$$

Biot-type coefficients: deformation induced volume change of channels by net fluid exchange through (fixed) interface Γ_α ($\tilde{\mathbf{w}}$ is the perfusion velocity)

$$\tilde{\mathcal{Q}}_{ij}^\alpha(t) = \int_{\Gamma_\alpha} (\tilde{\omega}^{ij}(t) + \tilde{\mathbf{w}}^{ij}(t)) \cdot \mathbf{n}^{[\alpha]} dS$$

and by ‘‘impermeable-like’’ interface Γ_α (interface distension mode)

$$\hat{\mathcal{Q}}_{ij}^\alpha(0_+) = \int_{\Gamma_\alpha} (\tilde{\omega}^{ij}(0_+) + \bar{\omega}^{ij}) \cdot \mathbf{n}^{[\alpha]} dS.$$

Barenblatt coefficients: related to the flow between the two channels and induced by $p_\alpha - p_\beta$, $\beta \neq \alpha$. They describe following phenomena: net fluid exchange through rigid-fixed interface ($\tilde{\mathbf{w}}$ is the perfusion velocity)

$$\tilde{\mathcal{G}}(t) = \int_{\Gamma_1} (\tilde{\omega}^1(t) + \tilde{\mathbf{w}}^1(t)) \cdot \mathbf{n}^{[1]} dS$$

and effects of the incompressible interface sector, the change of proportion between volumes of the channels Y_1 and Y_2 due to the compliant, incompressible interface Y_3

$$\mathcal{G}^* = \int_{\Gamma_1} \boldsymbol{\omega}^{*,1} \cdot \mathbf{n}^{[1]} dS.$$

It is worth noting that there are symmetries between those terms in equations (8)–(9) which couple the diffusion and deformation effects. It holds

$$\bar{\mathcal{P}}_{ij}^\alpha = \hat{\mathcal{Q}}_{ij}^\alpha \quad \text{and} \quad \tilde{\mathcal{R}}_{ij}^\alpha(t) = \frac{d}{dt} \tilde{\mathcal{Q}}_{ij}^\alpha(t), \quad \alpha = 1, 2. \quad (10)$$

Furthermore, we have the following relationships between the corresponding coefficients associated with Y_1 and Y_2 :

$$\begin{aligned}\bar{p}_{ij}^1 + \bar{p}_{ij}^2 &= \frac{|Y_3|}{|Y|} \delta_{ij}, & \hat{Q}_{ij}^1 + \hat{Q}_{ij}^2 &= \frac{|Y_3|}{|Y|} \delta_{ij}, \\ \tilde{\mathcal{R}}_{ij}^1(t) + \tilde{\mathcal{R}}_{ij}^2(t) &= 0, & \frac{d}{dt}[\tilde{Q}_{ij}^1(t) + \tilde{Q}_{ij}^2(t)] &= 0.\end{aligned}\quad (11)$$

3.2 Recovery of Pressure, Stress, and Deformation at the Micro-Level

The two-scale modelling enables to interpret the macroscopic fields in terms of the detailed local distributions of the microscopic fields. Having computed the displacement and pressure distributions in Ω , the microscopic ones can be recovered for a given $x \in \Omega$ using the ‘‘characteristic microscopic responses’’. For a given local strain $e_{ij}^x(\mathbf{u}(x, t))$, pressures $p_\alpha(x, t)$ and their gradients $\partial_k^x p_\alpha$ at an arbitrary macroscopic point x and in time interval $[0, t_{\max}]$, we can compute the following corrector microscopic fields:

$$\begin{aligned}\mathbf{u}^{\text{corr}}(y, t) &= \sum_{ij} \left[\bar{\omega}^{ij} e_{ij}^x(\mathbf{u}(t)) + \int_0^t \tilde{\omega}^{ij}(t-s) \frac{d}{ds} e_{ij}^x(\mathbf{u}(s)) ds \right] \\ &\quad + \sum_{\alpha=1,2} \left[\omega^{*,\alpha} p_\alpha(t) + \int_0^t \tilde{\omega}^\alpha(t-s) p_\alpha(s) ds \right], \quad y \in Y, \\ p_3^{\text{corr}}(y, t) &= \sum_{ij} \int_0^t \frac{d}{dt} \tilde{\pi}^{ij}(t-s) \frac{d}{ds} e_{ij}^x(\mathbf{u}(s)) ds \\ &\quad + \sum_{\alpha=1,2} \left[\tilde{\pi}^\alpha(0) p_\alpha(t) + \int_0^t \frac{d}{dt} \tilde{\pi}^\alpha(t-s) p_\alpha(s) ds \right], \quad y \in Y_3.\end{aligned}\quad (12)$$

Using (12) the relevant microscopic fields can be recovered:

- Displacement $\mathbf{u}^{\text{mic}} = (u_i^{\text{mic}})$: In the limit situation ($\varepsilon \rightarrow 0$), construction (13) provides displacements relative to a fixed point:

$$u_i^{\text{mic}}(y, t) = e_{ij}^x(\mathbf{u}(t)) y_j + u_i^{\text{corr}}(y, t), \quad y \in Y, \quad (13)$$

- Pressure p^{mic} : In the limit situation the pressure field is constant w. r. t. $y \in Y_\alpha$, whereas it varies in Y_3 :

$$\begin{aligned}p^{\text{mic}}(y, t) &= p_3^{\text{corr}}(y, t), \quad y \in Y_3, \\ p^{\text{mic}}(y, t) &= p_\alpha(t), \quad y \in Y_\alpha, \quad \alpha = 1, 2.\end{aligned}\quad (14)$$

- Diffusion velocity $\mathbf{w}^{\text{mic}} = (w_i^{\text{mic}})$: Denoting by P_α^k the standard corrector function which constitutes the homogenised permeability \mathcal{C}_{ij}^α in (9), we have

$$\begin{aligned}w_i^{\text{mic}}(y, t) &= K_{ij}^3 \partial_j^y p_3^{\text{corr}}(y, t), \quad y \in Y_3, \\ w_i^{\text{mic}}(y, t) &= K_{ij}^\alpha \partial_j^y (P_\alpha^k(y) + y_k) [\partial_k^x p_\alpha](t), \quad y \in Y_\alpha.\end{aligned}\quad (15)$$

4 Numerical Example – 2D Structure

We report a numerical example of the two-scale blood perfusion simulation. The upscaled problem (8)–(9) is defined in a square domain Ω . Pressures $\bar{p}_1(t)$, $\bar{p}_2(t)$ are prescribed as varying in time on two opposite edges of Ω , whereas the non-penetration condition is imposed on the other two edges. The structure is loaded on the upper edge by tractions and fixed on its lower edge. In Figure 2, we illustrate the distribution of p_1 , p_2 and of $p_2 - p_1$ in Ω . At a selected point $\mathbf{X} \in \Omega$, the N_t time samples were recorded, see Figure 3, comprising the following arrays:

record	phys. meaning	array dim.
$\{e_{11}(\mathbf{u}(t)), e_{22}(\mathbf{u}(t)), 2e_{12}(\mathbf{u}(t))\}_t$	strain	$[3 \times N_t]$
$\{p_1(t), p_2(t)\}_t$	pressure	$[2 \times N_t]$
$\{\nabla p_1(t), \nabla p_2(t)\}_t$	pressure grad.	$[4 \times N_t]$

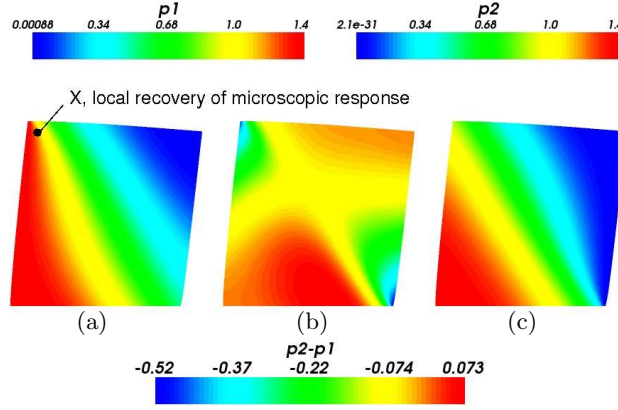


Fig. 2. Pressures p_1 (a), p_2 (c) and difference $p_2 - p_1$ (b) at the last time step.

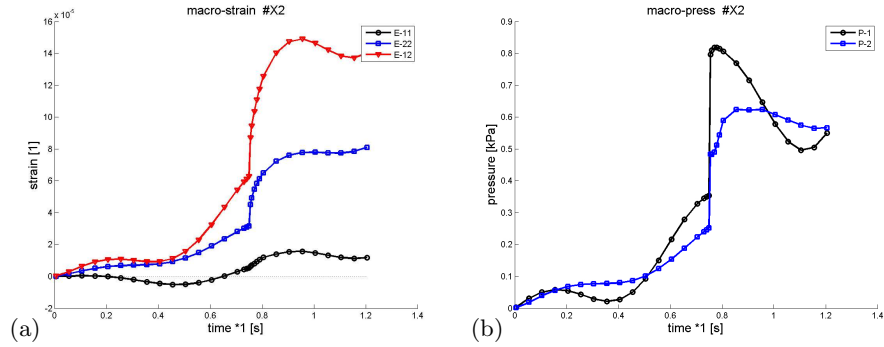


Fig. 3. Macroscopic response at a selected point $\mathbf{X} \in \Omega$: (a) strains $e_{ij}(\mathbf{u}(t))$ and (b) pressures $p_1(t)$, $p_2(t)$.

The resulting microscopic response was post-processed using convolutions (12) for a selected point $\hat{y} \in Y$. The effective stresses (i. e., $\sigma_{ij}^{\text{eff}} = D_{ijkl}e_{kl}(\mathbf{u}^{\text{mic}})$ without the volumetric part) and perfusion velocities are displayed in Figure 4. In Figure 5, we illustrate the pressure and the von Mises stress distributed in the domain Y at selected time levels.

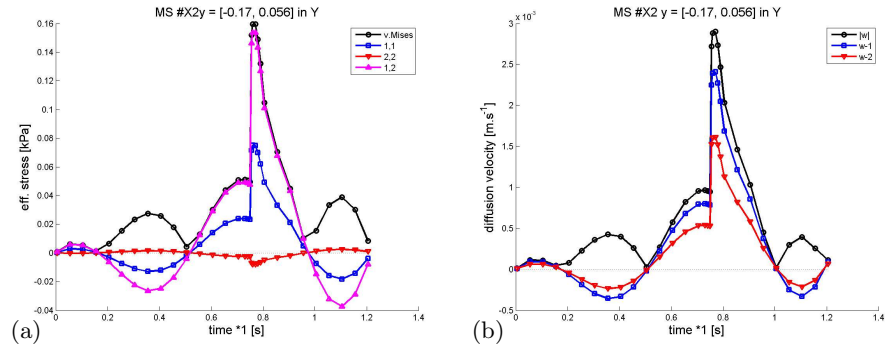


Fig. 4. Microscopic response at given $\hat{y} \in Y$: (a) stress and (b) diffusion velocity.

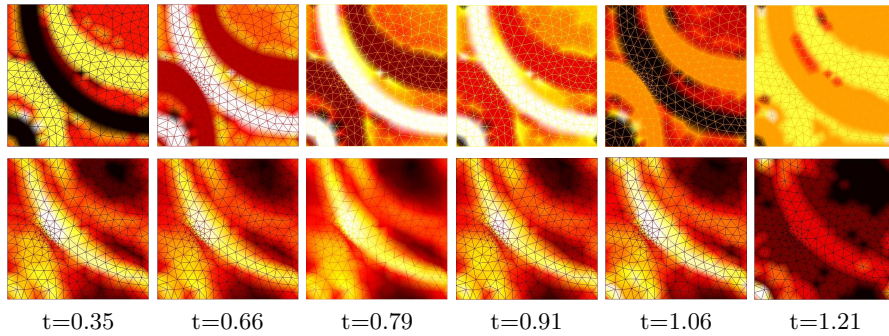


Fig. 5. Microscopic pressure and stress recovery. Above: pressure distribution in Y at time levels 8/14/23/26/29/32; below: von Mises stress at respective time levels.

5 Conclusion

In summary, we have demonstrated some interesting features of the homogenisation and two-scale modelling that may contribute to the development of advanced models of biological tissues. Starting with the Biot model, the dual porosity (strong heterogeneity in the permeability coefficients) related to a convenient partitioning of the reference volume element, the RPC, led to a new homogenised form of the constitutive laws, involving memory

effects, different forms of permeabilities that govern parallel flows in two channels and the flux between them, which is the measure of the tissue perfusion. The stress and strain recovery at the microscopic level from the macroscopic response can be used as basis for modelling growth and damage. The model can be extended to account for convected diffusion of dissolved species, e. g., oxygen.

The homogenised forms of the constitutive laws reported here have also been adapted and employed for the ad hoc macroscopic modelling of large deforming tissues in [1].

Acknowledgment

The research is supported by the project MSM 4977751303 of the Czech Republic.

References

1. Cimrman, R. & Rohan, E.: On modelling the parallel diffusion flow in deforming porous media. *Mathematics and Computers in Simulation* (to appear 2007), special volume: Proceedings of the Conference *Modelling 2005 – Third IMACS Conference on Mathematical Modelling and Computational Methods*, Plzeň, 2005.
2. Cioranescu, D. & Donato, P.: *An Introduction to Homogenization, Oxford Lecture Series in Mathematics and its Applications 17*. Oxford University Press, Oxford, 1999.
3. Griso, G. & Rohan, E.: On homogenization of diffusion-deformation problem in strongly heterogeneous media. *Ricerche di Matematica* (accepted 2006).
4. Hornung, U.: *Homogenization and Porous Media*. Springer-Verlag, Berlin, 1997.
5. Lukeš, V.: *Two-scale computational modelling of soft biological tissues*. Ph. D. thesis, University of West Bohemia, Plzeň, 2007.
6. Rohan, E.: Modelling large deformation induced microflow in soft biological tissues. *Theoretical and Computational Fluid Dynamics* **20** (2006), 251–276.
7. Rohan, E.: Homogenization of perfusion problem in deforming tissue with dual porosity. (to be submitted 2007).
8. Rohan, E.; Cimrman, R. & Lukeš, V.: Numerical modelling and homogenized constitutive law of large deforming fluid saturated heterogeneous solids. *Computers & Structures* **84** (2006), 1095–1114.

Calculation of Muscle and Joint Forces in the Masticatory System

S. Rues, H. J. Schindler, J. Lenz & K. Schweizerhof

Research Group Biomechanics, University of Karlsruhe
Englerstraße 2, 76128 Karlsruhe, Germany

Abstract. In ten healthy test persons, electromyographic (EMG) activities of the essential masticatory muscles and the intraorally transferred, feedback-controlled resultant bite force have been measured simultaneously for 19 motor tasks at different magnitudes simulating clenching. Additionally, for all test persons 3d-models of the musculature were reconstructed from magnetic resonance tomograms. The aim of the study was to identify the associated activation patterns, the intrinsic muscle strength and the muscle forces using a non-linear force law, and to calculate the joint reaction forces. On the basis of this information, motor tasks leading to high joint forces may possibly be identified. However, for the calculation of joint forces the lines of action of the masticatory muscles and the magnitudes of the muscle forces are needed. In this contribution the lines of action are determined by two different schemes: In the first approach the lines of action are defined by the centroids of the muscles' origin and insertion areas, and the muscle force magnitudes are computed based on the physiological cross-sectional areas. In a second approach all quantities shall be computed with the help of specific finite elements which are presently under development.

1 Introduction

The human masticatory system consists of twelve essential muscles connecting the mandible with the maxilla. Each muscle can generate a force vector with an a priori unknown magnitude, but along a line of action which can approximately be constructed either from its geometry or with the help of a finite element (FE) analysis. For the joint forces, however, the magnitudes as well as the lines of action are unknown. If we assume the mandible to be a rigid body there are 12 muscle forces + 6 joint force components in comparison to 6 equilibrium equations. Therefore, the system is highly redundant, i. e., without further information a specific resultant force can be generated by an infinite variety of activation patterns. Thus, aside of certain optimization methods using arbitrarily chosen target functions, only a simultaneous measurement of all muscular EMG activities and the resultant bite force between the lower and upper jaw can reveal the actual situation.

It is obvious that the quality of the results depends essentially on the quality of the estimation of the lines of action. Here, a FE analysis will certainly deliver better results than the geometric approach because the structure of each muscle and a possible inhomogeneous activation can be taken into account.

2 Materials and Methods

2.1 EMG- and Bite Force Measurement

To date, no measured data are available from experiments in which the activities of all masticatory muscles and the resultant bite force have been recorded simultaneously. This complete knowledge is, however, indispensable to determine the direction and magnitude of the reaction forces transferred to the condyles.

For that purpose, in ten healthy male subjects (average age: 29 ± 2.6 years) the intraoral force transfer and the electromyographic activities of the masseter, anterior and posterior temporal, medial and lateral pterygoid, and anterior digastric were simultaneously recorded in simulated clenching tasks during the generation of various resultant bite force vectors F_{res} . A feedback system enabled the test persons to perform 19 specific clenching tasks (circumferential angle $\varphi = 0^\circ, 60^\circ, 90^\circ, 180^\circ, 270^\circ, 300^\circ$; cranial angle $\theta = 0^\circ, 20^\circ, 40^\circ, 60^\circ$ with respect to the normal z' on the occlusal plane; cf. Figure 1 (a)) at different magnitudes of the resultant force. The centrally transmitted resultant force was determined with an intraoral measuring appliance, consisting of a bearing pin device equipped with strain gauges and fixed on custom-made metal splints (Figure 1 (b)).

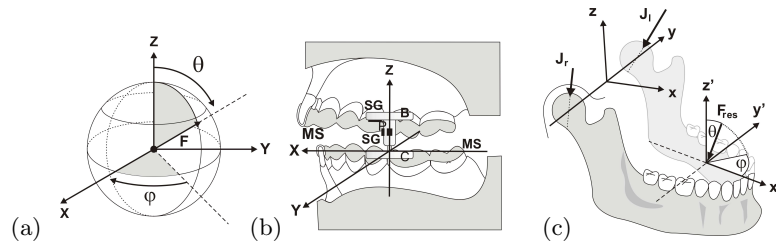


Fig. 1. Coordinate system used for the force measurement device (x',y' -plane corresponds to the occlusal plane) with angles φ and θ (a), Intraoral measuring device: SG: strain gauge, P: pin, B: base plate, C: contact plate, MS: metal splint (b) and Mandible with bite force and joint forces (c) (muscle forces are not displayed).

Bipolar surface electrodes were employed to measure bilaterally the electric activities U_i of the masseter, anterior temporal, posterior temporal, and anterior digastric, whereas bilateral bipolar wire electrodes, inserted by a needle, recorded the electric muscle activity of the medial and lateral pterygoid muscles. For special motor tasks also the maximum electric activities $U_{\text{max},i}$ of all muscles were determined. The experimental details are described in [1]. The study was approved by the Ethics Committee of the University of Freiburg, Germany (No. 25/02). All participating subjects gave their written consent to the experiments which were conducted in accordance with the Declaration of Helsinki.

2.2 Force Law

In addition, for each test person a 3d-model of the musculature was constructed using horizontal and frontal magnetic resonance tomograms (MRT) which also served to identify the so-called Frankfurt horizontal plane (passing through the lowest point in the margin of the orbit and the highest point in the margin of the auditory meatus), the occlusal plane, and the position of the bearing pin. From these models the so-called physiological cross-sectional areas $A_i = (1-p_i)V_i/l_{f,i}$ (V_i : total muscle volume, p_i : portion of tendinous tissue, $l_{f,i}$: muscle fibre length) were calculated (cf. Figure 2 (a)). The values for V_i and $l_{f,i}$ were taken from [2]. All described motor tasks were performed with magnitudes $F_{\text{res}} = 50$ N and $F_{\text{res}} = 150$ N. The task with vertical resultant force was additionally performed with $F_{\text{res}} = 250$ N and under maximum voluntary bite force of each test person. The results of this experimental study were presented in detail in [5]. The correlation between the actual muscle force and the actual electric activation is given by the force law:

$$\frac{F_i}{F_{\text{max},i}} = f\left(\frac{U_i}{U_{\text{max},i}}\right) = c_1 \frac{U_i}{U_{\text{max},i}} + c_2 \left(\frac{U_i}{U_{\text{max},i}}\right)^2. \quad (1)$$

Using the measured data, the constants c_1 and c_2 were determined for each test person separately via a least squares fit. A typical result for one test person can be seen in Figure 2 (b). The muscle force is proportional to its physiological cross-section (= sum of all muscle fibre cross-sections) and the stress generated by the muscle fibres [7]. The maximum stress value a muscle may generate is given by the so-called intrinsic muscle strength P . For pennated muscles (angle α_i between line of action and fibre direction) the maximum muscle force is given by $F_{\text{max},i} = P \cdot A_i \cdot \cos \alpha_i$.

2.3 Rigid Body Model

The line of action of each muscle is defined as the connection between the centroids of its origin and insertion area. In the following, the x,y-plane is chosen parallel to the Frankfurt horizontal plane with the y-axis coinciding with the axis connecting the centers of the condyles, and the x-axis directed frontally in the midsagittal plane, cf. right of Figure 1. With the force law relating the muscle forces F_i to the electric activities U_i , and the assumptions that (1) each joint force intersects the center of the corresponding condyle and (2) the component in direction of the condyle axis can only be transmitted by compression, the intrinsic muscle strength P and the joint forces can be determined using the balance of momentum. Once P is determined, all muscle forces follow from the force law together with the measured data.

2.4 Finite Element Formulations

Most chewing muscles have a complex structure, i. e., they are pennated. The muscle fibres attach to aponeuroses (cf. Figure 3) which collect the stress gen-

erated by the contraction of the single fibres. Therefore, to perform a realistic FE simulation, it is necessary to divide the complete muscle into contractile (muscle fibres) and tendinous tissue (aponeuroses). Both tissues consist of a soft but approximately incompressible matrix material to which fibres are added. For both tissues the matrix is modelled as a Mooney-Rivlin material. In the following, the additional contribution of the fibres is presented and implemented.

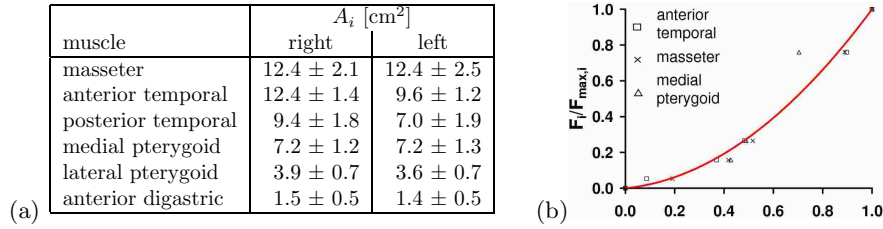


Fig. 2. Physiological cross-sections A_i averaged over the 10 test persons (a) and force law, approximation with a second order polynomial (b).

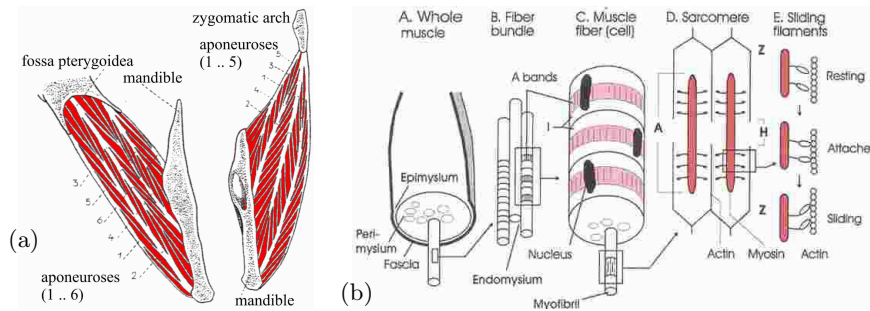


Fig. 3. Morphology of pt. med. and masseter (a) [6] and Muscle physiology (b).

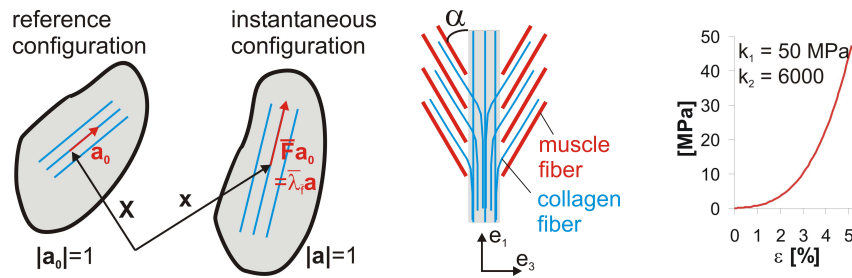


Fig. 4. Modelling and characteristics of the aponeuroses (tendinous tissue).

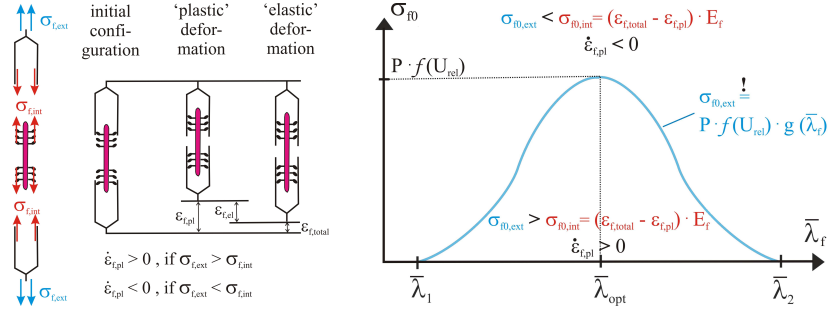


Fig. 5. Modelling and characteristics of muscle fibre contraction.

Finite Tendon Element: For a correct numerical implementation it is necessary to perform the well-known volumetric split of the deformation gradient which results in

$$\begin{aligned} \mathbf{F} &= (J^{1/3} \mathbf{I}) \bar{\mathbf{F}} \quad \text{with } J = \det \mathbf{F}, \\ \mathbf{C} &= \mathbf{F}^T \mathbf{F} = J^{2/3} \bar{\mathbf{F}}^T \bar{\mathbf{F}} = J^{2/3} \bar{\mathbf{C}}. \end{aligned} \quad (2)$$

$$\text{with } \begin{cases} \bar{\mathbf{F}} : \text{modified deformation gradient} \\ \bar{\mathbf{C}} : \text{mod. right Cauchy-Green tensor} \end{cases}$$

The free energy function for the tendinous tissue is divided into a penalty part for the dilatation and parts due to the isochoric deformation ($\bar{\mathbf{C}}$) of the matrix and fibres. Whereas the matrix material behaves isotropic, the behaviour of the fibre depends additionally on a structure tensor \mathbf{A} which takes into account the fibre distribution.

	penalty part for dilatation	matrix material (Mooney-Rivlin)	additional part for collagen fibres
$\Psi(\mathbf{C}, \mathbf{A})$	$= U(J)$	$+ \bar{\Psi}_m(\bar{\mathbf{C}})$	$+ \bar{\Psi}_f(\bar{\mathbf{C}}, \mathbf{A})$
\mathbf{S}	$= \mathbf{S}_{\text{vol}}$	$+ \mathbf{S}_m$	$+ \mathbf{S}_f$
\mathbf{C}	$= \mathbf{C}_{\text{vol}}$	$+ \mathbf{C}_m$	$+ \mathbf{C}_f$

Differentiation of the free-energy function with respect to the right Cauchy-Green tensor yields the 2. Piola-Kirchhoff stress tensor and the material tensor. In the following, we concentrate solely on the new contributions originating from the fibres. For the 2. Piola-Kirchhoff stresses this part is given by $\bar{\mathbf{S}}_f = 2\partial\bar{\Psi}_f/\partial\bar{\mathbf{C}}$.

Using the fourth order projection tensor \mathbb{P} the differentiation with respect to the right Cauchy-Green tensor can be replaced by the differentiation with respect to the modified right Cauchy-Green tensor [3]

$$\bar{\mathbf{S}}_f = J^{-2/3} \mathbb{P} : (2\partial\bar{\Psi}_f/\partial\bar{\mathbf{C}}) = J^{-2/3} \mathbb{P} : \bar{\mathbf{S}}_{f,\text{iso}} \quad (3)$$

$$\text{with } \mathbb{P} = \mathbb{I} - \frac{1}{3} \mathbf{C}^{-1} \otimes \mathbf{C} \quad \text{and} \quad \mathbb{I} = \frac{\delta_{IK} \delta_{JL} + \delta_{IL} \delta_{JK}}{2}$$

For the further procedure it is essential that no energy function for the fibres is introduced explicitly, but rather the contribution $\bar{\mathbf{S}}_{f,iso}$ of the fibres to the 2. Piola-Kirchhoff stress tensor due to an isometric deformation is derived. Looking at the deformed configuration, the Cauchy stress of each fibre depends on the fibre stretch $\bar{\lambda}$ and is, of course, oriented in the direction \mathbf{a} of the fibre (cf. Figure 4). The 2. Piola-Kirchhoff stress tensor is then gained by a pull-back operation

$$\begin{aligned}\bar{\boldsymbol{\sigma}}_f &= \sigma(\bar{\lambda}) \mathbf{a} \otimes \mathbf{a}, \\ \bar{\mathbf{S}}_f &= \frac{1}{\lambda^2} \sigma(\bar{\lambda}) \mathbf{a}_0 \otimes \mathbf{a}_0 \quad \text{with} \quad \lambda^2 = |\bar{\mathbf{F}} \mathbf{a}_0|^2 = \bar{C}_{ij} a_0^i a_0^j.\end{aligned}\quad (4)$$

As suggested by Gasser et al. [3], a density function $\rho(\varphi, \theta)$ is introduced to take into account the spatial distribution of the collagen fibres. The stress tensor is now gained by the summation of the stress tensors for all directions (unit sphere) weighed with the density function

$$\begin{aligned}\bar{\mathbf{S}}_{f,iso} &= \frac{1}{4\pi} \int_{\varphi=0}^{2\pi} \int_{\theta=0}^{\pi} \rho \frac{1}{\lambda^2} \sigma(\bar{\lambda}) \mathbf{e} \otimes \mathbf{e} \sin \theta \, d\theta d\varphi, \\ \text{where} \quad \mathbf{e} &= \begin{pmatrix} \sin \theta \cos \varphi \\ \sin \theta \sin \varphi \\ \cos \theta \end{pmatrix}.\end{aligned}\quad (5)$$

The integral of the density function over the unit sphere has to be zero, i. e., the following normalization condition has to be fulfilled

$$\frac{1}{4\pi} \int_{\varphi=0}^{2\pi} \int_{\theta=0}^{\pi} \rho(\varphi, \theta) \sin \theta \, d\theta d\varphi = 1. \quad (6)$$

As can be seen in the scheme given in Figure 4, the muscle fibres (pennation angle α) are attached to the aponeurosis by collagen fibres. Therefore, it is assumed that all fibres lie in the interval $\frac{\pi}{2} - \alpha \leq \theta \leq \frac{\pi}{2} + \alpha$ and are distributed uniformly with respect to θ . The in-plane fibre distribution $\rho(\varphi)$ of the aponeurosis has to be a π -periodic function. Therefore, the density function (N follows from the normalization equation) is chosen as

$$\begin{aligned}\rho(\varphi, \theta) &= \begin{cases} \rho(\varphi) = \frac{A_0}{N} + \sum_{i=1}^n \frac{A_i}{N} \cos^{2m_i}(\varphi - \varphi_{0,i}) & \text{for } \theta \in [\frac{\pi}{2} - \alpha, \frac{\pi}{2} + \alpha], \\ 0 & \text{else,} \end{cases} \\ \text{with} \quad \begin{cases} N = \sin \alpha \left(A_0 + \sum_{i=1}^n A_i \prod_{j=1}^{m_i} \frac{2(m_i - j) + 1}{2j} \right), \\ m_i \in \{1, 2, 3, \dots\}. \end{cases}\end{aligned}\quad (7)$$

Collagen fibres show a quickly increasing stiffness upon elongation. At first, the curled fibres will be stretched and oriented in load direction with a small

force. At the end, the fibres are straight and in parallel, and nearly no further elongation can be achieved even by high forces. This behavior can be well approximated by an exponential function. Here, because a polynomial is of advantage later on, the first two elements of a series expansion are used

$$\begin{aligned}\sigma(\bar{\lambda}) &= k_1 \bar{\lambda}^2 (\varepsilon + k_2 \varepsilon^3) = k_1 \bar{\lambda}^2 \left[\frac{1}{2}(\bar{\lambda}^2 - 1) + k_2 \left(\frac{1}{2}(\bar{\lambda}^2 - 1) \right)^3 \right] \\ &= \bar{\lambda}^2 k_1 \left[k_2 \bar{\lambda}^6 - 3 k_2 \bar{\lambda}^4 (3 k_2 + 4) \bar{\lambda}^2 - (k_2 + 4) \right] / 8\end{aligned}\quad (8)$$

with $\begin{cases} \bar{\lambda}^2 = \bar{C}_{KL} e_K e_L, & \bar{\lambda}^4 = \bar{C}_{KL} \bar{C}_{MN} e_K e_L e_M e_N, \\ \bar{\lambda}^6 = \bar{C}_{KL} \bar{C}_{MN} \bar{C}_{OP} e_K e_L e_M e_N e_O e_P. \end{cases}$

A typical stress-strain-curve is depicted in Figure 4.

Like in [3] the material tensor for the isochoric contribution is defined as

$$\begin{aligned}\bar{C}_f &= \mathbb{P} : \bar{C}_{f,iso} : \mathbb{P}^T + \frac{2}{3} J^{-2/3} \text{tr}[\bar{\mathbf{S}}_{f,iso}] \bar{\mathbb{P}} - \frac{2}{3} (\mathbf{C}^{-1} \otimes \bar{\mathbf{S}}_f + \bar{\mathbf{S}}_f \otimes \mathbf{C}^{-1}) \\ &\text{with } \begin{cases} \bar{\mathbb{P}} = \mathbb{I}_{c^{-1}} - \frac{1}{3} \mathbf{C}^{-1} \otimes \mathbf{C}^{-1}, \\ [\mathbb{I}_{c^{-1}}]_{IJKL} = \frac{1}{2} (C_{IK}^{-1} C_{JL}^{-1} + C_{IL}^{-1} C_{JK}^{-1}). \end{cases}\end{aligned}\quad (9)$$

To take into account that fibre support exists only for fibre elongation, a function $h(\bar{\lambda})$ is introduced which is 1 for fibre elongation and 0 for fibre shortening. Therefore, the range of values for φ and θ (due to symmetry only half of the unit sphere has to be evaluated) is divided in t_1 and t_2 parts, respectively.

$$h\left(\bar{\lambda}\left(\frac{\varphi_r + \varphi_{r+1}}{2}, \frac{\theta_s + \theta_{s+1}}{2}\right)\right) = \begin{cases} 1 & \text{for } \bar{\lambda}\left(\frac{\varphi_r + \varphi_{r+1}}{2}, \frac{\theta_s + \theta_{s+1}}{2}\right) \geq 1, \\ 0 & \text{for } \bar{\lambda}\left(\frac{\varphi_r + \varphi_{r+1}}{2}, \frac{\theta_s + \theta_{s+1}}{2}\right) < 1, \end{cases}\quad (10)$$

with $\begin{cases} \varphi_r = \frac{2\pi}{t_1}(r-1) & , r = 1, 2, \dots, t_1, \\ \theta_s = \frac{\pi}{2} - \alpha + \frac{\alpha}{t_2}(s-1) & , s = 1, 2, \dots, t_2. \end{cases}$

Finally, for $\bar{C}_{f,iso}$ the expression given below is gained. The integrals depend only on the structure, and primitives can be found and implemented in an FE code.

$$\begin{aligned}[\bar{C}_{f,iso}]_{IJKL} &= 2 \frac{\partial [\bar{\mathbf{S}}_{f,iso}]_{IJ}}{\partial \bar{C}_{KL}} = \\ &= \frac{k_1}{8\pi} \sum_{r=1}^{t_1} \sum_{s=1}^{t_2} h(\bar{\lambda}) \cdot \left\{ (3k_2 + 4) \int_{\varphi=\varphi_r}^{\varphi_{r+1}} \int_{\theta=\theta_s}^{\theta_{s+1}} \rho(\varphi) e_I e_J e_K e_L \sin \theta d\theta d\varphi - \right. \\ &\quad \left. - 3k_2 \bar{C}_{MN} \int_{\varphi=\varphi_r}^{\varphi_{r+1}} \int_{\theta=\theta_s}^{\theta_{s+1}} \rho(\varphi) e_I e_J e_K e_L e_M e_N \sin \theta d\theta d\varphi + \right. \\ &\quad \left. + k_2 \bar{C}_{MN} \bar{C}_{OP} \int_{\varphi=\varphi_r}^{\varphi_{r+1}} \int_{\theta=\theta_s}^{\theta_{s+1}} \rho(\varphi) e_I e_J e_K e_L e_M e_N e_O e_P \sin \theta d\theta d\varphi \right\}.\end{aligned}\quad (11)$$

Finite Muscle Element for Quasi-Static Contraction: As mentioned above, a Mooney-Rivlin material formulation is chosen to describe the matrix, i. e., besides the penalty part for dilatation $U(J)$ all other parts depend on isochoric deformation measures $(\bar{\lambda}_f, \bar{\mathbf{F}}, \bar{\mathbf{C}})$.

As can be seen in Figure 3, a muscle fibre consists of layers of sarcomeres, which are the force generating elements of a muscle. Due to this series connection, during quasi-static loading each sarcomere layer has to generate the same force, i. e., the same mean stress value. There exists an optimal fibre stretch value $\bar{\lambda}_{f,\text{opt}}$ for which the highest number of cross-links between myosin and actin filaments is given and therefore the highest stress value can be achieved. The peak of this stress-stretch-curve has the value $\sigma_{\text{max},0} = P \cdot f(U_{\text{rel}})$ where $f(U_{\text{rel}}) = F/F_{\text{max}} = \sigma_{f0}/\sigma_{f0,\text{max}}$ is the force law presented in chapter 2.2. The influence of the fibre stretch $\bar{\lambda}_f$ is taken into account by the function $g(\bar{\lambda}_f)$. For quasi-static contraction the stress generated in the fibre and the stress acting externally on the fibre have to be equal. The external stress is set to the stress value according to the actual fibre stretch and electric activation: $\sigma_{f0,\text{ext}} = P \cdot f(U_{\text{rel}}) \cdot g(\bar{\lambda}_f)$. This stress value refers to the physiological cross-section in the undeformed state. The corresponding Cauchy stress is then $\sigma_{f,\text{ext}} = \sigma_{f0,\text{ext}} \cdot dA/da = \bar{\lambda}_f \sigma_{f0,\text{ext}}$. The internal stress value depends on the elastic deformation of the fibre (elastic deformation of the filaments) which is very small in comparison with the "plastic" deformation which is given by the relative movement of actin and myosin filaments (cf. Figure 5). In contrast to the tendinous tissue, the muscle fibres of the contractile tissue are locally oriented in parallel, i. e., there exists only one fibre direction. As long as passive behavior is of no interest and therefore not modelled (muscle fibres are surrounded by thin layers of tendinous tissue, which impede a elongation of the fibres), the active fibre stresses are added to the right hand side and no additional entries due to the fibres occur in the stiffness matrix. Using the plastic fibre deformation at each Gauss-point as history variable, the muscle deformation corresponding to the actual electric activation can be found.

3 Results and Discussion

The following results arise from the rigid body analysis based on a purely geometrical estimation of the lines of action.

For the intrinsic muscle strength a mean value $P = 0.32 \pm 0.12 \text{ N/mm}^2$ was found. The results for the muscle and joint forces under a resultant bite force magnitude of 150 N are shown in Figure 6. Here, corresponding muscle and joint forces of the right and left side have been averaged. The right muscles and the right condyle perform the same task for $\varphi = 0^\circ, 60^\circ, 90^\circ, 180^\circ, 270^\circ, 300^\circ$ as the left muscles and the left condyle for $\varphi = 0^\circ, 300^\circ, 270^\circ, 180^\circ, 90^\circ, 60^\circ$, respectively. The values for the muscle volumes calculated from the MRTs and the correlating physiological cross-sectional areas correspond well

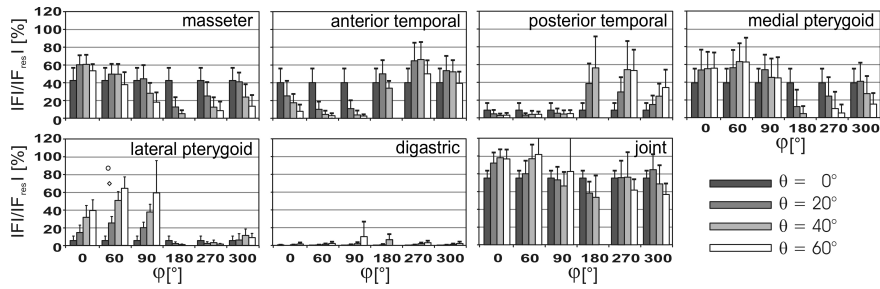


Fig. 6. Muscle and joint forces of the “right” side (values of right and left side are averaged for corresponding tasks) under a resultant bite force of $F_{\text{res}} = 150$ N.

with those found in literature [7, 4]. This holds especially for test persons of about the same age quoted in [4].

The estimation of the lines of action based on the geometry delivers reliable results if the individual muscle is activated homogeneously. However, especially for laterally and medially oriented tasks, measurements show a heterogeneous activation of the musculature as also described in [1]. This muscle behavior might essentially influence the lines of action. Therefore, the presented results for the intrinsic muscle strength P are presumably less accurate for these tasks than for the protrusive or vertical (symmetric) tasks. Nevertheless, the mean value for all calculated intrinsic muscle strengths corresponds well with values given in literature. For example, Weijs and Hillen [7] found $P = 0.37$ N/mm².

With the exception of the anterior temporal, the individual muscles developed the highest force values in clenching directions which corresponded roughly to their line of action. This supports the assumption that the motor control selects the activation state of the masticatory muscles with regard to their directional effectiveness. The relatively high force generation of the anterior temporal during lateral and posterior force development, however, might be essential for stabilizing the ipsilateral jaw joint during these tasks.

The joint force magnitude ranges from about 60% to 100% of the magnitude of the resultant bite force. It is known from measurements that chewing forces lie between 50 and 250 N, i. e., $F_{\text{res}} = 150$ N corresponds to a moderate chewing force. However, maximum forces with magnitudes over 800 N can be generated.

4 Conclusions and Outlook

A reliable calculation of the intrinsic muscle strength P requires an individual adjustment of the force law. The presented force and EMG measurements clearly show a non-linear dependence of the muscle force on the electric activity. Motor control seems to favor a directional effectiveness of the muscles when selecting the task-dependent intermuscular activation patterns. When

large bite forces are developed, the joint force magnitudes are about 60% of the magnitude of the resultant bite force. This might predispose an overloading of the jaw joint tissues.

With the developed finite elements for tendinous and contractile tissue, additionally the contraction of the muscles under inhomogeneous electric activation can be taken into account, and the lines of action can be computed for every motor task. This will yield more reliable results for the intrinsic muscle strength P and the muscle forces. Furthermore, the FE analysis will give detailed information about the stresses in the joint region, i. e., in the articular disc and fossa mandibulae.

References

1. Blanksma, N. G. & van Eijden, T. M. G. J.: Electromyographic heterogeneity in the human temporalis and masseter during static biting, open/close excursions, and chewing. *Journal of Dental Research* **74** (1995), 1318–1327.
2. van Eijden, T. M. G. J.; Korfage, J. A. M. & Brugman, P.: Architecture of the human jaw-closing and jaw-opening muscles. *The Anatomical Record* **248** (1997), 464–474.
3. Gasser, T. C.; Ogden, R. W. & Holzapfel, G. A.: Hyperelastic Modelling of arterial layers with distributed collagen fibre orientations. *Journal of the Royal Society Interface* **3** (2006), 15–35.
4. Hsu, C. W.; Shiau, Y. Y.; Chen, C. M.; Chen, K. C. & Liu, H. M.: Measurement of the size and orientation of human masseter and medial pterygoid muscles. *Proceedings National Science Council, ROC (B)* **25** (1) (2001), 45–49.
5. Schindler, H. J.; Rues, S.; Türp, J. C. & Lenz, J.: Activity patterns of the masticatory muscles during feedback-controlled simulated clenching activities. *European Journal of Oral Sciences* **113** (2005), 469–478.
6. Schumacher, G. H.: *Funktionelle Morphologie der Kaumuskulatur*. VEB Gustav Fischer Verlag, Jena, 1961.
7. Weijs, W. A. & Hillen, B.: Cross-sectional areas and estimated intrinsic strength of the human jaw muscles. *Acta Morphologica Neerlando-Scandinavica* **23** (1985), 267–274.

On Mechanical Modelling of Arterial Walls and Parallel Solution Strategies

J. Schröder¹, A. Klawonn², D. Balzani¹, O. Rheinbach² & D. Brands¹

¹ Institut für Mechanik, Fachbereich Bauwissenschaften,
Universität Duisburg-Essen, Universitätsstr. 15, 45177 Essen, Germany

² Numerische Mathematik, Fachbereich Mathematik
Universität Duisburg-Essen, Universitätsstr. 3, 45177 Essen, Germany

Abstract. Biological soft tissues appearing in arterial walls are characterized by a nearly incompressible, anisotropic, hyperelastic material behavior in the physiological range of deformations. For the representation of such materials we apply a polyconvex strain energy function in order to ensure the existence of minimizers and in order to satisfy the Legendre-Hadamard condition automatically.

The 3D discretization results in a large system of equations, therefore a parallel algorithm is applied to solve the equilibrium problem. Domain decomposition methods like the FETI-DP (Dual-Primal Finite Element Tearing and Interconnecting) method are designed to solve large linear equation systems that arise from the discretization of partial differential equations on parallel computers. Their numerical and parallel scalability, as well as their robustness, also in the incompressible limit, has been shown theoretically and in numerical simulations. We are using a dual-primal FETI method to solve elasticity problems for three dimensional models of arterial walls and present some preliminary numerical results.

1 Introduction

In recent years cardiovascular disease has become one of the most frequent causes of death. Therefore, development in the field of modelling and simulation of biological tissues has become more important. In many cases accumulations of plaques, evolved from atherosclerotic degeneration of the blood vessels, increase the risk of arterial occlusion. The balloon-angioplasty, the nidation of stents, and the combination of these two techniques are established methods of treatment.

The understanding of the anatomy and composition of arterial walls is an essential topic for the of their mechanical behavior. Because of the interest in large deformations, we focus our interest on the modelling of elastic arteries. An example of a healthy elastic artery is shown in Figure 1. The classification into three layers is a common abstraction of an arterial wall. These layers are named intima (tunica intima), media (tunica media), and adventitia (tunica externa).

The FE-simulation of an arterial wall, especially of a diseased one, represents a challenging task with view to the large number of degrees of freedom. Robust, parallel solvers are essential for the solution of the resulting

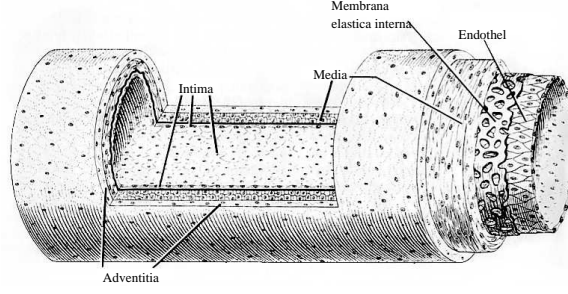


Fig. 1. Histology of a healthy artery [7].

large linear systems of equations. FETI-DP domain decomposition methods, originally introduced in [5], have been shown to be numerical and parallel scalable and robust for a huge class of problems in structural mechanics, see also [8, 9, 11].

2 Continuum Mechanical Preliminaries

The body of interest in the reference configuration is denoted by $\mathcal{B} \subset \mathbb{R}^3$, parametrized in \mathbf{X} and the current configuration by $\mathcal{S} \subset \mathbb{R}^3$, parametrized in \mathbf{x} . The non-linear deformation map $\varphi_t : \mathcal{B} \rightarrow \mathcal{S}$ at time $t \in \mathbb{R}_+$ maps points $\mathbf{X} \in \mathcal{B}$ onto points $\mathbf{x} \in \mathcal{S}$. The deformation gradient \mathbf{F} is defined by

$$\mathbf{F}(\mathbf{X}) := \nabla \varphi_t(\mathbf{X}) \quad (1)$$

with the Jacobian $J(\mathbf{X}) := \det \mathbf{F}(\mathbf{X}) > 0$. An important strain measure, the right Cauchy-Green tensor, is defined by

$$\mathbf{C} := \mathbf{F}^T \mathbf{F}. \quad (2)$$

We consider hyperelastic materials, which postulate the existence of a so-called strain energy function $\psi(\mathbf{C}) = W(\mathbf{F})$, assumed to be defined per unit reference volume. Now we focus on energy functions of the type $W = \hat{W}(\mathbf{F}, \bullet)$. The argument (\bullet) denotes additional tensor arguments, which characterize the anisotropy of the material. We consider perfect elastic materials, which means that the internal dissipation \mathcal{D}_{int} is zero for every admissible process. The constitutive equations for the stresses are obtained by evaluation of the Clausius-Duhem inequality, neglecting thermal effects, in the form

$$\mathcal{D}_{\text{int}} = \mathbf{P} : \dot{\mathbf{F}} - \dot{W} = (\mathbf{P} - \partial_{\mathbf{F}} W) : \dot{\mathbf{F}} \geq 0 \rightarrow \mathbf{P} = \partial_{\mathbf{F}} W. \quad (3)$$

The first Piola-Kirchhoff stress tensor is denoted by \mathbf{P} and $\dot{\mathbf{F}}$ denotes the material time derivative of the deformation gradient. Furthermore, $\partial_{\mathbf{F}}(\bullet)$ is the abbreviation for $\partial(\bullet)/\partial \mathbf{F}$.

In the case of anisotropy we introduce a material symmetry group \mathcal{G}_k with respect to a local reference configuration, which characterizes the anisotropy

class of the material. The elements of \mathcal{G}_k are denoted by the orthogonal tensors ${}^i\mathbf{Q} | i = 1, \dots, n$. The concept of material symmetry requires the constitutive law to be invariant under transformations with elements of the symmetry group, i. e.,

$$\hat{W}(\mathbf{F}\mathbf{Q}) = \hat{W}(\mathbf{F}) \quad \Leftrightarrow \quad \hat{\mathbf{P}}(\mathbf{F}\mathbf{Q}) = \hat{\mathbf{P}}(\mathbf{F})\mathbf{Q} \quad \forall \mathbf{Q} \in \mathcal{G}_k, \forall \mathbf{F}. \quad (4)$$

We say that the function W or \mathbf{P} in (4) are \mathcal{G}_k -invariant functions. Without any restrictions we set $\mathcal{G}_k \subset \text{SO}(3)$, where $\text{SO}(3)$ denotes the special orthogonal group.

Thus, it is clear that material symmetries impose several restrictions on the form of the constitutive functions for an anisotropic material. In order to work out the explicit restrictions for the individual symmetry groups, i. e., to point out general forms of the functions satisfying these restrictions, the use of representation theorems for anisotropic tensor functions represents a reasonable approach.

The basic idea is the extension of \mathcal{G}_k -invariant functions such that they become invariant for a larger group, here the special orthogonal group. This implies that it is in principle possible to transform an anisotropic constitutive function to an isotropic one by introducing some tensors, the so-called structural tensors, which reflect the symmetry group of the considered material. This theorem was originally introduced by Boehler in 1979, see [4]. Here, we use the structural tensor \mathbf{M} , which is given by

$$\mathbf{M} := \mathbf{a} \otimes \mathbf{a}, \quad (5)$$

where \mathbf{a} is the unit vector in the preferred direction. Taking advantage of the material frame indifference, we obtain a reduced constitutive equation,

$$\psi = \hat{\psi}(\mathbf{C}, \mathbf{M}) = \hat{\psi}(\mathbf{Q}^T \mathbf{C} \mathbf{Q}, \mathbf{Q}^T \mathbf{M} \mathbf{Q}) \quad \forall \mathbf{Q} \in \text{SO}(3), \quad (6)$$

which is the definition of an isotropic, scalar-valued tensor function in the arguments (\mathbf{C}, \mathbf{M}) .

For the construction of specific constitutive equations the invariants of the deformation tensor \mathbf{C} and the additional structural tensor \mathbf{M} are necessary. The explicit expressions for the principle invariants of \mathbf{C} are

$$I_1 := \text{tr} \mathbf{C}, \quad I_2 := \text{tr}[\text{cof} \mathbf{C}], \quad I_3 := \det \mathbf{C}. \quad (7)$$

Let \mathbf{M} be of rank-one and let us assume the normalization condition $\|\mathbf{M}\| = 1$, then the additional invariants, the so-called mixed invariants, are

$$J_4 := \text{tr}[\mathbf{C}\mathbf{M}], \quad J_5 := \text{tr}[\mathbf{C}^2\mathbf{M}], \quad (8)$$

see, e. g., [14] and the references therein.

3 Material Modelling of Biological Soft Tissues

Generally, from the mechanical point of view, soft biological tissues may be characterized as an isotropic, non-collageneous matrix, the so-called ground substance, in which collagen fibers are embedded. In arterial walls the fibers are arranged in two directions which are crosswire helically wound along the artery and symmetrically disposed with respect to the longitudinal direction. The material behavior in fiber direction can be represented by the superposition of two transversely isotropic models, see [6], and we obtain the strain energies to be of the form

$$\psi_{\text{media}} = \psi_{\text{media}}^{\text{iso}} + \sum_{a=1}^2 \psi_{\text{media}}^{\text{ti},(a)}, \quad \psi_{\text{adv}} = \psi_{\text{adv}}^{\text{iso}} + \sum_{a=1}^2 \psi_{\text{adv}}^{\text{ti},(a)}, \quad (9)$$

where the superscript a is associated to the two fiber directions \mathbf{a}_1 and \mathbf{a}_2 . Herein, ψ_{media} and ψ_{adv} denote the energies for the media and the adventitia, respectively.

In order to guarantee the existence of minimizers polyconvex functions in the sense of [1] for the strain energy are considered. Polyconvex strain energy functions automatically satisfy the quasiconvexity, the rank-one convexity, and the Legendre-Hadamard condition. In the context of anisotropic polyconvexity see e.g. [3, 12, 13].

Polyconvexity: $\mathbf{F} \rightarrow W(\mathbf{F})$ is polyconvex if and only if there exists a function $P: \mathbb{R}^{3 \times 3} \times \mathbb{R}^{3 \times 3} \times \mathbb{R} \rightarrow \mathbb{R}$ (in general non-unique) such that

$$W(\mathbf{F}) = P(\mathbf{F}, \text{Adj}[\mathbf{F}], \det[\mathbf{F}])$$

and the function $\mathbb{R}^{19} \rightarrow \mathbb{R}$, $(\mathbf{F}, \text{Adj}[\mathbf{F}], \det[\mathbf{F}]) \rightarrow P(\mathbf{F}, \text{Adj}[\mathbf{F}], \det[\mathbf{F}])$ is convex for all points $\mathbf{X} \in \mathbb{R}^3$.

Here and in the following, we omit the \mathbf{X} -dependence of the individual functions if there is no danger of confusion. The adjoint of \mathbf{F} is defined by $\text{Adj}[\mathbf{F}] = \det[\mathbf{F}]\mathbf{F}^{-1}$ for all invertible \mathbf{F} .

Since we assume the ground substance in soft tissues to behave in an isotropic manner, we consider isotropic functions for its description. The first terms on the right hand sides in (9) are both given as

$$\psi^{\text{iso}} = c_1 \left(\frac{I_1}{I_3^{1/3}} - 3 \right) + \varepsilon_1 \left(I_3^{\varepsilon_2} + \frac{1}{I_3^{\varepsilon_2}} - 2 \right), \quad (10)$$

with $c_1 > 0$, $\varepsilon_1 > 0$, $\varepsilon_2 > 1$, which satisfies the condition of a stress-free reference configuration a priori. This polyconvex function is similar to the one used in [6].

Soft biological tissues are characterized by an exponential-type stress-strain behavior in the fiber direction. A polyconvex model for the description

of these materials, which also satisfies the natural state condition, is proposed in [2] and given by

$$\psi^{\text{ti},(a)} = \begin{cases} \alpha_1 \left(K_3^{(a)} - 2 \right)^{\alpha_2} & \text{for } K_3^{(a)} \geq 2 \\ 0 & \text{for } K_3^{(a)} < 2 \end{cases} \quad \text{with } \alpha_1 \geq 0, \alpha_2 > 1. \quad (11)$$

Here, $K_3^{(a)} = I_1 J_4^{(a)} - J_5^{(a)}$ is a fundamental polyconvex function for transverse isotropy, with the invariants $J_4^{(a)} = \text{tr}[\mathbf{C}\mathbf{M}_{(a)}]$ and $J_5^{(a)} = \text{tr}[\mathbf{C}^2\mathbf{M}_{(a)}]$ using $\mathbf{M}_{(a)} := \mathbf{a}_{(a)} \otimes \mathbf{a}_{(a)}$, cf. [12]. In order to obtain smooth tangent moduli close to the reference configuration we introduce the slightly more restrictive condition $\alpha_2 > 2$.

4 Variational Formulation and FE-Discretization

In the following, we give a brief summary of our material description, i. e., the corresponding boundary value problem and the finite element formulation. Let \mathcal{B} be the reference body of interest which is bounded by the surface $\partial\mathcal{B}$. The surface is partitioned into two disjoint parts $\partial\mathcal{B} = \partial\mathcal{B}_u \cup \partial\mathcal{B}_t$. The balance of linear momentum for the static case, neglecting body forces, is given by

$$\text{Div}[\mathbf{P}] = \mathbf{0} \quad \text{with} \quad \mathbf{P} = \partial_{\mathbf{F}}\psi = 2\mathbf{F}\partial_{\mathbf{C}}\psi = \mathbf{F}\mathbf{S}, \quad (12)$$

where \mathbf{S} denotes the second Piola-Kirchhoff stress tensor. The Dirichlet and the Neumann boundary conditions are given by $\mathbf{u} = \bar{\mathbf{u}}$ on $\partial\mathcal{B}_u$ and $\mathbf{t} = \bar{\mathbf{t}} = \mathbf{P}\mathbf{N}$ on $\partial\mathcal{B}_t$. Here, \mathbf{N} represents the unit normal on the boundary surface $\partial\mathcal{B}_t$. Applying standard arguments of variational calculus, we obtain the weak form

$$G(\mathbf{u}, \delta\mathbf{u}) = \int_{\mathcal{B}} \delta\mathbf{F} : \mathbf{P} \, dV + G^{\text{ext}}, \quad \text{where } G^{\text{ext}} := - \int_{\partial\mathcal{B}_t} \delta\mathbf{u} \cdot \bar{\mathbf{t}} \, dA, \quad (13)$$

and $\delta\mathbf{F} := \text{Grad} \delta\mathbf{u}$ characterizes the virtual deformation gradient. The principle of virtual work for a static equilibrium state of the considered body requires $G = 0$. For the solution of this non-linear equation we apply a standard Newton iteration scheme, which requires the consistent linearization of (13) in order to guarantee quadratic convergence in the neighborhood of the solution. The linearization of $G(\mathbf{u}, \delta\mathbf{u})$ is given by

$$\text{Lin} G = G(\mathbf{u}, \delta\mathbf{u}) + \Delta G(\mathbf{u}, \delta\mathbf{u}, \Delta\mathbf{u}), \quad (14)$$

with the linear increment

$$\Delta G(\mathbf{u}, \delta\mathbf{u}, \Delta\mathbf{u}) = \int_{\mathcal{B}} \delta\mathbf{F} : \mathbf{A} : \Delta\mathbf{F} \, dV, \quad (15)$$

and the incremental deformation gradient $\Delta\mathbf{F} := \text{Grad} \Delta\mathbf{u}$. The nominal tangent moduli \mathbf{A} can be computed via

$$\mathbf{A} = \partial_{\mathbf{F}}(\mathbf{F}\mathbf{S}) = \mathbf{I} \boxtimes \mathbf{S} + \mathbf{F} \cdot \mathbf{C} : \frac{1}{2} \partial_{\mathbf{F}}\mathbf{C}, \quad (16)$$

with the material moduli $\mathbf{C} := 2\partial_{\mathbf{C}}\mathbf{S}$, using the definition of the Kronecker product of second order tensors $(\mathbf{A} \boxtimes \mathbf{B}) : (\mathbf{a} \otimes \mathbf{b}) = \mathbf{A}\mathbf{a} \otimes \mathbf{B}\mathbf{b}$. The spatial discretization of \mathcal{B} by $\bigcup_{e=1}^{n_{\text{ele}}} \mathcal{B}^e$ using n_{ele} finite elements \mathcal{B}^e , with the approximations $\mathbf{u} = \sum_{I=1}^{n_{\text{ele}}} N^I \mathbf{d}_I$, $\delta \mathbf{u} = \sum_{I=1}^{n_{\text{ele}}} N^I \delta \mathbf{d}_I$ and $\Delta \mathbf{u} = \sum_{I=1}^{n_{\text{ele}}} N^I \Delta \mathbf{d}_I$ for the actual, virtual, and incremental displacement fields, respectively, leads to a set of algebraic equations. The discrete counterpart of equation (13) reads

$$G^h = \sum_{e=1}^{n_{\text{ele}}} \delta \mathbf{d}^{\text{T}} \left\{ \int_{\mathcal{B}} \mathbb{B}^{\text{T}} \mathbf{P}^{\text{h}} \, dV - \int_{\mathcal{B}_t} \mathbf{N}^{\text{T}} \bar{\mathbf{t}} \, dA \right\} = \sum_{e=1}^{n_{\text{ele}}} \delta \mathbf{d}^{e\text{T}} \mathbf{r}^e \quad (17)$$

and the linear increment for a typical element is given by

$$\Delta G^{e,\text{int}} = \delta \mathbf{d}^{e\text{T}} \int_{\mathcal{B}^e} \mathbb{B}^{\text{T}} \mathbf{A}^{\text{h}} \mathbb{B} \, dV \Delta \mathbf{d}^e = \delta \mathbf{d}^{e\text{T}} \mathbf{k}^e \Delta \mathbf{d}^e. \quad (18)$$

The superscript h in the latter equations represents a suitable contracted matrix notation of the associated quantities. Thus we obtain from $\text{Lin } G^h = 0$ the linear system of equations

$$\sum_{e=1}^{n_{\text{ele}}} \delta \mathbf{d}^{e\text{T}} (\mathbf{k}^e \Delta \mathbf{d}^e - \mathbf{r}^e) = \delta \mathbf{D}^{\text{T}} (\mathbf{K} \Delta \mathbf{D} - \mathbf{f}) = 0, \quad (19)$$

with the global incremental displacement field $\Delta \mathbf{D}$, virtual displacement $\delta \mathbf{D}$, right hand side \mathbf{f} and the global stiffness matrix \mathbf{K} . The algebraic system $\mathbf{K} \Delta \mathbf{D} = \mathbf{f}$ is solved iteratively until $\|\mathbf{f}\| < \text{tol}$ is reached. For the following analysis it is convenient to introduce the (incremental) bilinear form of the linearized weak form

$$a_{\mathbf{u}}(\Delta \mathbf{u}, \delta \mathbf{u}) := \int_{\mathcal{B}} \delta \mathbf{F} : \mathbf{A} : \Delta \mathbf{F} \, dV \quad (20)$$

and the associated right hand side

$$f(\delta \mathbf{u}) := \int_{\partial \mathcal{B}_t} \delta \mathbf{u} \cdot \bar{\mathbf{t}} \, dA. \quad (21)$$

Here, $a_{\mathbf{u}}(\delta \mathbf{u}, \Delta \mathbf{u}) := a(\Delta \mathbf{u}, \delta \mathbf{u}; \mathbf{u})$ denotes the evaluation of the linear increment at the previous solution.

In the following section we will describe the dual-primal version of the FETI method which we apply to solve our linearized systems. For a general overview on FETI methods see [10].

5 FETI Domain Decomposition Method

We decompose our reference body \mathcal{B} into N nonoverlapping subbodies \mathcal{B}_i of diameter H , which we also call subdomains. Each subdomain is the union of finite elements with matching finite element nodes on the boundaries of neighbouring subdomains across the interface $\Gamma := \bigcup_{i \neq j} \partial \mathcal{B}_i \cap \partial \mathcal{B}_j$. Here,

$\partial\mathcal{B}_i, \partial\mathcal{B}_j$ are the boundaries of $\mathcal{B}_i, \mathcal{B}_j$, respectively. Typically, a graph partitioning tool is used to define the decomposition of the body into subdomains, see, e. g., [9, ?].

For each subdomain \mathcal{B}_i , $i = 1, \dots, N$, we assemble the local stiffness matrices $\mathbf{K}^{(i)}$ and load vectors $\mathbf{f}^{(i)}$ using (20) and (21). We denote the displacement increment on subdomain \mathcal{B}_i by $\Delta\mathbf{D}^{(i)}$.

We then partition the displacement increment $\Delta\mathbf{D}^{(i)}$ into primal variables $\Delta\mathbf{D}_{\Pi}^{(i)}$ and nonprimal variables $\Delta\mathbf{D}_B^{(i)}$. In FETI-DP algorithms, we enforce the continuity of the solution in the primal displacement increments $\Delta\mathbf{D}_{\Pi}^{(i)}$ by global subassembly of the subdomain stiffness matrices $\mathbf{K}^{(i)}$. For all other interface variables $\Delta\mathbf{D}_{\Delta}^{(i)}$ we will introduce Lagrange multipliers to enforce continuity.

First, we partition the stiffness matrices and right hand sides according to the different sets of unknowns,

$$\mathbf{K}^{(i)} = \begin{bmatrix} \mathbf{K}_{BB}^{(i)} & \mathbf{K}_{\Pi B}^{(i)T} \\ \mathbf{K}_{\Pi B}^{(i)} & \mathbf{K}_{\Pi\Pi}^{(i)} \end{bmatrix}, \quad \mathbf{f}^{(i)} = \begin{bmatrix} \mathbf{f}_B^{(i)} \\ \mathbf{f}_{\Pi}^{(i)} \end{bmatrix},$$

and

$$\mathbf{K}_{BB}^{(i)} = \begin{bmatrix} \mathbf{K}_{\Pi\Pi}^{(i)} & \mathbf{K}_{\Delta I}^{(i)T} \\ \mathbf{K}_{\Delta I}^{(i)} & \mathbf{K}_{\Delta\Delta}^{(i)} \end{bmatrix}, \quad \mathbf{f}_B^{(i)} = \begin{bmatrix} \mathbf{f}_I^{(i)} \\ \mathbf{f}_{\Delta}^{(i)} \end{bmatrix}.$$

We then gather these matrices and vectors in block matrix form,

$$\begin{aligned} \mathbf{K}_{BB} &:= \text{diag}_{i=1}^N(\mathbf{K}_{BB}^{(i)}), \\ \mathbf{K}_{\Pi B} &:= \text{diag}_{i=1}^N(\mathbf{K}_{\Pi B}^{(i)}), \\ \mathbf{K}_{\Pi\Pi} &:= \text{diag}_{i=1}^N(\mathbf{K}_{\Pi\Pi}^{(i)}), \end{aligned}$$

and in block right hand sides

$$\mathbf{f}_B^T := [\mathbf{f}_B^{(1)T}, \dots, \mathbf{f}_B^{(N)T}], \quad \mathbf{f}_{\Pi}^T := [\mathbf{f}_{\Pi}^{(1)T}, \dots, \mathbf{f}_{\Pi}^{(N)T}].$$

By assembly of the local subdomain matrices in the primal variables using the assembly operator $\mathbf{R}_{\Pi}^T = [\mathbf{R}_{\Pi}^{(1)T}, \dots, \mathbf{R}_{\Pi}^{(N)T}]$ with entries 0 or 1, we obtain the partially assembled, global stiffness matrix

$$\widetilde{\mathbf{K}} := \begin{bmatrix} \mathbf{K}_{BB} & \widetilde{\mathbf{K}}_{\Pi B}^T \\ \widetilde{\mathbf{K}}_{\Pi B} & \widetilde{\mathbf{K}}_{\Pi\Pi} \end{bmatrix} = \begin{bmatrix} \mathbf{I}_B & 0 \\ 0 & \mathbf{R}_{\Pi}^T \end{bmatrix} \begin{bmatrix} \mathbf{K}_{BB} & \mathbf{K}_{\Pi B}^T \\ \mathbf{K}_{\Pi B} & \mathbf{K}_{\Pi\Pi} \end{bmatrix} \begin{bmatrix} \mathbf{I}_B & 0 \\ 0 & \mathbf{R}_{\Pi} \end{bmatrix}$$

and the corresponding right hand side

$$\widetilde{\mathbf{f}} := \begin{bmatrix} \mathbf{f}_B \\ \widetilde{\mathbf{f}}_{\Pi} \end{bmatrix} = \begin{bmatrix} \mathbf{I}_B & 0 \\ 0 & \mathbf{R}_{\Pi}^T \end{bmatrix} \begin{bmatrix} \mathbf{f}_B \\ \mathbf{f}_{\Pi} \end{bmatrix}.$$

In our algorithm, for every pair of subdomains with $\overline{\mathcal{B}_i} \cap \overline{\mathcal{B}_j}$, $i \neq j$, a sufficient number of primal variables $\Delta\mathbf{D}_{\Pi}^{(i)}$ is chosen and we obtain a symmetric,

positive definite matrix $\widetilde{\mathbf{K}}$. This matrix is only coupled in the primal variables and its structure is still suitable for efficient parallelization.

To enforce the continuity in the remaining interface variables $\Delta \mathbf{D}_\Delta^{(i)}$, we introduce a jump operator \mathbf{B}_B with entries 0, -1 or 1 and the corresponding Lagrange multipliers $\boldsymbol{\lambda}$.

We can now formulate the FETI-DP saddle-point problem

$$\begin{bmatrix} \mathbf{K}_{BB} & \widetilde{\mathbf{K}}_{\Pi B}^T & \mathbf{B}_B^T \\ \widetilde{\mathbf{K}}_{\Pi B} & \widetilde{\mathbf{K}}_{\Pi \Pi} & 0 \\ \mathbf{B}_B & 0 & 0 \end{bmatrix} \begin{bmatrix} \Delta \mathbf{D}_B \\ \Delta \widetilde{\mathbf{D}}_\Pi \\ \boldsymbol{\lambda} \end{bmatrix} = \begin{bmatrix} \underline{\mathbf{f}}_B \\ \underline{\mathbf{f}}_\Pi \\ 0 \end{bmatrix}. \quad (22)$$

By eliminating $\Delta \mathbf{D}_B$ and $\Delta \widetilde{\mathbf{D}}_\Pi$ from the system (22) we obtain an equation system

$$\mathbf{F}_{\text{FETI}} \boldsymbol{\lambda} = \mathbf{d}.$$

In order to define the preconditioner for the method, we define

$$\mathbf{K}_{II} := \text{diag}_{i=1}^N(\mathbf{K}_{II}^{(i)}), \quad \mathbf{K}_{\Delta I} := \text{diag}_{i=1}^N(\mathbf{K}_{\Delta I}^{(i)}), \quad \mathbf{K}_{\Delta \Delta} := \text{diag}_{i=1}^N(\mathbf{K}_{\Delta \Delta}^{(i)}).$$

The Dirichlet preconditioner \mathbf{M}_{FETI} is then defined by

$$\mathbf{M}_{\text{FETI}}^{-1} := \mathbf{B}_{B,\mathcal{D}}(\mathbf{R}_\Delta^B)^T (\mathbf{K}_{\Delta \Delta} - \mathbf{K}_{\Delta I} \mathbf{K}_{II}^{-1} \mathbf{K}_{\Delta I}^T) \mathbf{R}_\Delta^B \mathbf{B}_{B,\mathcal{D}}^T,$$

where $\mathbf{R}_\Delta^B = \text{diag}_{i=1}^N(\mathbf{R}_\Delta^{B(i)})$. The matrices $\mathbf{R}_\Delta^{B(i)}$ are restriction matrices with entries 0 or 1 which restrict the nonprimal degrees of freedom $\Delta \mathbf{D}_B^{(i)}$ of a subdomain to the dual part $\Delta \mathbf{D}_\Delta^{(i)}$. The matrices $\mathbf{B}_{B,\mathcal{D}}$ are scaled variants of the jump operator \mathbf{B}_B , where the contribution from and to each interface node is scaled by the inverse of the multiplicity of the node. The multiplicity of a node is defined as the number of subdomains it belongs to. It is well known that for heterogeneous problems a more elaborate scaling is necessary; see, e. g., [8]. The scaled jump operator $\mathbf{B}_{B,\mathcal{D}}$ can be written as

$$\mathbf{B}_{B,\mathcal{D}} = [\mathbf{B}_{B,\mathcal{D}}^{(1)}, \dots, \mathbf{B}_{B,\mathcal{D}}^{(N)}] = [\mathcal{D}^{(1)} \mathbf{B}_B^{(1)}, \dots, \mathcal{D}^{(N)} \mathbf{B}_B^{(N)}].$$

In the heterogeneous case, the matrices $\mathbf{B}_{B,\mathcal{D}}^{(i)}$, $i = 1, \dots, N$, are defined as follows: Each row of $\mathbf{B}_B^{(i)}$ with a nonzero entry corresponds to a Lagrange multiplier λ connecting the subdomain \mathcal{B}_i with a neighboring subdomain \mathcal{B}_j . Let us write the entry on the main diagonal of the subdomain stiffness matrix $\mathbf{K}^{(i)}$ which is related to the Lagrange multiplier λ as $k^{(i)}(x)$. Here, the notation symbolizes that the local degree of freedom originates from a global degree of freedom x . Accordingly, the corresponding entry on the main diagonal of the subdomain stiffness matrix $\mathbf{K}^{(j)}$ is denoted by $k^{(j)}(x)$. The scaled matrix $\mathbf{B}_{B,\mathcal{D}}^{(i)}$ is now obtained by multiplying each such element of $\mathbf{B}_B^{(i)}$ by $\frac{[k^{(j)}(x)]^\gamma}{\sum_{l \in \mathcal{N}_x} [k^{(l)}(x)]^\gamma}$, $\gamma \in [1/2, \infty)$, where \mathcal{N}_x is the set of indices of the

subdomains where local degrees of freedom correspond to x . If all $k^{(l)}(x)$, $l \in \mathcal{N}_x$ are the same and if $\gamma = 1$, this scaling reduces to the multiplicity scaling mentioned before for homogeneous problems.

We now solve the system $\mathbf{F}_{\text{FETI}}\boldsymbol{\lambda} = \mathbf{d}$ with the preconditioner $\mathbf{M}_{\text{FETI}}^{-1}$ using a suitable Krylov subspace method, e. g., the method of generalized minimal residuals GMRES.

6 A First Simulation using the Anisotropic Material Model

As a first test problem, we consider a uniaxial tension test for a quasi-incompressible cubic body up to a strain of 30 percent of the side length. The orientation of the fibres in our material model is chosen such that it coincides with the axis of the strain test. We thus have a hardening of the material and an increasing influence of the anisotropy during the simulation. We use a parallel FETI-DP implementation to solve the linearized equation systems using restarted GMRES(100) as a Krylov subspace accelerator. The FETI-DP iteration for the linearized systems is stopped once a relative residual reduction of 10^{-12} is reached. The nonlinear iteration uses an absolute tolerance of 10^{-7} . Thus, we solve the linearized systems to a much higher accuracy than the Newton iteration. To study the influence of the anisotropy which is present in our material model on the convergence of the method, we repeat the simulation using the same material model but omitting the anisotropic part. The cubic body, see Figure 2, is discretized using 26,982 second order tetrahedral elements which results in 116,973 degrees of freedom.

Newton Step	Anisotropic						Isotropic			
	1	2	3	4	5	6	1	2	3	4
Load Step 1	198	328	197	197	-	-	198	328	197	197
Load Step 2	197	281	197	196	-	-	197	281	197	196
Load Step 3	196	262	196	196	-	-	196	264	197	197
Load Step 4	196	198	188	188	-	-	197	261	196	196
Load Step 5	188	257	183	185	186	186	196	256	197	197
Load Step 6	186	352	223	221	220	220	197	252	197	197
Load Step 7	220	252	252	252	-	-	197	249	198	198
Load Step 8	252	295	272	272	272	-	198	246	198	198
Load Step 9	272	363	289	288	288	-	198	245	199	199
Load Step 10	288	395	302	301	301	-	199	244	200	200

Table 1. Uniaxial strain test. Number of FETI-DP iterations for each Newton step. Relative tolerance for the linear solver: 10^{-12} . Absolute tolerance for the Newton iteration: 10^{-7} .

From the results in Table 1 we see that, in the isotropic case, the number of Newton steps remains constant during the simulation. Likewise, the number of FETI-DP iterations only varies slightly throughout the simulation. On the

other hand, in the anisotropic case, the number of Newton steps as well as the number of FETI-DP iterations grows by a factor of up to 1.5 as the influence of the anisotropy grows during the simulation. The total number of GMRES steps in the simulation thus is slightly higher in the anisotropic case (11,444 it.) than in the isotropic case (8,551 it.).

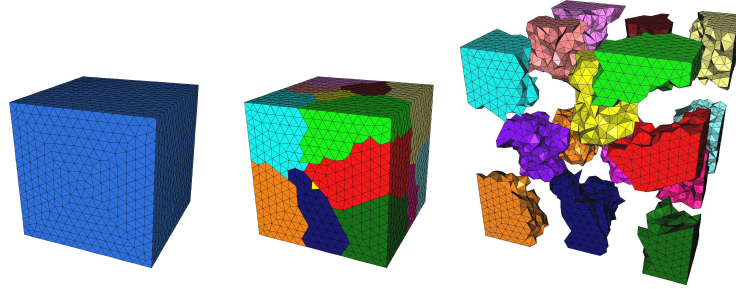


Fig. 2. Decomposition of the cubic body in the FETI-DP algorithm.

Our results show that our method is robust with respect to the quasi-incompressibility and in the presence of the anisotropies built into our material model. Furthermore, the FETI-DP method is indeed reliably able to reduce the residual of the linearized systems by 12 orders of magnitude. Thus, the method seems suitable for the simulation of arterial walls using our anisotropic, polyconvex material model, cf. Figure 3.

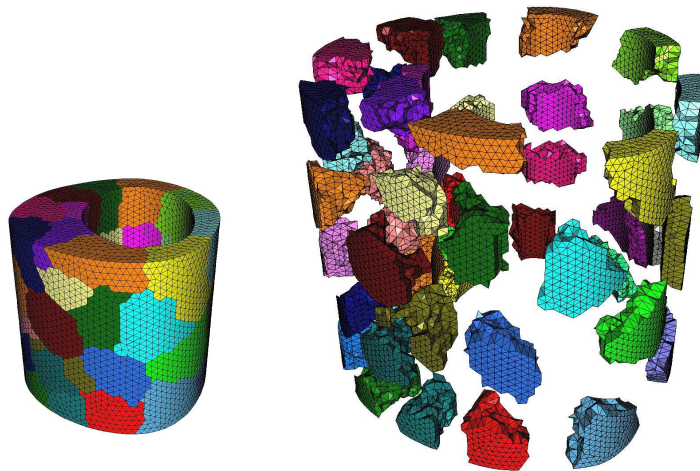


Fig. 3. Decomposition of an arterial segment in the FETI-DP algorithm.

Acknowledgements: The work of the authors was supported by the Deutsche Forschungsgemeinschaft (DFG) under research grants KL 2094/1-1 and SCHR 570/7-1.

References

1. Ball, J. M.: Convexity conditions and existence theorems in non-linear elasticity. *Archive for Rational Mechanics and Analysis* **63** (1977), 337–403.
2. Balzani, D.; Neff, P.; Schröder, J. & Holzapfel, G. A.: A Polyconvex Framework for Soft Biological Tissues. Adjustment to Experimental Data. *International Journal of Solids and Structures* **43** (2006), 6052–6070.
3. Balzani, D.: *Polyconvex Anisotropic Energies and Modeling of Damage Applied to Arterial Walls*. PhD-Thesis, Scientific Report of the Institute of Mechanics, University Duisburg-Essen, Verlag Glückauf, Essen 2006.
4. Boehler, J. P.: Introduction to the invariant formulation of anisotropic constitutive equations. In Boehler J. P. (ed.), *Applications of Tensor Functions in Solid Mechanics*, CISM Course No. 292. Springer-Verlag, Berlin, 1987.
5. Farhat, C.; Lesoinne, M.; LeTallec, P.; Pierson, K. H. & Rixen, D.: FETI-DP: A dual-primal unified FETI method - Part I: A faster alternative to the two-level FETI method. *International Journal for Numerical Methods in Engineering* **50** (2001), 1523–1544.
6. Holzapfel, G. A.; Gasser, T. C. & Ogden, R. W.: A new constitutive framework for arterial wall mechanics and a comparative study of material models. *Journal of Elasticity* **61** (2000), 1–48.
7. Junqueira, L. C. & Carneiro, J.: Histologie. Springer-Verlag, Berlin, 1991.
8. Klawonn, A.; Widlund, O. B.: Dual-Primal FETI Methods for Linear Elasticity. *Communications on Pure and Applied Mathematics* **59** (2006), 1523–1572.
9. Klawonn, A.; Rheinbach, O.: A parallel implementation of Dual-Primal FETI methods for three dimensional linear elasticity using a transformation of basis. *SIAM Journal on Scientific Computing* **28** (2006), 1886–1906.
10. Klawonn, A.: FETI Domain Decomposition Methods for Second Order Elliptic Partial Differential Equations. *GAMM-Mitteilung* **29** (2006), 319–341.
11. Rheinbach, O.: *Parallel Scalable Iterative Substructuring: Robust Exact and Inexact FETI-DP Methods with Applications to Elasticity*. PhD-Thesis, Fachbereich Mathematik, Universität Duisburg-Essen, 2006.
12. Schröder, J. & Neff, P.: Invariant Formulation of Hyperelastic Transverse Isotropy Based on Polyconvex Free Energy Functions. *International Journal of Solids and Structures* **40** (2003), 401–445.
13. Schröder, J.; Neff, P. & Balzani, D.: A Variational Approach for Materially Stable Anisotropic Hyperelasticity. *International Journal of Solids and Structures* **42** (2004), 4352–4371.
14. Spencer, A. J. M.: Isotropic Polynomial Invariants and Tensor Functions. In Boehler J. P. (ed.), *Applications of Tensor Functions in Solid Mechanics*, CISM Course No. 292. Springer-Verlag, Berlin, 1987.

Wave Propagation in Cancellous Bones

H. Steeb

Chair of Applied Mechanics, Saarland University,
Department of Materials Sciences, Campus A4 2, 66123 Saarbrücken, Germany

Abstract. Wave propagation in fluid-saturated cancellous bone is studied on the basis of the thermodynamically consistent Theory of Porous Media (TPM). In comparison with Gassmann's relation, Wyllie's relation and Biot's equations, it is shown that a simple, so-called hybrid biphasic model based on the Theory of Porous Media is able to capture the main acoustical effects in cancellous bones. Furthermore, an extension towards high-frequency wave propagation is discussed on the basis of the constitutive relation of the momentum exchange between the fluid and the solid phase.

1 Introduction

In the present contribution, we discuss the acoustical properties of cancellous bone saturated with bovine marrow or water. Due to the increasing importance of ultrasound techniques as non-invasive techniques for the detection of osteoporosis, advanced modelling techniques have to be developed in order to explain the measured experimental velocities and attenuation effects in a qualitative and quantitative way. Then, the ultimate goal of such a quantitative model is the prediction of the porosity in order to detect osteoporosis. In this context, Biot's theory for wave propagation in fluid-saturated porous media, cf. [1–3], is discussed extensively. Besides the existence of one transversal and two longitudinal waves, the fast or P1 wave and the the so-called slow, P2 or Biot's wave, Biot's equations predict a frequency-dependent attenuation effect. The present paper focuses on the phase velocities of monochromatic waves in cancellous bones. As we do not take into account higher order coupling effects between the fluid and the solid phase, attenuation effects caused by so-called inertia coupling are not investigated in the present contribution. Obviously, these effects become dominating in the high frequency, i. e., ultrasonic, regime. Furthermore, we do not introduce a modification of the concept of permeability¹. Within the first part of the paper a summary of the basic modelling aspects is given in combination with some additional remarks. In the second part, we apply the hybrid biphasic model to wave propagation

¹ In Biot's original contribution discussing the high frequency range, cf. [2] and many following papers, the permeability was replaced by a frequency-dependent permeability function. As pointed out clearly by Wilmański [19] such a frequency-dependent complex permeability is inappropriate from a mathematical point of view. Therefore, it should be avoided.

phenomena in bones. We compare the phase velocities of a simple, so-called hybrid biphasic model based on the thermodynamically consistent Theory of Porous Media (TPM) with the results obtained by the Biot-Gassmann relations in the low-frequency range, cf. [8, 17], as a function of porosity.

2 Modelling Concepts – The Hybrid Mixture Model

In contrast to Biot's equations, the mixture theory is based on the principles of rational continuum-thermodynamics of superimposed continua. Consequently, the basic kinematical relations and balance equations are inherently non-linear. Obviously, linear models can be obtained a posteriori by a formal linearization step.

In the present context, we apply the framework of the Theory of Porous Media, cf. [5, 7], which extends the classical mixture theory by the concept of volume fractions. Thus, the superimposed continuum on the macroscale has lost all microscopical information except for the volumetrical decomposition of a Representative Volume Element (RVE). Thus, the volume fraction of the constituent φ^α is introduced as $n^\alpha = dv^\alpha/dv$ where dv^α is the part of the RVE with the volume dv , which is occupied by the constituent φ^α . Furthermore, the partial density is introduced as dm^α/dv using the mass of the single constituent φ^α . If the mass dm^α is related to its volume dv^α we obtain the definition of the effective or true density $\rho^{\alpha R} := dm^\alpha/dv^\alpha$. The volume fraction relates the partial and the effective density $\rho^\alpha = n^\alpha \rho^{\alpha R}$. Furthermore, an algebraic constraint is introduced, the so-called saturation condition $\sum_\alpha n^\alpha = 1$. Note that most of the models based on the TPM deal with quasi-static phenomena within geotechnical applications like consolidation problems or slope instabilities of landslides, cf. [5] or [7]. In the field of such applications it is often assumed that both, the solid and the liquid constituent, behave material incompressible, i. e., $\rho^{\alpha R} = \text{const}$. Nevertheless, such models are not suitable for wave propagation investigations. They lead to unphysical results as there can not occur any in-phase movement of the solid and the liquid constituent. Thus, the first or fast longitudinal wave (P1-wave) has an infinite velocity.

2.1 Kinematical Assumptions

Within fluid-saturated porous materials, the balance of mass of the constituent φ^α can be expressed as

$$\rho_0^\alpha = J_\alpha \rho^\alpha, \quad \text{with } J_\alpha = \det \mathbf{F}_\alpha \neq 0. \quad (1)$$

The deformation gradient of the individual constituent is given as $\mathbf{F}_\alpha = \partial \mathbf{x} / \partial \mathbf{X}_\alpha$, with the position vector \mathbf{X}_α of the constituent φ^α in the reference configuration and the mixture's position \mathbf{x} in the current configuration. In the following, the index $(\bullet)_0$ refers to quantities in the initial configuration.

For a material incompressible constituent, (1) is reduced to the mapping of the volume fractions

$$n_0^\alpha = J_\alpha n^\alpha. \quad (2)$$

As we restrict ourselves to small amplitudes, i. e., small deformations, the deformation gradient is further linearized

$$\text{lin}(\det \mathbf{F}_\alpha) = \text{lin}(J_\alpha) = \text{div } \mathbf{u}_\alpha + 1 = \text{tr } \boldsymbol{\varepsilon}_\alpha + 1. \quad (3)$$

We have introduced the displacements $\mathbf{u}_\alpha = \mathbf{x} - \mathbf{X}_\alpha$ and the linearized strain tensor $\boldsymbol{\varepsilon}_\alpha = 1/2(\text{grad } \mathbf{u}_\alpha + \text{grad}^T \mathbf{u}_\alpha)$. If we apply (2) and (3) to a hybrid biphasic mixture, i. e., a materially incompressible solid skeleton ($\rho^{sR} = \rho_0^{sR}$) with an inherent compressible pore fluid ($\rho^{fR} \neq \text{const}$), we obtain the following kinematical conditions for the fluid

$$\rho_0^f = (1 + \text{div } \mathbf{u}_f) \rho^f =: (1 + \varepsilon) \rho^f, \quad (4)$$

and the solid constituent

$$n_0^s = (1 + \text{div } \mathbf{u}_s) n^s =: (1 + e) n^s. \quad (5)$$

Note that in the context of the compressible Biot's equations such a hybrid model is often denoted as the so-called rigid grain limit. Now, it is necessary to point out the modelling consequences of these kinematical conditions. In a hybrid biphasic mixture with a known motion function, the system of equations for the six unknowns $\{n^s, n^f, \rho^s, \rho^f, \rho^{sR}, \rho^{fR}\}$ is closed with the balances of mass, (4) and (5), the algebraic relations between the partial and effective densities, the saturation condition and the incompressibility constraint, cf. Table 1. Obviously, this is not the case for the fully compressible case ($\rho^{sR} \neq \text{const.}$ and $\rho^{fR} \neq \text{const.}$), where further constitutive assumptions on the basis of evolution equations are needed, cf. [4, 6]. Alternatively, a further balance relation for the porosity can be introduced as proposed by Wilmański [18], cf. the comments in Kirchner [15]. In the opposite case, i. e., for the fully incompressible model ($\rho^{sR} = \text{const.}$ and $\rho^{fR} = \text{const.}$), the system of equations is over-determined. Thus, a further constraint has to be taken into account, which can be every single equation of Table 1 (left) or a combination of them.

Obviously, within the hybrid model, the system of equations can be solved directly and we obtain an explicit expression for the evolution of the porosity depending only on the volumetric deformation of the solid skeleton

$$n^f = \phi = \phi_0 + (1 - \phi_0) e. \quad (6)$$

Thus, the porosity $\phi(\mathbf{x}, t)$ is a dependent field variable which is evolving during the process. Note that a comparable relation of the porosity can also be found for the fully compressible model of Biot, as pointed out in a recent

contribution [19]. Wilmański's porosity balance for the linear compressible model can be also discussed for the rigid grain limit

$$\lim_{K^s \rightarrow \infty} \phi = \phi \left(1 - \delta e + \frac{\Phi}{\phi_0} (e - \varepsilon) \right) = \phi_0 + (1 - \phi_0) e, \quad (7)$$

which is identical to the direct derivation within the hybrid model. Applying similar arguments, we obtain a relation for the effective density of the pore fluid in the case of the hybrid biphasic mixture model

$$\rho^{fR} = \rho_0^{fR} \left(1 - \varepsilon - \frac{1 - \phi_0}{\phi_0} e \right), \quad (8)$$

which states that the effective density ρ^{fR} of the pore fluid depends on the volumetrical deformation of the fluid and the solid constituent, respectively.

	incompressible model	hybrid model	compressible model
I.	$\rho^s = n^s \rho^{sR}$	$\rho^s = n^s \rho^{sR}$	$\rho^s = n^s \rho^{sR}$
II.	$\rho^f = n^f \rho^{fR}$	$\rho^f = n^f \rho^{fR}$	$\rho^f = n^f \rho^{fR}$
III.	$n^s = J_s^{-1} n_0^s$	$n^s = J_s^{-1} n_0^s$	$\rho^s = J_s^{-1} \rho_0^s$
IV.	$n^f = J_f^{-1} n_0^f$	$\rho^f = J_f^{-1} \rho_0^f$	$\rho^f = J_f^{-1} \rho_0^f$
V.	$\rho^{sR} = \text{const.}$	$\rho^{sR} = \text{const.}$	—
VI.	$\rho^{fR} = \text{const.}$	—	—
VII.	$n^s + n^f = 1$	$n^s + n^f = 1$	$n^s + n^f = 1$
	$7 - 6 = +1$	$6 - 6 = 0$	$5 - 6 = -1$

Table 1. Kinematical behaviour of biphasic models and consequences.

2.2 Balance Relations

The governing balances of the hybrid two-phase model are the balance of momentum of the solid and fluid constituent

$$\rho^s \ddot{\mathbf{u}}_s - \text{div } \boldsymbol{\sigma}^s = -\hat{\mathbf{p}}^f, \quad \text{and} \quad \rho^f \ddot{\mathbf{u}}_f - \text{div } \boldsymbol{\sigma}^f = \hat{\mathbf{p}}^f. \quad (9)$$

It has to be remarked, that within a linear model, we do not have to distinguish between the partial and the material time derivatives. Thus $\partial_t(\mathbf{u}_\alpha) = \dot{\mathbf{u}}_\alpha$. Furthermore, we have neglected body forces. The term of the right hand side of (9) is the direct momentum interaction, which takes the interacting equilibrium and non-equilibrium forces between the solid and the pore-fluid into account, e. g., the viscous drag forces in the most simple case.

2.3 Constitutive Assumptions

The model, cf. the balance equations (9), is closed with the kinematical conditions, cf. Table 1, and a set of appropriate constitutive equations for the set of response functions $\mathcal{R} = \{\boldsymbol{\sigma}_E^s, p, \hat{\mathbf{p}}^f\}$. We have evaluated the effective stress principle for the partial stresses $\boldsymbol{\sigma}^\alpha = \boldsymbol{\sigma}_E^\alpha - n^\alpha p \mathbf{I}$. Furthermore, an order-of-magnitude analysis [11] shows that the extra stress \mathbf{T}_E^f of the fluid is of higher order. Thus, it is convenient for most applications in porous media that the viscous shear stresses of the pore fluid are assumed to be zero resulting in $\boldsymbol{\sigma}_E^f = \mathbf{0}$.

Pressure: The constitutive equation of the pore pressure $p(\mathbf{x}, t)$ in the case of a barotropic fluid reads $p = f(\rho^{fR})$. It can be shown from the entropy balance that the simplest thermodynamically consistent relation between the effective density of the compressible fluid and the pore pressure is a linear relation, well-known as the ideal gas or Boyle-Mariotte's law, respectively.

$$p \propto \rho^{fR} \quad \Longrightarrow \quad p = p_0 + \kappa \rho^{fR}. \quad (10)$$

Resorting the terms and disregarding the mixed non-linear contribution yields a simple constitutive expression for the pore pressure $p(\mathbf{x}, t)$ depending on material parameters, which are given with respect to the initial configuration \mathcal{B}_0 , i. e., $(\rho_0^{fR}, n_0^s, n_0^f)$, and the volumetrical deformation of the fluid and the solid constituent (ε, e)

$$p = p_0 - \kappa \rho_0^{fR} \varepsilon - \kappa \frac{n_0^s}{n_0^f} \rho_0^{fR} e = p_0 - K^f \varepsilon - \frac{n_0^s}{n_0^f} K^f e. \quad (11)$$

Furthermore, the compressibility of the pore fluid is characterized by K^f .

Effective Stress of the Solid Skeleton: The effective stress of the solid skeleton is given by Hooke's law

$$\boldsymbol{\sigma}_E^s = 2\mu \boldsymbol{\varepsilon}_s + \lambda e \mathbf{I}, \quad (12)$$

with the Lamé parameters μ and λ of the empty porous skeleton. Therefore, we can calculate the bulk modulus of the empty skeleton $K = \lambda + \frac{2}{3}\mu$.

Momentum Interaction: The interaction part of the balances of momentum is split into an equilibrium part denoted by $\hat{\mathbf{p}}_{eq}^f$ and a part which vanishes at thermodynamical equilibrium denoted by $\hat{\mathbf{p}}_{neq}^f$. Evaluating the balance of entropy we obtain

$$\hat{\mathbf{p}}^f = \hat{\mathbf{p}}_{eq}^f + \hat{\mathbf{p}}_{neq}^f = p \text{grad } n^f + \hat{\mathbf{p}}_{neq}^f. \quad (13)$$

Generally speaking, the non-equilibrium part of the momentum interaction depends on the complete set of non-equilibrium process variables and yields a non-linear constitutive equation, which can be formulated using further

concepts of the theory of materials, i. e., isotropic vector-valued functions. To complete the linear model, we assume, that $\hat{\mathbf{p}}_{neq}^f$ is proportional to the seepage velocities which yields the well-known Darcy law

$$\hat{\mathbf{p}}_{neq}^f = -\frac{(n^f)^2 \gamma^{fR}}{k^f} (\dot{\mathbf{u}}_f - \dot{\mathbf{u}}_s) =: -\pi (\dot{\mathbf{u}}_f - \dot{\mathbf{u}}_s). \quad (14)$$

Here, we have introduced the generalized conductivity π which can be related to the Darcy permeability k^f . Furthermore, the effective weight of the fluid is introduced as γ^{fR} . Discussing (13), we find that in a linear model the equilibrium part only remains if the initial porosity distribution is inhomogeneous.

2.4 Field Equations

Assuming homogeneous initial porosity distributions, we formulate the resulting field equations by inserting the constitutive assumptions into the balances of momentum

$$\begin{aligned} \rho_0^s \ddot{\mathbf{u}}_s - (\lambda + \mu + \frac{(n_0^s)^2}{n_0^f} K^f) \text{grad div } \mathbf{u}_s - \\ - n_0^s K^f \text{grad div } \mathbf{u}_f - \mu \text{div grad } \mathbf{u}_s - \pi (\dot{\mathbf{u}}_f - \dot{\mathbf{u}}_s) = \mathbf{0}, \quad (15) \\ \rho_0^f \ddot{\mathbf{u}}_f - n_0^f K^f \text{grad div } \mathbf{u}_f - \\ - n_0^s K^f \text{grad div } \mathbf{u}_s + \pi (\dot{\mathbf{u}}_f - \dot{\mathbf{u}}_s) = \mathbf{0}. \end{aligned}$$

The standard ansatz $\mathbf{u}_\alpha(\mathbf{x}, t) = \mathbf{U}_\alpha \exp[i(\mathbf{k} \cdot \mathbf{x} - \omega t)]$ is used in combination with the longitudinal direction of the wave vector \mathbf{k}^{\parallel} and the transversal part \mathbf{k}^{\perp} to obtain the dispersion relations. For the transversal mode we obtain

$$(\rho_0^s \omega^2 - \mu k^2 + i \pi \omega)(\rho_0^f \omega^2 + i \pi \omega) - (i \pi \omega)^2 = 0, \quad (16)$$

and for the longitudinal mode we get

$$\begin{aligned} (\rho_0^s \omega^2 - (\lambda + 2\mu + \frac{(n_0^s)^2}{n_0^f} K^f) k^2 + i \pi \omega) (\rho_0^f \omega^2 - n_0^f K^f k^2 + i \pi \omega) - \\ - (n_0^s K^f k^2 + i \pi \omega)^2 = 0. \quad (17) \end{aligned}$$

Equations (16) and (17) can be solved leading to three solutions of the wave vector: The real parts of the solution correspond to the phase velocities of the shear wave and to the fast and the slow longitudinal wave. The imaginary part of the wave vector is equivalent to the attenuation of the amplitude of the waves.

3 Results and Discussion

Next, we apply the hybrid biphasic model to cancellous bones saturated either with water or with bovine marrow. In the first investigation, we compare the

results obtained by well-established low-frequency models. Note that these models are usually applied to reservoir rocks [17] and used to predict seismic waves. As a matter of fact, the material properties of reservoir rocks and cancellous bones disagree completely in the range of the material parameters. Furthermore, the results of this comparison are not useful for the direct interpretation of ultrasonic experiments but they can be used to discuss the sensitivity of the models with respect to the material parameters of cancellous bones. The results of the phase velocities in longitudinal direction obtained by the TPM-model, cf. (17), are compared with the Biot-Gassmann results [1, 3, 8, 17] and the empirical quantities of Wyllie [20] in the low-frequency range ($\omega < 100$ Hz). The elastic parameters of the empty porous skeleton depend on the porosity and the fabric of the bone matrix. According to the work of Gibson [9] and Gibson & Ashby [10] these quantities are estimated as

$$K = \frac{E^s (1 - \phi_0)^n}{3(1 - 2\nu^s)}, \quad \text{and} \quad \mu = \frac{E^s (1 - \phi_0)^n}{2(1 + \nu^s)}. \quad (18)$$

Young's modulus and Poisson's ratio of the solid bone are introduced as E^s and ν^s , respectively. Note that these quantities are well documented in the literature, cf. [12, 16]. Gassmann's low-frequency relation relates the bulk modulus of the saturated bone K_{sat} to the bulk moduli of the empty skeleton K , the single trabeculae K^s and the bone fluid K^f . Note that Gassmann's relations and Biot's equations lead to the same phase velocity of the fast longitudinal wave in the low frequency range.

$$K_{sat} = K + \frac{(1 - \frac{K}{K^s})^2}{\frac{\phi_0}{K^f} + \frac{1-\phi_0}{K} - \frac{K}{(K^s)^2}} \quad \text{and} \quad \mu_{sat} = \mu. \quad (19)$$

Then, Gassmann's phase velocity c_p is calculated as

$$c_p^2 = \frac{K_{sat} + \frac{4}{3}\mu_{sat}}{\rho}. \quad (20)$$

Furthermore, the phase velocities can be compared with the heuristic time average expression proposed by Wyllie [20]. Note that Wyllie's equation is based on experimental data without theoretical basis

$$\frac{1}{c_p} = \frac{\phi_0}{c_p^f} + \frac{1 - \phi_0}{c_p^s}. \quad (21)$$

Herein, $c_p^f(K^f)$ is the phase velocity of the bone fluid while $c_p^s(K^s, \mu^s)$ is the velocity of the solid bone. In Figure 1 we plot the phase velocity of the fast longitudinal wave vs. porosity in the low-frequency range. The gray-shaded area marks the porosity range of a human cancellous bone. There, it is observed that the amount of compressibility of the solid skeleton K dominates the wave

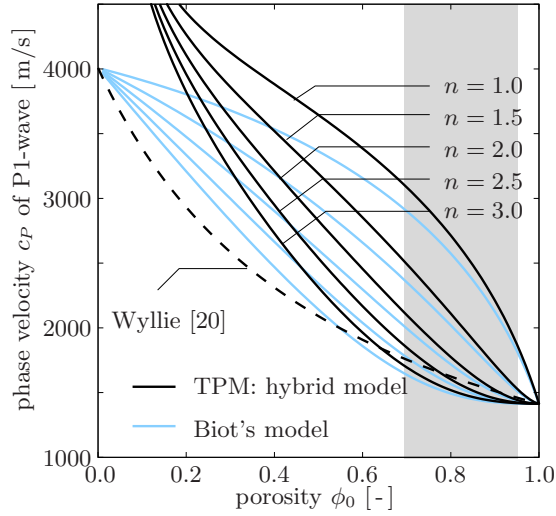


Fig. 1. Low-frequency phase velocity of cancellous bone saturated with water. Comparison of phase velocities calculated with Wyllie’s model and Gassmann’s relations for the Biot case and the hybrid two-phase model. Bulk modulus of the skeleton K^s is calculated according to Gibson’s equation with varying exponents n , cf. (18).

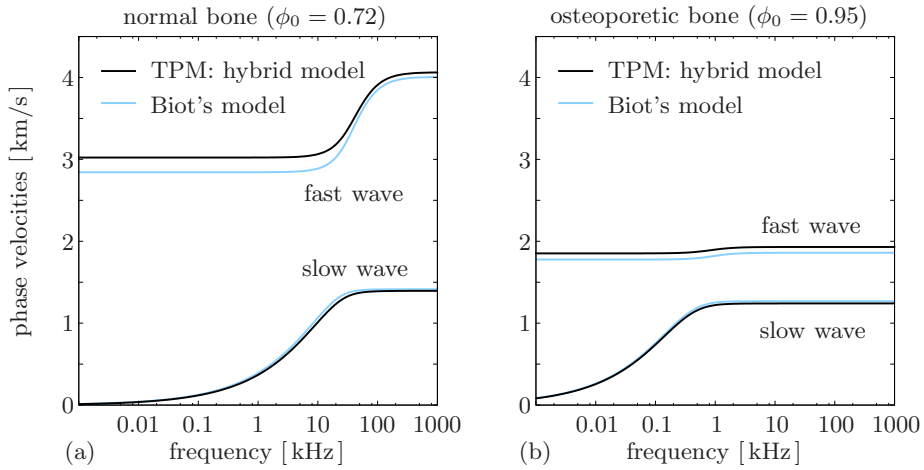


Fig. 2. Phase velocities of the fast and the slow longitudinal wave as functions of frequency for a normal bone and an osteoporetic bone. Bulk modulus of the skeleton K^s is calculated according to Gibson’s equation with an exponents $n = 1.0$, cf. (18).

speed, while the differences between the compressible Biot’s model and the more simpler hybrid TPM model are of lower order. Even Wyllie’s empirical relation (21) delivers practical results which are comparable to the models of Biot and the TPM approach. Furthermore, as shown in Figure 1, the quality

Material parameter			
bulk modulus of single trabecula	K^s	20.37	GPa
Poisson's ratio of single trabecula	ν^s	0.32	
initial porosity (normal bone)	ϕ_0	0.72	
(osteoporetic bone)		0.95	
effective density solid	ρ^{sR}	1960.0	kG/m ³
bulk modulus of fluid	K^f	2.0	GPa
effective density bovine marrow	ρ_0^{fR}	930.0	kG/m ³
intrinsic permeability (normal bone)	k^s	5.0e-9	m ²
(osteoporetic bone)		5.0e-7	m ²
effective dynamic viscosity bone marrow (20° C)	η^{fR}	0.15	Pas
(37° C)		0.05	Pas
pore radius (normal bone)	r	285	μm
(osteoporetic bone)		455	μm
phase velocity bone marrow	c_p^f	1467	m/s
phase velocity solid bone	c_p^s	4008	m/s

Table 2. Material parameters of fluid-saturated cancellous bone.

of Gibson's relation (18) strongly depends on the exponent n . Therefore, it seems to be important to investigate the elastic behaviour of the bone fabric in more detail, either by numerical homogenization techniques or by more-detailed micro-mechanical investigations based on μCT -data. Note that the small differences between Biot's equations and the hybrid TPM model can also be observed in the frequency range, cf. Figure 2. In the diagram of Figure 2 (a) we plot the phase velocity of the fast and the slow longitudinal wave vs. the frequency for a normal bone, while in the right diagram, cf. Figure 2 (b), analogous results are shown for an osteoporetic bone. Note that the out-of-phase velocities of the slow longitudinal wave coincide more or less for both models.

As a conclusion, it could be noted that both models, the TPM-based hybrid biphasic model and Biot's model, predict the phase velocities quite well for realistic porosities and bulk moduli. Experimental data obtained by ultrasound techniques, cf. [12], are also comparable to these theoretically calculated results. Nevertheless, the whole picture is only closed if we also compare the dissipative effects of the experiment with the attenuation predicted by the model, i. e., the imaginary part of the wave number. As clinical ultrasound techniques operate in a bandwidth of 200-600 kHz we have to take effects in the high frequency range into account, cf. [13]. As remarked earlier in this contribution, this could only be achieved by a more realistic

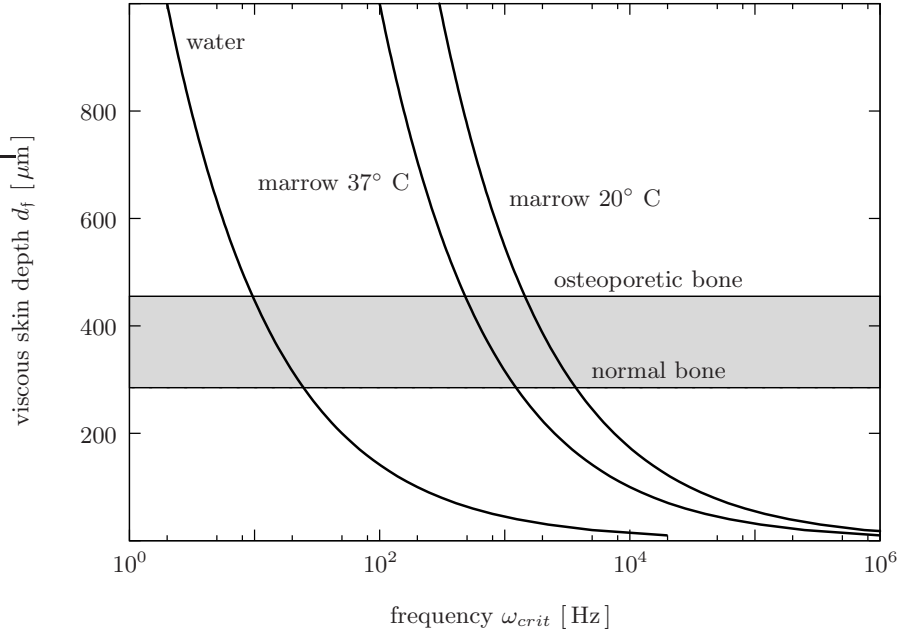


Fig. 3. Viscous skin depth versus frequency for bovine marrow at 20° C and 30° C and water at 20° C.

physically-based ansatz for the non-equilibrium momentum interaction (inertia coupling), cf. (13) and the remarks in the recent work of Wilmański [19]. In the low frequency range viscous coupling locks the bone matrix and the bone marrow and prevents a travelling slow wave. Unlike the low frequency range a travelling wave can be observed in the high frequency range. Therefore, the high-frequency range is also much more interesting from a parameter identification point of view. The strong frequency-dependent phase velocity, cf. Figure 2, and attenuation effect of the slow wave could be used as additional information to identify material parameters of the bone, e. g., porosity, permeability, etc. Furthermore, the high frequency range is characterized by the so-called critical frequency ω_{crit} , cf. [1, 2, 13]. If the microstructure of the bone fabric is known, for instance by μ CT imaging techniques, the critical frequency ω_{crit} is met, if the viscous skin depth d_f equals the pore radius r . Thus, ω_{crit} itself can be calculated from

$$\omega_{crit} = \frac{2\eta^{fR}}{\rho_0^{fR} r^2} = \frac{2\eta^{fR}}{\rho_0^{fR} d_f^2}. \quad (22)$$

For realistic bone properties, cf. [14], the viscous skin depth d_f vs. the critical frequency ω_{crit} is plotted in Figure 3 for various bone fluids. The gray-shaded region is denoted to realistic bone microstructures in the normal and the osteoporetic range. From the simple microscopical calculations of the crit-

ical frequency (22) it could be stated that standard ultrasonic techniques, like the Broadband Ultrasonic Attenuation technique (BUA), cf. [13], are in the high frequency range. Therefore, it seems to be very promising for the inverse identification of inherent bone properties like porosity, bulk moduli, permeability etc, to use both, the (frequency-dependent) phase velocities of the fast and the slow wave and the (frequency-dependent) attenuation effect of the slow wave.

Even if it was demonstrated that a simple TPM-based hybrid biphasic model is able to capture phase velocities in cancellous bones quite well, it seems to be important to include more physically-based high-frequency effects into the model. Especially, non-standard momentum interaction terms and added mass effects seem to play a significant role in the ultrasonic, i. e., high frequency range. In contrast to the approach of Biot, such contributions can be included into a mixture theory-based model in a rational way.

Acknowledgment

The author wants to thank Stefan Schmalholz (ETH Zürich) and Stefan Diebels (Saarland University) for various helpful and quite lengthy discussions concerning wave propagation phenomena in porous materials.

References

1. Biot, M. A.: Theory of propagation of elastic waves in a fluid-saturated porous solid. I. Low-frequency range. *Journal of the Acoustical Society of America* **29** (1956), 168–178.
2. Biot, M. A.: Theory of propagation of elastic waves in a fluid-saturated porous solid. II. Higher frequency range. *Journal of the Acoustical Society of America* **29** (1956), 179–191.
3. Biot, M. A.: Mechanics of deformation and acoustic propagation in porous media. *Journal of Applied Physics* **33** (1962), 1482–1498.
4. Bluhm, J.: *A consistent Model for Saturated and Empty Porous Media*. Techn. Rep. 74, Forschungsberichte aus dem Fachbereich Bauwesen, Universität-GH-Essen, 1997.
5. de Boer, R.: *Trends in Continuum Mechanics of Porous Media*. Springer-Verlag, Berlin, 2005.
6. Diebels, S.: *Mikropolare Zweiphasenmodelle: Modellierung auf der Basis der Theorie Poröser Medien*. Habilitationsschrift, Institut für Mechanik (Bauwesen), Nr. II-4, Universität Stuttgart, 2000.
7. Ehlers, W. & Bluhm, J.: *Porous Media: Theory, Experiments and Numerical Applications*. Springer-Verlag, Berlin, 2002.
8. Gassmann, F.: Über die Elastizität poröser Medien. *Vierteljahresschrift der Naturforschenden Gesellschaft in Zürich* **96** (1951), 1–23.
9. Gibson, L. J.: The mechanical behaviour of cancellous bone. *Journal of Biomechanics* **18** (1985), 317–328.
10. Gibson, L. J. & Ashby, M. F.: *Cellular solids. Structure and Properties*. Cambridge University Press, Cambridge, 1997.

11. Hassanizadeh, S. M. & Gray, W. G.: High flow velocity in porous media. *Transport in Porous Media* **2** (1987), 521–531.
12. Hosokawa, A.; Otani, T.; Suzaki, T.; Kubo, Y. & Sakai, S.: Influences of trabecular structure on ultrasonic wave propagation in bovine cancellous bone. *Japanese Journal of Applied Physics* **36** (1997), 3233–3237.
13. Hughes, E. R.; Leighton, T. G.; Petley, G. W. & White, P. R.: Ultrasonic propagation in cancellous bone: A new stratified model. *Ultrasound in Medicine and Biology* **5** (1999), 811–821.
14. Hughes, E. R.; Leighton, T. G.; Petley, G. W.; White, P. R. & Chivers, R. C.: Estimation of critical and viscous frequencies for Biot theory in cancellous bone. *Ultrasonics* **41** (2003), 365–368.
15. Kirchner, N.: Thermodynamically consistent modelling of abrasive granular materials. I. Non equilibrium-theory. *Proceedings of the Royal Society of London. Series A* **458** (2002), 2153–2176.
16. Lee, K. I. & Yoon, S. W.: Comparison of acoustic characteristics predicted by Biot's theory and the modified Biot-Attenborough model in cancellous bone. *Journal of Biomechanics* **39** (2006), 364–368.
17. Mavko, G.; Mukerji, T. & Dvorkin, J.: *The Rock Physics Handbook. Tools for Seismic Analysis in Porous Media*. Cambridge University Press, Cambridge, 2003.
18. Wilmański, K.: A thermodynamic model of compressible porous materials with the balance equation of porosity. *Transport in Porous Media* **32** (1998), 21–47.
19. Wilmański, K.: A few remarks on Biot's model and linear acoustics of poroelastic saturated materials. *Soil Dynamics and Earthquake Engineering* **26** (2006), 509–536.
20. Wyllie, M. R. J.; Gregory, A. R. & Gardner, L. W.: Elastic wave velocities in heterogeneous and porous media. *Geophysics* **21** (1956), 41–70.

Integrated Motion Measurement in Biomechanics

J. F. Wagner

Institute of Statics and Dynamics of Aerospace Structures,
Universität Stuttgart, Pfaffenwaldring 27, 70569 Stuttgart, Germany

Abstract. Integrated navigation systems like a combination of a GPS receiver with accelerometers and gyros are powerful motion measurement devices. They are well established in vehicle guidance and allow a versatile determination of the vehicle position and angular attitude including the respective velocities with high sampling rates and good accuracies. Whereas in former times such systems were large, heavy, and expensive, modern microelectronics technology has led to increasingly small and light devices with a good price-performance ratio. Therefore, modern navigation technology recommends itself for new, unconventional applications. One of these additional possibilities is motion analysis in Biomechanics.

All navigation sensors like gyros or radar units are basically tools that detect mainly single motion components. To obtain a more complete, descriptive determination of the motion considered, an appropriate fusion of several sensor signals of complementary physical meaning is required. This forms the basic idea of integrated navigation or integrated motion measurement respectively. Besides, suitable sensor combinations can simultaneously provide a good long-term accuracy and a high resolution with respect to time. Finally, it is not necessary to restrict integrated motion measurement to a single rigid body or vehicle like in classical navigation.

In fact, some approaches of applying integrated motion measurement to Biomechanics exist already and show a promising potential for tasks like rehabilitation documentation or analysing motor learning. For this, the paper outlines the theoretical basics for integrated motion measurement and discusses existing examples.

1 Usage of Integrated Navigation Systems

The satellite navigation system GPS stands for drastic changes in navigation technology during the last years: Its accuracy, versatility, and operation ease have reached a favourable level that was never intended during the system design 30 years ago. Similar statements apply to other navigation tools like sensors (gyroscopes, accelerometers, compasses, radar units) as well as microchips for data logging and processing sensor signals.

GPS receivers and the (other) navigation sensors mentioned are in principle devices that detect single motion components of the respective vehicle considered for navigation. These are for example components of the acceleration or the angular rate vector, distances to explicit reference points, etc. To obtain a more complete, descriptive determination of the vehicle motion, a suitable combination of several sensor signals of complementary mechanical

meaning has to be employed. This is the basic idea of integrated navigation systems, which are therefore more precisely integrated motion measurement devices. If these systems are appropriately designed and if the assumption of a rigid vehicle structure is acceptable, a recording of the entire vehicle motion is possible. Simultaneously, a good long-term accuracy and a high resolution with respect to time can be provided [4].

In vehicle guidance and navigation, the use of such integrated systems is well established. However, it is also traditionally associated with high equipment weight, volume, costs, and power consumption [7]. On the other hand, the technological progress as mentioned, changes this unfavourable situation at present because modern microelectronics technology leads increasingly to small and light navigation devices with a good price-performance ratio.

The utilisation of integrated motion measurement systems in Biomechanics [11] becomes therefore more and more interesting. Indeed, some basic approaches already exist and show a promising potential for applications like motion analysis in sport, orthopaedics, and neurology, like quality management of rehabilitation processes, like sports competition diagnosis, or like medical engineering. Assessing some realised examples, the paper illustrates this situation in Section 3. Section 2 contains beforehand the necessary outline of the methodological basis for integrated motion measurement systems.

2 Principle of Integrated Motion Measurement

Position finding is a very old, essential part of navigation. It provides the location of the respective vehicle for the necessary route planning. Modern vehicle guidance tasks additionally require other kinematical vehicle characteristics like velocity, acceleration, angular rate, and (angular) attitude. This requires a more or less complete determination of the vehicle motion.

Historically, the associated kind of navigation technology is based on measuring simple geometric values like directions or distances and deducing then numerically the information required. For this, optical and acoustical bearings form old, classical measurement procedures, whereas during the 19th and 20th century numerous other sensor principles especially from gyro and radio technology appeared. Sequel to this, modern navigation technology has, as mentioned, sophisticated motion measurement systems as its disposal, which combine several sensors detecting different geometrical and kinematical parameters by various physical principles.

Besides choosing suitable sensor types, the measurement system design requires also a kinematical vehicle modelling to settle on the motion components considered to be necessary and to describe the mechanical meaning of the measurements employed. Furthermore, a mathematical procedure is required to generate the desired motion information by an appropriate fusion of all sensor signals. Details about the kinematical modelling, the sensor types, and the mathematical fusion procedure form the following subsections.

2.1 Kinematical Modelling

In navigation, a single rigid body with two, three, or six mechanical degrees of freedom traditionally idealises the vehicle considered. The latter case forms the most general one and combines the pure, complete body translation and the pure, complete body rotation with three degrees of freedom each. A rare but typical example of directly using this fact in analysing specific balance skills in sport is depicted in Figure 1 (being taken from [15]), where all motion components have a clear physical meaning and a body fixed Cartesian coordinate system is used to separate the degrees of freedom.

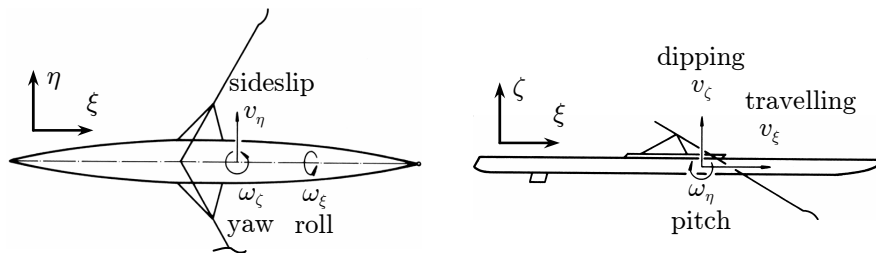


Fig. 1. All motion components of a rowing boat reflecting human balance skills.

In this classical case, when a rigid body reflects the whole motion of interest, it is not only in navigation but also in Biomechanics convenient to simply describe the body location by a single position vector \mathbf{r} and the body attitude, e. g., by three (time varying) Euler angles or a quaternion \mathbf{q} (all values with respect to a suitable coordinate system). A more detailed analysis should also include the velocity vector \mathbf{v} and acceleration vector \mathbf{a} as well as the angular rate vector $\boldsymbol{\omega}$ and the angular acceleration vector $\boldsymbol{\alpha}$ of the body. Furthermore, the equations $\mathbf{v} = \dot{\mathbf{r}}$ and $\mathbf{a} = \ddot{\mathbf{r}}$ as well as similar relations for the attitude hold.

To describe the rigid body motion more compactly, a motion state vector $\mathbf{x} = [\mathbf{r}^T \ \mathbf{v}^T \ \mathbf{q}^T]^T$ can be introduced. This is typical for inertial navigation, which is based on signals from gyros and accelerometers (“inertial sensors”). In this case, also the relation

$$\dot{\mathbf{x}} = \mathbf{f}(\mathbf{x}, \mathbf{u}) \quad (1)$$

has to be used, which establishes the relation between position, velocity, and attitude on one side and the acceleration and the angular rate on the other side. The latter two vectors are measured by the accelerometers and gyros. They form the vector $\mathbf{u} = [\mathbf{a}^T \ \boldsymbol{\omega}^T]^T$, whereas the vector function \mathbf{f} reflects simply all the relations like $\mathbf{a} = \ddot{\mathbf{r}}$. Therefore, \mathbf{f} describes the interesting body kinematics using a set of ordinary differential equations.

To determine the position, velocity and attitude from \mathbf{u} , equation (1) has to be solved numerically. (Mathematically, this is an initial value problem with a typically nonlinear function vector \mathbf{f} .) However, this procedure causes errors growing with time. To limit this inaccuracies, additional ‘aiding’ signals are necessary. The latter ones originate from, e. g., a Doppler radar, a GPS receiver, a camera, etc., and their outputs (altogether forming the aiding vector \mathbf{y}) have to be modelled by a set of algebraic equations (for a GPS receiver the equations contain, e. g., the formulation of the geometric range between the receiver antenna and the GPS satellites [4]):

$$\mathbf{y} = \mathbf{h}(\mathbf{x}, \mathbf{u}) . \quad (2)$$

Together with all sensors, equations (1) and (2) form the kernel of integrated navigation or rather integrated motion measurement systems. For the classical case of a rigid body, \mathbf{f} and \mathbf{h} are well known and proven (albeit their derivation is by no means trivial). For a short time, extended theories for modelling flexible vehicles and multibody systems exist as well [13, 14] (with the latter case being especially interesting for Biomechanics). Such structures show additional degrees of freedom and, therefore, require supplemental sensors, which have now to be distributed over all moving parts.

2.2 Common Navigation Sensors for Motion Measurement

During the last decades, various navigation sensor types became more and more attractive for Biomechanics: their size, weight, and power consumption decreased steadily to a degree enabling a nearly imperceptible, reactionless sensor attachment to test persons, sports equipment, and medical devices. Some sensor types resemble meanwhile small electronic chips [10] and can even be used for micro air vehicles [19]. Table 1 contains especially interesting devices together with the mechanical meaning of their output [4, 6, 8]. The sensors in the first three lines are especially important for \mathbf{u} ; the other sensors (including also the odometer) are typically aiding signal sources.

From this list, the accelerometer has gained already a broad acceptance in Biomechanics as a single instrument. However, its use is very critical. The sensor principle is based on measuring the inertial forces on a seismic mass, which is also subjected to gravity. Therefore, the sensor signal is a mixture between the real acceleration and the component of the negative gravity vector along the sensor input axis. The latter part has to be compensated mathematically, and this requires to know or to measure additionally the attitude (relative to the local vertical) of the body carrying the accelerometer. According to this and in anticipation to the extended theory of Wagner [14], Wu and Ladin [20] combined signals of gyros and accelerometers being distributed over a complete human body. However, they used only a reduced set of aiding sensors and could therefore not evaluate the measurements to the full extent as described in the next section.

sensor type	mechanical meaning of signal
accelerometer	component of acceleration \mathbf{a} minus gravity \mathbf{g}
gyro	component of angular rate $\boldsymbol{\omega}$
odometer	velocity of a wheel
GPS receiver	range and range rate to certain navigation satellites
electronic compass	orientation relative to the local magnetic flux lines
short range radar	range or range rate to a certain surface or point
camera	photogrammetric position of markers

Table 1. Typical navigation sensors being usable for Biomechanics.

2.3 Sensor Signal Fusion and System Integration

As mentioned, integrated motion measurement systems fuse sensor signals with different mechanical meaning. Traditionally, this task is realised by the observer principle, a well-known subject of control theory. Figure 2 illustrates this approach being explained by the popular combination of inertial sensors and GPS: The upper left block stands for the rigid body (with six degrees

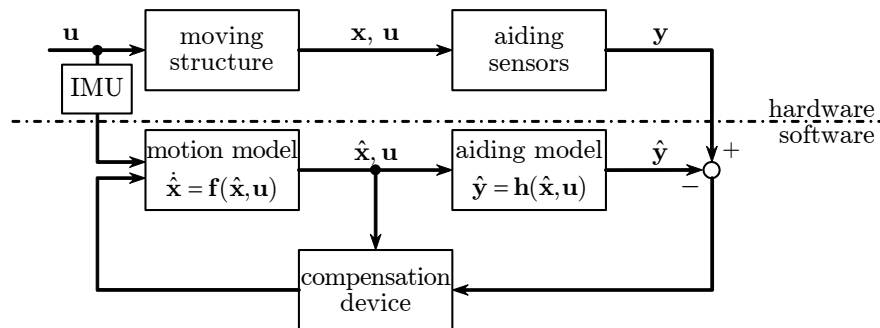


Fig. 2. Observer principle as used for integrated motion measurement.

of freedom) being subject to input \mathbf{u} (comprising \mathbf{a} and $\boldsymbol{\omega}$ as explained for equation (1)) causing the vehicle movement. This motion is described by \mathbf{x} containing \mathbf{r} , \mathbf{v} , and \mathbf{q} (as also mentioned). Based on \mathbf{x} and \mathbf{u} , the upper right block (being here a GPS receiver) provides a first set of data, the aiding measurements. Representing \mathbf{u} , a second set of data is gained through an inertial measurement unit (IMU) consisting of three accelerometers and three gyros

(each set with orthogonal measurement axes). Based on these six signals, the block “motion model”, containing the numerical solution of equation (1), calculates an estimate $\hat{\mathbf{x}}$ for the (strictly speaking) unknown state \mathbf{x} . Using the set of (normally nonlinear) algebraic equations (2) with the vector function \mathbf{h} , the block marked with “aiding model” derives estimates $\hat{\mathbf{y}}$ of \mathbf{y} . At last, a “compensation” block has the task to minimise the deviations between \mathbf{x} and $\hat{\mathbf{x}}$ using the difference $\mathbf{y} - \hat{\mathbf{y}}$. The design of the “compensation” block follows mostly the theory for the “Extended Kalman Filter” [4]. Unlikely values of $\mathbf{y} - \hat{\mathbf{y}}$ allow furthermore to identify and to miss out measurement outliers.

3 Assessment of Already Realised Examples

The design and implementation of integrated motion measurement systems is not trivial because appropriate sensors have to be selected, the handling of the functions \mathbf{f} and \mathbf{h} requires a sufficient insight in kinematics, and real-time requirements have to be met [4, 14]. A reliable and reactionless installation of the sensors and of the data processing equipment is costly and not quite simple, too. Therefore, it is explainable that up to now in Biomechanics such systems are mostly realised only in parts. The majority of the already existing examples come from sport, where motor skills and motor learning form a determining scientific area.

In the following, a selection of available examples is presented in order to give an impression about the specific state of the art and about typical difficulties in applying integrated motion measurement systems to Biomechanics. The cases listed now are partitioned with respect to sports disciplines:

- Rowing:

To measure specific forces, the use of accelerometers onboard of rowing boats has already a certain tradition (see, e. g., [5]). However, in the beginning it was not combined with the necessary attitude determination. Therefore, the significance of the data evaluation was very limited.

Based initially on military gyros, a first attitude measurement system arose at about the year 1990 and was used for studies on specific rowing balance ([15], Figure 1). These devices permitted only short-term analyses because at that time suitable aiding equipment was not available and an unaided numerical long-term integration of equation (1) is normally not feasible.

Another method to determine the yaw and pitch motion (Figure 1) of the boat is the differential position measurement with two GPS antennas, one fixed to the bow and one to the stern [17]. As GPS receivers have a limited resolution with time, this technique has, however, problems with analysing single strokes and can rather lead to statistical statements. Here, a combination with gyros and accelerometers suggests itself and would lead to an integrated system as outlined above. A realisation is no

longer a technical problem and could allow a detailed insight in balance abilities; nevertheless, an implementation does not yet exist (probably due to financing and manpower).

- Javelin:

A few years ago, a very small and light acceleration measurement unit was developed and incorporated into a javelin [18]. The value of benefit of the device is, regrettably, limited because the compensation of the gravity influence is still incomplete and the intended long-term calculation of the velocity requires an aiding. Therefore, further system development concerning three gyros and a GPS receiver is necessary. However, this could cause weight and volume problems.

- Swimming:

A few years ago, a complete inertial measurement unit (consisting of three gyros and three accelerometers) was developed and attached to the lower back of several athletes for swimming [2]. The intended long-term calculation of the velocity and position requires still an additional aiding, which could possibly be realised by underwater photogrammetry. Unfortunately, this approach does not allow the projected real-time performance assessment and causes a high technical complexity. Furthermore, the value of insight in the swimming motion is limited because the human body is not rigid (as assumed for the design of the inertial measurement unit).

- Ski jumping:

Based on a special helmet being equipped with a GPS receiver, on a light-grille barrier at the jump-off platform, and on a geodetic GPS data processing procedure, a high accurate measurement system with a precision of about 1 cm was recently developed and successfully tested to monitor the translational motion of the athlete's head [1]. Nevertheless, the critical phases of the jump-off and the landing should still be recorded with a higher sample rate (because, as mentioned, pure GPS data have a limited resolution with time). This requires additional, inertial sensors leading to an integrated system as explained with Figure 2. Furthermore, the gyros would then facilitate a supplemental analysis of the head rotation being especially interesting because of the vestibular organ.

- Inline and ice skating, cross-country skiing:

To assess the specific balance of skaters and skiers, an ankle exercise board (wobble board) was equipped with three gyros and three accelerometers. The board is basically a hemisphere rolling on the floor with its curved side down and bearing a platform on its flat, upper side. It shows primarily a pure rotational motion. Therefore, the gyros measure the angular rate vector forming \mathbf{u} , whereas the accelerometers are operated as inclinometers to provide aiding measurements \mathbf{y} for the board tilt (pitch and roll corresponding to Figure 1). With this, a complete integrated system could be realised which is tailored to the specific kinematics of the board and which estimates the rotational motion according to Figure 2 [16].

Medical rehabilitation (especially with respect to neurology and orthopaedics) is another scientific field, where motor skills and motor learning play an important role. For example, the ankle exercise board is an important rehabilitation device after injuries of the leg and the outlined measurement system can be used to monitor the rehabilitation process [16]. A further possibility is to use the extended measurement system of the ski jumping helmet for recording the complete head motion during diseases of the vestibular organ.

A fairly new development is the use of a classical attitude and heading reference system (AHRS) for measuring the angular attitude of limbs or of a part of the vertebral column [9]. In an AHRS, three gyros measure \mathbf{u} , whereas for \mathbf{y} a set of accelerometers and an electronic compass detect the direction of the local gravity and of the local lines of magnetic flux respectively. With this, an AHRS is a complete integrated measurement system for the attitude only and has three Euler angles or a quaternion as motion state \mathbf{x} [12].

Nevertheless, all the examples mentioned here are designed as if all the sensors are attached to a rigid body. It is realistic to assume this (at least as a first approach) for a rowing boat, a javelin, an ankle exercise board, or a helmet. The same is true locally for parts of the human body like the head, the pelvis, or a Humerus. To measure the motion of a larger region or of the whole human body, a direct, simple approach is to assume that the skeleton consists of several rigid bodies moving independently of each other. Delleman, den Dekker, and Tan have presented such a measurement system, which consists of a tight-fitting suit with several AHRS sewed in [3, 9]. However, this method does not incorporate kinematical constraints, which limit the relative body motions considerably. In this regard, the approach of Wu and Ladin [20] was already more advanced, but did not include aiding measurements. Combining the sensor equipment of Delleman et al. [3] as well as of Wu and Ladin [20] and designing \mathbf{f} and \mathbf{h} as described by Wagner [14] would lead to a very sophisticated integrated measurement system. Yet, a realisation requires some manpower and is still lacking.

4 Conclusions

Modern navigation technology enables the design of small, light, and inconspicuous motion measurement systems, which can be tailored to the characteristic kinematics of specific human motions. If a high resolution with time, a good long-term accuracy, and high reliability is required simultaneously, the employment of an integrated system according to Figure 2 is advisable. With this, integrated motion measurement systems offer an interesting possibility for research and education in medicine and sport as they can provide motion data in a surpassing quality.

Referring to Figure 2, the system input \mathbf{u} provides normally the high resolution with time and reliability. Predominantly, it is measured with inertial sensors. The aiding sensors effect the long-term accuracy, and their signals

can easily be checked for measurement disturbances. The adaption to the particular human motion considered is carried out by the design of \mathbf{f} and \mathbf{h} in close relationship with a suitable sensor arrangement. This is a standard but demanding engineering task which requires experience as well as a certain development effort. Technical mature sports systems are therefore still rare. On the other hand, it represents an appealing challenge for engineering in Biomechanics.

Correspondingly, it seems highly desirable to design and to realize such an integrated system for at least one popular sports discipline. If, e. g., a system for rowing exists, the transfer to sailing, canoeing, cycling, ski jumping, alpine skiing, hang gliding, etc. is simple; inline skating systems are alike usable for ice skating and cross country skiing.

A final remark, which is of central importance, concerns the appropriate analysis of the data generated. This is an additional, vital task, which needs sophisticated methods of sports science, neurology, and orthopaedics. The design of such data evaluation procedures has to be addressed for the future, too. With this, a better insight in balance control and motor learning (e. g., for fitness assessment of children for road traffic) as well as in malpositions and skeletal loads is possible. Other applications are athletes' performance analysis, sports competition analysis, or training and rehabilitation documentation.

References

1. Blumenbach, T.: *GPS-Anwendungen in der Sportwissenschaft: Entwicklung eines Messverfahrens für das Skispringen*. Bayerische Akademie der Wissenschaften, München, 2005.
2. Buchner, M.; Männer, R.; Marey, A. & Noehte, S.: Dr. Feelgood – Neue Ansätze im mobilen Monitoring. *Biomedical Journal* **57** (2001), 25–27.
3. Delleman, N. J.; den Dekker, E. & Tan, T. K.: I3VR: intuitive interactive immersive virtual reality-technology. In Koningsveld, E. (ed.): *Proceedings of the 16th World Congress of the International Ergonomics Association (IEA)*, Elsevier, Amsterdam 2006, CD-ROM.
4. Farrell, J. A. & Barth, M.: *The Global Positioning System and inertial navigation*. McGraw-Hill, New York, 1999.
5. Hänyes, B.; Körndle, H. & Lippens, V.: Gerätetest mit Hand und Fuß. *Rudersport* **104** (1986), 226–227.
6. Hofmann-Wellenhof, B.; Legat, K. & Wieser, M.: *Navigation*. Springer-Verlag, Wien, 2003.
7. Jerchow, F.: *From sextant to satellite navigation*. C. Plath, Hamburg, 1987.
8. Lawrence, A.: *Modern inertial technology: navigation, guidance, and control*. Corrected 3rd print. Springer-Verlag, New York, 2001.
9. Luinge, H. J.: *Inertial Sensing of Human Movement*. Dissertation, Twente University Press, Enschede, 2002.
10. Maluf, N.: *An Introduction to microelectromechanical systems engineering*. 2nd ed. Artech House Publishers, Boston, 2004.

11. Nicol, K. & Peikenkamp, K. (eds.): *Apparative Biomechanik – Methodik und Anwendungen*. Feldhaus, Hamburg, 2000.
12. Stieler, B. & Winter, H.: *AGARDograph 160 Vol. 15, Gyroscopic Instruments and their Application to Flight Testing*. AGARD, Neuilly-sur-Seine, 1982.
13. Wagner, J. F.: *Zur Verallgemeinerung integrierter Navigationssysteme auf räumlich verteilte Sensoren und flexible Fahrzeugstrukturen*. VDI-Verlag, Düsseldorf, 2003.
14. Wagner, J. F.: Adapting the principle of integrated navigation systems to measuring the motion of rigid multibody systems. *Multibody System Dynamics* **11** (2004), 87–110.
15. Wagner, J. F.; Bartmus, U. & de Marées, H.: Three-axes gyro system quantifying the specific balance of rowing. *International Journal of Sports Medicine* **14** (1993), 35–38.
16. Wagner, J. F.; Lippens, V.; Nagel, V.; Morlock, M. & Vollmer, M.: An instrument quantifying human balance skills: attitude reference system for an ankle exercise board. *International Journal of Computer Science in Sport* **1** (2003), 96–105.
17. Wagner, M. & Reinking, J.: Messen für künftige Weltmeister: Nutzung von Low-Cost-GPS im Rudersport. *Der Vermessungsingenieur* **3** (2004), 182–186.
18. Warnemünde, R. & Schmucker U.: Entwicklung eines integrierten Messsystems zur Bestimmung von Beschleunigung und Geschwindigkeit beim Speerwerfen. In *BISp-Jahrbuch 2001*. Bundesinstitut für Sportwissenschaft, Bonn, 2001, pp. 161–164.
19. Winkler, S. & Vörsmann, P.: Bird’s-eye view. *GPS World* **10** (2004), 14–22.
20. Wu, G. & Ladin, Z.: The study of kinematic transients in locomotion using the integrated kinematic sensor. *IEEE Transactions on Rehabilitation Engineering* **4** (1996), 193–200.

Author Index

Böl, Markus	1	Nackenhorst, Udo	49
Balzani, Daniel	97	Ott, Ingrid	33
Bluhm, Joachim	59	Reese, Stefanie	1
Brands, Dominik	97	Rheinbach, Oliver	97
Bucher, Anke	21	Ricken, Tim	59
Cimrman, Robert	77	Rohan, Eduard	77
Ehlers, Wolfgang	11	Rues, Stefan	87
Görke, Uwe-Jens	21	Schindler, Hans J.	87
Günther, Hubert	21	Schröder, Jörg	97
Karajan, Nils	11	Schröder, Roland	33
Kienzler, Reinhold	33	Schweizerhof, Karl	87
Klawonn, Axel	97	Steeb, Holger	109
Kreißig, Reiner	21	Wagner, Jörg F.	121
Lenz, Jürgen	87	Wieners, Christian	11
Lukeš, Vladimír	77	Wimmer, Markus A.	21
Lutz, André	49		

List of Participants

Dipl.-Ing. Ayhan Acartürk
acar@mechbau.uni-stuttgart.de
Institut für Mechanik (Bau)
Universität Stuttgart

Dipl.-Ing. Dominik Brands
dominik.brands@uni-due.de
Institut für Mechanik
Universität Duisburg-Essen

Prof. Dr.-Ing. Wolfgang Ehlers
ehlers@mechbau.uni-stuttgart.de
Institut für Mechanik (Bau)
Universität Stuttgart

Dr.-Ing. Uwe-Jens Görke
uwe-jens.goerke@mb.tu-chemnitz.de
Institut für Mechanik und
Thermodynamik
TU Chemnitz

Dipl.-Ing. Grieta Himpel
himpel@rhrk.uni-kl.de
Lehrstuhl für Technische Mechanik
TU Kaiserslautern

Prof. Dr. Axel Klawonn
axel.klawonn@uni-due.de
Fachbereich Mathematik
Universität Duisburg-Essen

**Prof. Dr.-Ing. Manfred
Krafczyk**
kraft@cab.bau.tu-bs.de
Institut für Computeranwendungen
TU Braunschweig

Dr.-Ing. Markus Böhl
m.boel@tu-bs.de
Institut für Festkörpermechanik
TU Braunschweig

Dipl.-Ing. Tobias Ebinger
t.ebinger@mx.uni-saarland.de
Lehrstuhl für Technische Mechanik
Universität des Saarlandes

Dipl.-Ing. Mario Fleischer
fleischer.mario@web.de
Institut für Festkörpermechanik
TU Dresden

Prof. Dr. Christian Hellmich
christian.hellmich@tuwien.ac.at
Institut für Mechanik der
Werkstoffe und Strukturen
TU Wien

Dipl.-Ing. Nils Karajan
karajan@mechbau.uni-
stuttgart.de
Institut für Mechanik (Bau)
Universität Stuttgart

**Prof. Dr.-Ing. Reinhold
Kienzler**
rkienzler@uni-bremen.de
Fachgebiet Technische Mechanik -
Strukturmechanik
Universität Bremen

JP Dr.-Ing. Ellen Kuhl
ekuhl@rhrk.uni-kl.de
Lehrstuhl für Technische Mechanik
TU Kaiserslautern

Vladimir Lukes
lukes@kme.zcu.cz
Department of Mechanics and New
Technologies Research Centre
University of West Bohemia

Dr.-Ing. Bernd Markert
markert@mechbau.uni-
stuttgart.de
Institut für Mechanik (Bau)
Universität Stuttgart

**Prof. Dr.-Ing. Udo
Nackenhorst**
nackenhorst@ibnm.uni-
hannover.de
Institut für Baumechanik und
Numerische Mechanik
Universität Hannover

Prof. Dr.-Ing. Friedrich Pfeiffer
pfeiffer@amm.mw.tum.de
Institute for Applied Mechanics
TU München

Dr. Oliver Rheinbach
oliver.rheinbach@uni-essen.de
Fachbereich Mathematik
Universität Duisburg-Essen

Dr. Eduard Rohan
rohan@kme.zcu.cz
Department of Mechanics and New
Technologies Research Centre
University of West Bohemia

**Prof. Dr. med. Dr. rer. nat.
Fritz Schick**
fritz.schick@med.uni-
tuebingen.de
Sektion für Experimentelle
Radiologie
Universität Tübingen

M. Sc. André Lutz
lutz@ibnm.uni-hannover.de
Institut für Baumechanik und
Numerische Mechanik
Universität Hannover

**Dipl.-Phys. Isabel Rica
Mendez**
isabel@tat.physik.uni-
tuebingen.de
Theoretische Astrophysik
Universität Tübingen

Dipl.-Ing. Ingrid Ott
ingrid@mechanik.uni-bremen.de
Fachgebiet Technische Mechanik -
Strukturmechanik
Universität Bremen

Prof. Dr.-Ing. Stefanie Reese
s.reese@tu-bs.de
Institut für Festkörpermechanik
TU Braunschweig

JP Dr.-Ing. Tim Ricken
tim.ricken@uni-essen.de
Institut für Mechanik
Universität Duisburg-Essen

Dipl.-Ing. Stefan Rues
stefan.rues@ifm.uni-
karlsruhe.de
Forschungsgruppe Biomechanik
Universität Karlsruhe

Prof. Dr.-Ing. Jörg Schröder
j.schroeder@uni-essen.de
Institut für Mechanik
Universität Duisburg-Essen

Prof. Dr.-Ing. Rüdiger Schmidt
schmidt@iam.rwth-aachen.de
Institut für Allgemeine Mechanik
RWTH Aachen

Dipl.-Phys. Syn Schmitt
syn.schmitt@sport.uni-
freiburg.de
Institut für Sport und
Sportwissenschaft - Arbeitsgruppe
Motorik
Universität Freiburg

**Prof. Dr.-Ing. Karl
Schweizerhof**
karl.schweizerhof@ifm.uni-
karlsruhe.de
Institut für Mechanik
Universität Karlsruhe

Dr.-Ing. Holger Steeb
h.steeb@mx.uni-saarland.de
Lehrstuhl für Technische Mechanik
Universität des Saarlandes

Harry van Lenthe, Ph.D.
vanlenthe@biomed.ee.ethz.ch
Institute for Biomedical
Engineering
University and ETH Zurich

Prof. Dr.-Ing. Jörg Wagner
jfw@isd.uni-stuttgart.de
Institut für Statik und Dynamik
der Luft- und
Raumfahrtkonstruktionen
Universität Stuttgart

**Prof. Dr. biol. hum.
Hans-Joachim Wilke**
hans-joachim.wilke@uni-ulm.de
Institut für Unfallchirurgische
Forschung und Biomechanik
Universität Ulm

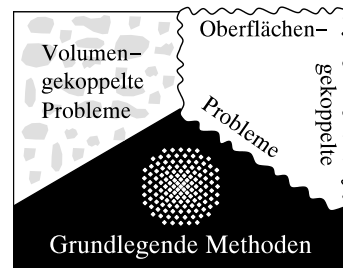
Prof. Dr. Christian Wieners
wieners@math.uni-karlsruhe.de
Institut für Angewandte und
Numerische Mathematik
Universität Karlsruhe

Prof. Philippe Zysset
philippe.zysset@ilsb.tuwien.
ac.at
Institute for Lightweight Design
and Structural Biomechanics
TU Wien

Wednesday 22.11.	Thursday 23.11.	Friday 24.11.
8:00 - 9:00	 Breakfast	 Breakfast
9:00 - 10:30	<p style="text-align: center;"><i>Welcome</i> (W. Ehlers)</p> <p>Section 1 · Chair: Zysset IVD & CARTILAGE</p> <ol style="list-style-type: none"> 1.) <u>Wilke</u>: Biomechanical Characteristics of Different Non-Fusion Technologies 2.) <u>Karajan</u>: Advances in Modelling the Intervertebral Disc 3.) <u>Goerke</u>: Experimental-Numerical Studies of Impaction Loading of Osteochondral Grafts 	<p>Section 5 · Chair: Klawonn GROWTH & REMODELLING</p> <ol style="list-style-type: none"> 1.) <u>Kuhl</u>: Stress vs. Strain-based Remodelling in Arterial Walls 2.) <u>Ricken</u>: Remodelling and Growth of Living Tissue by Using a Multiphase Theory 3.) <u>Markert</u>: An Energy-based Biphasic Growth Model for Neoplasms
10:30 - 11:00	 Coffee Break	 Coffee Break
11:00 - 13:00	<p>Section 2 · Chair: Nackenhorst BONE MECHANICS</p> <ol style="list-style-type: none"> 1.) <u>van Lenthe</u>: High-Throughput Computational Analyses of Bone Mechanics: From Mice to Men 2.) <u>Zysset</u>: Fabric-based Computational Mechanics of Trabecular Bone 3.) <u>Steeb</u>: Acoustic Wave Propagation in Cancellous Bone: From Sound to Ultrasound 4.) <u>Ott</u>: A Damage-Based Model to Describe Aging in Cortical Bone 	<p>Section 6 · Chair: Kienzler MUSCLES & MOTION</p> <ol style="list-style-type: none"> 1.) <u>Böl</u>: Micromechanical Modelling of Skeletal Muscles: From the Single Fibre to the Whole Muscle 2.) <u>Rues</u>: Muscle and Joint Forces in the Masticatory System 3.) <u>Wagner</u>: Integrated Motion Measurement in Biomechanics 4.) <u>Schmitt</u>: Computer Simulations in Biomechanics and Physics <p style="text-align: center;"><i>Closing</i> (W. Ehlers)</p>

13:00 - 14:00		 Lunch	 Lunch
14:30 - 16:00		Section 3 · Chair: Reese <u>COMPUTATIONAL METHODS</u> 1.) <u>Wieners</u> : Parallel Numerical Methods for a Porous Media Model in Biomechanics 2.) <u>Schröder</u> : Mechanical Modelling of Arterial Walls and Parallel Solution Strategies Using FETI-Domain Decomposition Methods 3.) <u>Krafczyk</u> : Kinetic Multi-scale Simulation of Biological Flows	Departure Check out
16:00 - 16:30		 Coffee Break	
16:30 - 18:00	Arrival Check In	Section 4 · Chair: Schröder <u>GENERAL BIOMECHANICS</u> 1.) <u>Schick</u> : Principles of Magnetic Resonance and Some Applications to Tissue Characterization 2.) <u>Hellmich</u> : Effect of Ray Cells on Wood Stiffness and Strength: A Continuum Micromechanics Investigation 3.) <u>Rohan</u> : Homogenization in Soft Biological Tissue Modelling – Two-scale FE Computing	
18:00 - 19:30		 Dinner	
19:30 - ...	 Welcome Dinner	Meeting of the Biomechanics Activity Group	

Sponsors of the 2nd GAMM Seminar on
Continuum Biomechanics



Released Report Series

- II-1 Gernot Eipper: *Theorie und Numerik finiter elastischer Deformationen in fluidgesättigten porösen Festkörpern*, June 1998.
- II-2 Wolfram Volk: *Untersuchung des Lokalisierungsverhaltens mikropolarer poröser Medien mit Hilfe der Cosserat-Theorie*, May 1999.
- II-3 Peter Ellsiepen: *Zeit- und ortsadaptive Verfahren angewandt auf Mehrphasenprobleme poröser Medien*, July 1999.
- II-4 Stefan Diebels: *Mikropolare Zweiphasenmodelle: Formulierung auf der Basis der Theorie Poröser Medien*, March 2000.
- II-5 Dirk Mahnkopf: *Lokalisierung fluidgesättigter poröser Festkörper bei finiten elastoplastischen Deformationen*, March 2000.
- II-6 Heiner Müllerschön: *Spannungs-Verformungsverhalten granularer Materialien am Beispiel von Berliner Sand*, August 2000.
- II-7 Stefan Diebels (Ed.): *Zur Beschreibung komplexen Materialverhaltens: Beiträge anlässlich des 50. Geburtstages von Herrn Prof. Dr.-Ing. Wolfgang Ehlers*, August 2001.
- II-8 Jack Widjajakusuma: *Quantitative Prediction of Effective Material Parameters of Heterogeneous Materials*, June 2002.
- II-9 Alexander Droste: *Beschreibung und Anwendung eines elastisch-plastischen Materialmodells mit Schädigung für hochporöse Metallschäume*, October 2002.
- II-10 Peter Blome: *Ein Mehrphasen-Stoffmodell für Böden mit Übergang auf Interface-Gesetze*, October 2003.
- II-11 Martin Ammann: *Parallel Finite Element Simulations of Localization Phenomena in Porous Media*, April 2005.
- II-12 Bernd Markert: *Porous Media Viscoelasticity with Application to Polymeric Foams*, July 2005.
- II-13 Saeed Reza Ghadiani: *A Multiphasic Continuum Mechanical Model for Design Investigations of an Effusion-Cooled Rocket Thrust Chamber*, September 2005.
- II-14 Wolfgang Ehlers & Bernd Markert (Eds.): *Proceedings of the 1st GAMM Seminar on Continuum Biomechanics*, September 2005.

- II-15 Bernd Scholz: *Application of a Micropolar Model to the Localization Phenomena in Granular Materials*, December 2007.
- II-16 Wolfgang Ehlers & Nils Karajan (Eds.): *Proceedings of the 2nd GAMM Seminar on Continuum Biomechanics*, December 2007.